Electrochemical Methods for Graphene-Based Materials for Biosensors

Abstract

The literature review of this thesis goes through the most common types of graphene-based materials, essential fundamentals of electrochemistry required for biosensing, discusses the possible electrochemical methods and finally gives examples of applications taking advantage of said methods in different types of biosensing. The goal of the experimental work presented here was to characterize a novel graphene-based material called EGNITE and find an electrochemical method for measuring pH using the material as an electrode. The material was found to be pH sensitive but finding a clear and reliable method for pH sensing was challenging. The material was characterized using Raman spectroscopy, scanning electron microscopy, X-ray photoelectron spectroscopy and cyclic voltammetry. The results show very high capacitive properties (41.9 to 52.2 mF/cm^2) for EGNITE in comparison to plain single-layer graphene (21 $\mu F/cm^2$). They also show that an autoclaving treatment was successfully used to reduce EGNITE to increase its conductivity. However, this also increased its defect concentration. Electrochemical methods explored for the pH measurements were cyclic voltammetry, potentio electrochemical impedance spectroscopy (PEIS), chronoamperometry and PEIS-wait. PEIS measurements showed the most promise and equivalent circuit fitting was successfully used to inspect the material's pH sensitivity. However, further work has to be done to find a reliable and reproducible pH measuring method using EGNITE. This is because of the poor reproducibility of the measurements and sample to sample variation.

Tiivistelmä

Tämän opinnäytetyön kirjallisuuskatsaus käy läpi tyypillisimmät grafeeniin pohjautuvat materiaalit, biosensoreihin liittyvät olennaiset perusteet sähkökemiasta, niihin soveltuvat sähkökemian metodit ja lopuksi erilaisia sovelluksia, jotka käyttävät näitä metodeita biosensoreissa. Kokeellisen osion tavoitteena oli karakterisoida EGNITE, joka on uusi grafeeniin pohjautuva materiaali. Tarkoituksena oli löytää sähkökemiallinen metodi, jonka avulla tätä uutta materiaalia voitaisiin käyttää pH-mittauksissa. EGNITE osoittautui pH-herkäksi materiaaliksi, mutta selkeän ja luotettavan metodin löytämisessä oli haasteita. EGNITE:n karakterisointi suoritettiin käyttämällä Raman spektroskopiaa, pyyhkäisy-elektronimikroskopiaa (SEM), röntgenfotonispektroskopiaa (XPS) ja syklistä voltametriaa (CV). Niiden tulokset osoittivat, että EGNITE on hyvin kapasitiivinen materiaali (41,9 – 52,2 mF/cm^2) verrattaessa yksikerroksiseen grafeeniin (21 µF/cm^2). Tämän lisäksi osoitettiin, että käyttämällä autoklaavia, materiaalia saatiin onnistuneesti pelkistettyä parantaen sen johtokykyä, joka myös kasvatti sen rakenteessa esiintyvien defektien konsentraatiota. Sähkökemialliset metodit, joita käytettiin pH-herkkyyden tutkimisessa, olivat CV, jännitekontrolloitu sähkökemiallinen impedanssispektroskopia (PEIS), kronoamperometria (CA) ja kronometrinen jännitekontrolloitu sähkökemiallinen impedanssispektroskopia (PEISW). Saadut tulokset käyttäen PEIS-menetelmää osoittautuivat kaikkein lupaavimmiksi. Niistä mittauksista saatuun dataan sovitettiin onnistuneesti ekvivalenttipiiri pH-herkkyyden tutkimiseksi. Tämän opinnäytetyön tuloksista huolimatta lisää työtä materiaalin parissa tulee tehdä, jotta toimiva ja toisinnettavissa oleva sähkökemiallinen metodi pH:n mittaamiseen löytyy. Syynä tähän on ongelmat toisinnettavuudessa ja näytteiden välisissä eroissa.

Preface

The experimental work for this thesis was conducted during the autumn of 2019 in collaboration with a research group led by Jose Antonio Garrido in the Catalan Institute of Nanoscience and Nanotechnology (ICN2) at the Autonomous University of Barcelona. The literature review part has been written afterwards, under quarantine in Barcelona, during the COVID-19 pandemic of spring 2020. The references have been found for the most part online using Google Scholar, Google, JYU Finna, ProQuest eBook Central and Springer Link. The work instructors have been Mika Pettersson from the University of Jyväskylä and Jose Antonio Garrido from ICN2.

This thesis aims to help other students who are about to embark on electrode characterization measurements and provide good sources of information for further reading. The experimental part goes through the methods used in characterization in a way that can be used to make measurements and data analysis. The literature review on the other hand goes deeper into the theory of general electrochemistry giving more background and deeper understanding to the practical work presented.

I wish to thank my instructors Jose Antonio Garrido for taking me into his research group and giving me the chance to work there and Mika Pettersson for his advice and patience with me and the flexibility and freedom I have had with my thesis. Of course, a thank you goes to the whole Advanced Electronic Materials and Devices research group at ICN2. Also, I wish to thank my friends from the University of Jyväskylä for the amazing years of student life that have led to this moment, for the trip would not have been the same without you all. And I must also acknowledge the Erasmus+ program for giving me the practical and financial support to make it possible to work on my thesis abroad.

Table of contents

Abbreviations

1LG:	Single layer graphene
3D:	Three-dimensional
AC:	Alternating current
BSE:	Backscattered electrons
CA:	Chronoamperometry
CE:	Counter electrode
CSC:	Charge storage capacitance
CV:	Cyclic voltammetry
CVD:	Chemical vapor deposition
DC:	Direct current
DI:	Deionized
DNA:	Deoxyribonucleic acid
DPV:	Differential pulse voltammetry
EEI:	Electrode–electrolyte interface
EGNITE:	Engineered graphene for neural interfaces
EIS:	Electrochemical impedance spectroscopy
EMC:	Esin-Markov coefficient
FRA:	Frequency response analyzer
FWHM:	Full width at half-maximum
GCE:	Glassy carbon electrode
GCS:	Gouy-Chapman-Stern model
GEIS:	Galvano electrochemical impedance spectroscopy
GO:	Graphene oxide
ICN2:	Catalan Institute of Nanoscience and Nanotechnology
IHP:	Inner Helmholtz plane
INE:	Ideally nonpolarizable electrode
IPE:	Ideally polarizable electrode
LSV:	Linear sweep voltammetry
NPV:	Normal pulse voltammetry
OCP:	Open circuit potential
OHP:	Outer Helmholtz plane
OP:	Organophosphorus
PEIS:	Potentio electrochemical impedance spectroscopy

PEISW: PEIS Wait (at one frequency against time)

RE: Reference electrode

rGO: Reduced graphene oxide

RPV: Reverse pulse voltammetry

RSF: Relative sensitivity factor

SCE: Saturated calomel electrode

SE: Secondary electrons

SEM: Scanning electron microscopy

SHE: Standard hydrogen electrode

SNR: Signal to noise ratio

SOX: Sarcosine oxidase

SWV: Square wave voltammetry

UPS: Ultraviolet photoelectron spectroscopy

VBA: Visual Basic for Applications

WE: Working electrode

XPS: X-ray photoelectron spectroscopy

Literature Review Section

1 Introduction

The field of electrochemistry includes a vast variety of different methods. It mainly studies the relationship between the passage of electric current and chemical reactions. This includes both controlling the reaction by controlling the current or potential applied to the system and taking advantage of known chemical reactions to create electric currents. In addition, there is a plethora of different phenomena, technologies and devices that are classified as electrochemistry. These include electrophoresis, corrosion, electrochromic displays, batteries, electroplating, electrodeposition, large scale manufacturing of metals and electroanalytical sensors.[1] In this thesis the focus of electrochemistry is on the phenomena and devices that are used for chemical sensing.

One important factor in any electrochemical system is the materials used in it. To create new and innovative applications for electrochemistry, new types of materials have to be incorporated into the designs. One such family of materials that has in the last decade been very much present in the field of electrochemistry is graphene-based materials. They show promise due to their tunable properties, such as surface chemistry and electric conductivity. This flexibility is of huge importance in applications such as chemical sensing or biosensing.[2]

Biosensing is, likewise, a large branch of research. As an example, biosensing includes wearable sensors for medical or personal monitoring[3], laboratory tests for early stage detection of disorders such as Alzheimer's disease[4] or quality monitoring of products in the food industry[5]. To limit the discussion here to a sensible amount, the focus of this thesis is on the possibilities of biosensing using the two fields mentioned above: electrochemistry and graphene-based materials.

This literature review aims to discuss the essential parts of the theory required to understand and use electrochemical methods. The discussion is begun by first going through graphene, its derivatives and their properties briefly, mainly through examples. This is followed by a discussion of the electrochemical theory, starting from the fundamentals. After the fundamentals, the electrochemical methods are discussed. And finally, relevant biosensing applications found in literature are presented with an emphasis on the electrochemical methods used in those applications.

The literature review presented here is written with a significant part of it based on the so-called Bible of Electrochemistry, *Electrochemical Methods: Fundamentals and Applications* by Bard and Faulkner[1]. Sections 4 and 5 mainly provide a summary of the main topics relevant to the other work presented here with some additions from other newer sources.

2 Graphene

The honeycomb lattice single layer graphene (1LG) has become a familiar research subject in the last two decades ever since the publication of its original isolation[6] with scotch tape. The main interests in the material that was originally thought to be thermodynamically unstable in room temperature are its extraordinary electrical, mechanical and thermal properties. These properties had been of interest in theoretical studies for a long time before any experiments had been conducted with the material.[7]

The lattice structure of graphene is presented in Figure 1a). This consists of unit cells formed of two sp^2 hybridized atoms with both of them having three bonds. The single atom thick layer makes it possible for π and π^* states to not interact and this forms an interesting band structure presented in Figure 1b). In the band structure the π states form the valence band and π^* states the conduction band. These two bands only meet at six different points known as the Dirac points. The band structure, at low energies, due to its symmetry can be simplified into two cones touching at the Dirac point (Figure 1c)). Because the states π and π^* do not interact, but touch at Dirac points, graphene is said to have zero band gap and is often called a zero-gap semimetal.[8]

Regarding the electrochemistry of 1LG, some properties are important to mention.[9] First of all, the potential window that graphene presents is wide[10], 2.5 V. This value is comparable to that of many other carbon-based materials and indicates that graphene is a stable material in electrochemical measurements.[9] Based on electrochemical impedance measurements the charge-transfer resistance of graphene is lower than that of glassy carbon electrodes (GCE) or graphite electrodes.[10] Graphene-based electrodes also seem to exhibit mainly diffusion controlled redox processes as indicated by the linear behavior of peak current when plotted against the square root of the cyclic voltammetry (CV) scan rate.[11] In addition, the redox peaks forming in CV have a small peak-to-peak separation, which indicates that graphene has fast
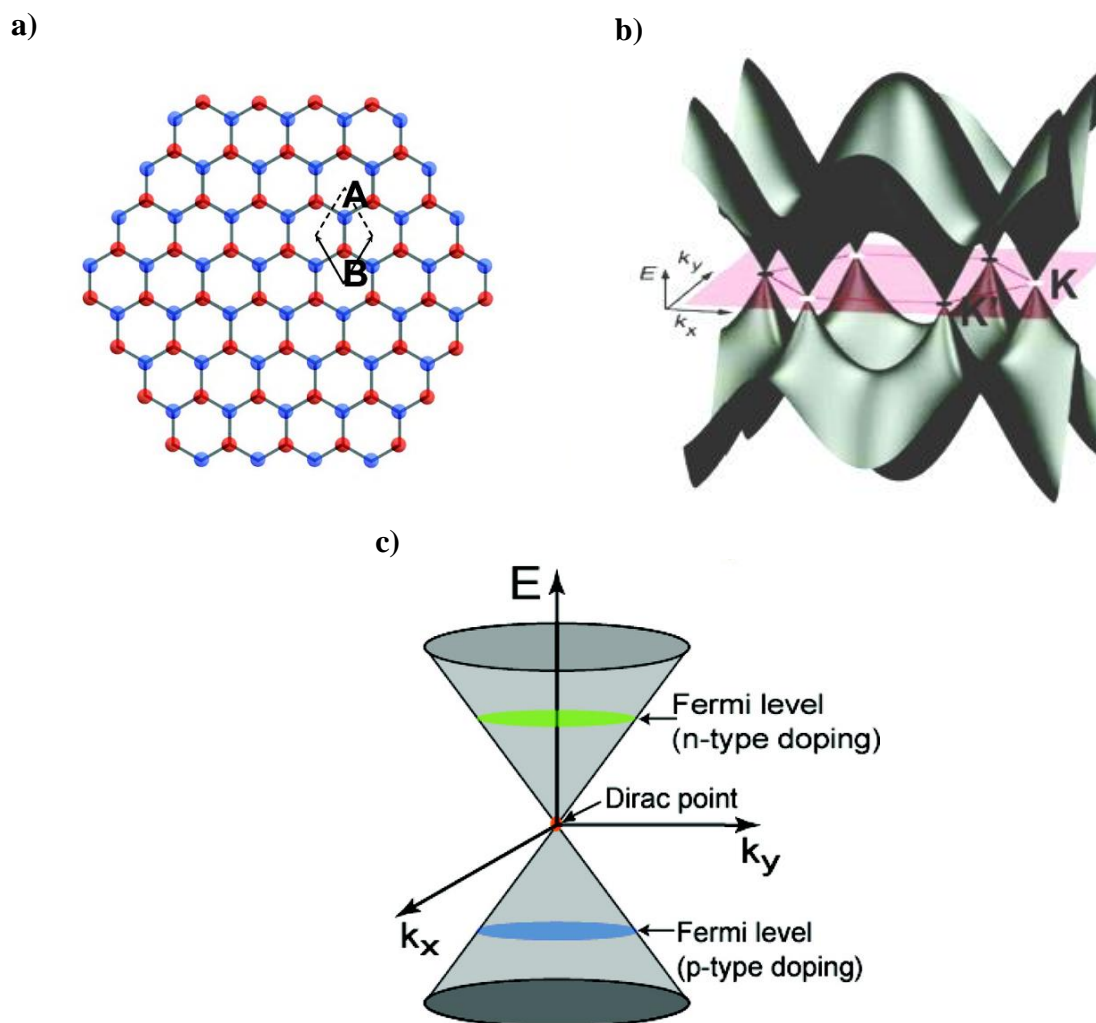
Figure 1: a) Graphene's hexagonal lattice with the unit cell formed of A and B atoms, **b)** a 3D rendering of the band structure of graphene and **c)** the simplified low energy band structure with the Dirac point and Fermi levels with different types of doping presented. Adapted with permission from reference[8]. Copyright (2010) American Chemical Society.

electron transfer properties.[9,12] And in comparison to GCEs the electronic structure and surface physicochemistry of graphene seem to be beneficial for electron transfer based on experiments made with different redox couples with sensitivities to varying impurities of the electrode surface.[9,13] In summary, graphene is a very interesting and suitable material for electrochemical measurements and experiments. The methods mentioned here are explained in the following sections of this thesis.

3 Graphene-Based Materials

Nowadays, in addition to the exploration of the synthesis, properties and applications of 1LG, a vast area of research has been founded in graphene-based materials. For example, this includes chemical functionalization of graphene[2] or creating 3D derivatives[14] of it such as foams, fibers, hydrogels etc. These materials can then be used for biosensors[9], supercapacitors[15] or other applications. The main reason for the interest in these derivative materials is that they are easier to fabricate with a high throughput than the high quality 1LG. Therefore, it is possible to use the similar properties to graphene of the derivatives even though that high throughput fabrication is still lagging behind the batch-to-batch fabrication[16] of, for example, 1LG fabricated by chemical vapor deposition (CVD). It is impossible to go through all of the existing derivatives as there are too many of them, but here some of the most common graphene-based materials are discussed and some examples of their applications are given. Although some overlap is present within the different materials' definitions, the essential differences between the materials give enough reason to differentiate between them.

3.1 Graphene Oxide

One of the most common variations of graphene derivatives is graphene oxide (GO). This material is typically fabricated by exfoliating and oxidizing graphite with strong acids or oxidants. GO can then be reduced by thermal, chemical or electrochemical methods to create electrodes modified with a graphene-based material as a "top down" method. GO has different chemical, electrochemical and electrical properties when compared to 1LG mainly due to the functional oxygen-containing groups attached to its surface. The combination of graphene's crystal structure and the functional groups make GO easily dispersible in water, biocompatible and also exhibits high affinity to certain biomolecules.[17] The functional groups can be for example hydroxyl (–OH), carbonyl (=O), epoxide (>O) or carboxylic acid (–COOH) groups. Figure 2 illustrates a possible structure of GO with different functional groups present. However, the amount and nature of oxygen groups depends greatly on the GO fabrication method. The four most common methods are Tour, Hummers, Hofmann and Staudenmaier methods in the order from the most oxidizing to the least oxidizing method. For the Hofmann and Staudenmaier methods the oxygen groups are usually reduced irreversibly with only one potential sweep when for the others reversibility can be detected.[18]
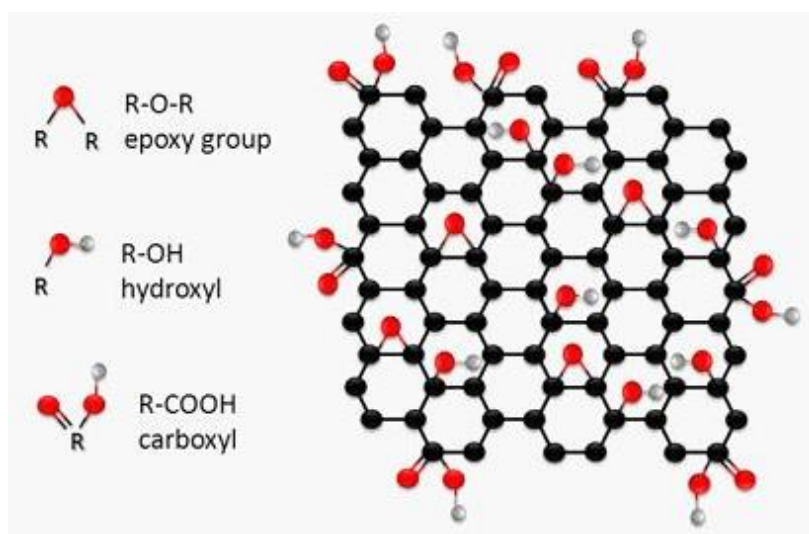
Figure 2: An illustration of the different functional groups of GO. © 2013 Nan-Fu Chiu, Teng-Yi Huang and Hsin-Chih Lai. Adapted from reference[84]; originally published under CC BY 3.0 license. Available from: 10.5772/56221

Because of the structural defects (e.g. sp^3 hybridized carbons) caused by the covalently bound functional groups of GO, the material is not as conductive as 1LG. This means that direct electrochemical applications of GO can be limited.[19] However, it is possible to fabricate devices utilizing GO modified electrodes for different sensing purposes. Commonly they are fabricated by drop-casting. In it a drop of a suspension of GO flakes is placed on the electrode and the solution is removed. Another common method that has also been used to conduct some studies has been spin-coated GO electrodes.[18] GO based devices have been used in numerous applications: together with fluorophores, microfluidics, aptamers or enzymes to detect DNA; RNA, glucose or even cancer; in drug delivery to carry small drug molecules, antibodies, proteins or DNA by different functionalizations.[17]

The electrochemical applications of GO take advantage of the various interactions between the surface functional groups and other molecules.[19] For example, Zuo *et al.*[20] showed that modifying a glassy carbon electrode with GO enables the usage of cyclic voltammetry to see oxidation and reduction peaks of heme proteins. Normally GCEs cannot be used in this manner, but according to Zuo *et al.*[20], mixing GO dispersion with a solution of a protein and then absorbing this mixture to the electrode surface improves the electron transfer between the electrode and the protein. They also claim that this method does not distort the proteins' structures.

3.2 Reduced Graphene Oxide

To improve the conductivity, reduce the number of defects and therefore enable certain new applications, GO is often modified into another graphene-based derivative called reduced graphene oxide (rGO). The required reduction can be conducted with several different methods. Although, having similar water dispersions of rGO as GO typically ends in agglomeration of the flakes. Therefore other solvents or other methods have to be utilized.[21] Park et al.[22] claim in their 2009 paper that they were the first ones to report a colloidal suspension of rGO without stabilizers. They made it by chemically reducing a GO dispersion and using organic solvents. From this suspension they were able to create a "paperlike" material simply by filtration. An alternative electrochemical reduction method using cyclic voltammetry to create a rGO film directly onto an electrode has been presented by Chen et al.[23]. They used cyclic voltammetry in a three-electrode setup to reduce the exfoliated GO flakes onto the surface of a GCE. This deposited film facilitates the detection of redox reactions so that greater currents are seen allowing simultaneous detection of two different organic molecules.

With both GO and rGO the selected fabrication method affects the properties of the product. However, none of the existing methods can completely reform the sp^2 hybridized structure of graphene nor remove all of the oxygen from the material. This is why a distinction between graphene and rGO must be made. But even though all defects cannot be removed, rGO materials have shown high conductivity[24], low sheet resistance[24], low O/C ratios[25] (<6.25 %) and good mobility[24]. The fabricated rGO is often very rough on its surface or not uniform, as it is fabricated from small GO flakes. This type of material can still be used for several applications.[19,25]

An application using an optically transparent and free-standing rGO film has been reported by Yang et al.[24]. They used several rounds of drop-casting of a GO dispersion in alcohol and then drying it overnight to create a 1.15 nm thick GO layer. They say that this thickness indicates that the film only has 1 to 2 layers. After deposition of several of these layers the film was then reduced by annealing to create the final rGO film. The final rGO thin film had the thickness of 542 nm and a smaller average roughness than that of rGO thin films produced by other methods. Yang et al.[24] continued by showing as proof-of-concept that this film could be utilized in a photodetector with reliable and reproducible photoresponse. Another recent application of rGO has been presented by Yu et al.[24] who functionalized a GCE so that they were able to detect trace amounts of Pb^{2+} ions. They used cyclic voltammetry to electrochemically reduce GO from

a dispersion onto the surface of the electrode. A DNA aptamer was then attached onto the rGO layer by π–π interactions. The signal was formed by the interaction between the aptamer and the Pb^{2+} ions in the solution. The sensor was characterized by cyclic voltammetry and electrochemical impedance spectroscopy. The characterization showed that the rGO functionalization enhanced the electron transfer rates of the electrode and that the functionalization with the aptamer had been successful.

3.3 Three-Dimensional Derivatives

Because 1LG graphene has problems of agglomeration in its synthesis, ways to counter this negative phenomenon and for example increase the surface area of graphene-based electrodes have been developed by using 3D derivatives. Several different types of 3D derivatives have been developed with different names: hydrogels, aerogels, foams, networks, monoliths, beads and sponges. Their fabrication methods can be divided into direct fabrication and solution-based fabrication with both of them having template-assisted and template-free possibilities. An overview of the classification of these methods used by Hiew *et al.*[26] is presented in Figure 3. A few of these methods will be described now, but for a more in-depth explanation, the reader is guided to read the original review article.[14,26]

Synthesis of graphene foam by template-assisted CVD is similar to the CVD synthesis of 1LG. Instead of using a copper sheet, a previously made 3D metal framework is used as the growth surface in this direct synthesis. Copper can be used, but as the growth of graphene on copper is
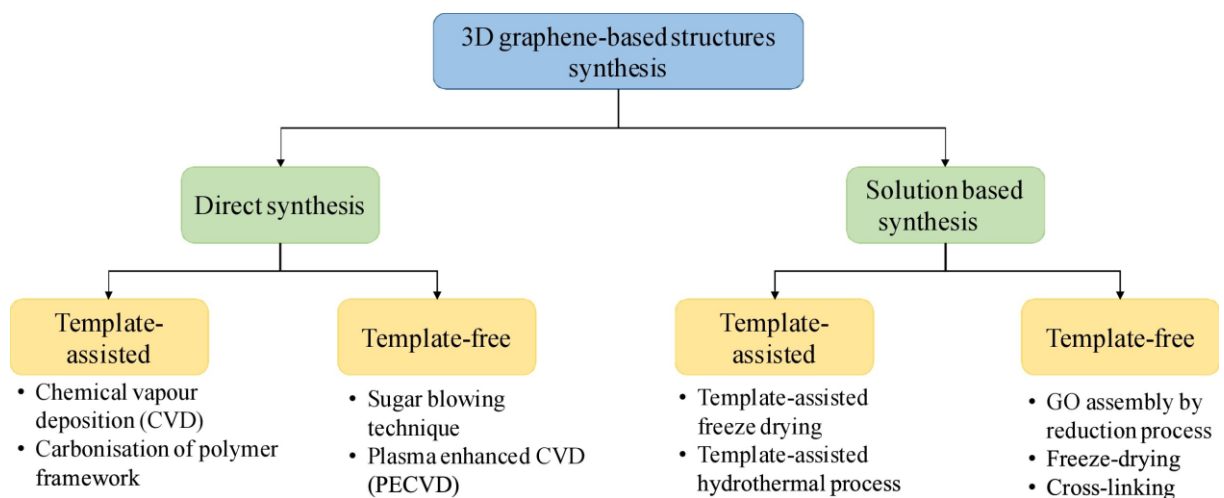

Figure 3: An overview of the classification of the synthesis methods of 3D graphene-based materials.[26]

governed by surface growth, only one layer of graphene will be formed. This has been shown to lead to a failure of the material when it is being handled. Therefore, a nickel-based framework is favored due to dissolution-precipitation of carbon on nickel allowing more layers to be formed strengthening the structure. Altering the framework structure, material and other synthesis parameters, the structure and properties of the 3D graphene-based derivative can be controlled.[26]

The sugar-blowing technique described by Wang *et al.*[27] is a template free direct synthesis method inspired by the food art called 'blown sugar'. In this method a 3D self-supported graphene bubble network consisting of mono- or few-layer graphitic flakes named strutted graphene is fabricated. The materials used for the synthesis are glucose and NH_4Cl, which are heated in a controlled manner. During the heating process the formed syrup walls are thinned by the release of gases and this leaves behind only the carbon nanostructure. By controlling the heating rate it was possible to control the size of the pores and the thickness of the walls.

An example of a solution-based template-free fabrication method is freeze drying. Basically, the method consists of having a water-based solution with graphene-based flakes in it. The solution is frozen, and this forms the lattice structure. When subjected to a vacuum, the frozen water is sublimated, and the graphene-based aerogel is left behind. This has been demonstrated by Zhang *et al.*[28] who reduced a GO solution with L-ascorbic acid and then heated the mixture without stirring. The used acid was chosen so that no gas would be released during the heating as this would break the structure of the forming hydrogel. After the formation of the hydrogel, it was purified by distilled water and freeze dried. Even though they do not describe the freezing or drying conditions, the method is referred to as being simple and treated as common in articles[29] where applications for the material have been studied. In contrast, the template-assisted freeze-drying method uses rapid freezing of other polymers to create the porous scaffolding that then has graphene flakes attached to it. However, this method has its problems with irregularities in the structure and often needs chemical additives to counter this phenomenon.[26]

The 3D graphene-based structures seem to always have a strong and durable self-standing structure, good electric conductivity, high surface area and therefore good capacitive properties. This explains why mainly all of the examples discussed here have been used as materials for supercapacitors, electrodes for energy sources or in some other device related to power storage.

A review article by Venkateshalu and Grace[14] gives a good overview of the topic. However, as seen from the review by Hiew *et al.*[26], this type of materials can also be used in other applications. The graphene-based 3D structures have also been shown[30] to have promise in the development of the next generation of neural interfaces.[14,26]

3.4 Composites

One class of graphene-based derivatives with many possibilities especially related to industry is composite materials. This is due to their typically easily scalable and traditional synthesis methods. They consist of a mixture of some form of graphene and typically a metal, polymer or a more complex hybrid mixture. In order to produce graphene-based composites, it is critical to have high quality and high throughput ways of synthesizing graphene. This will enable the fabrication of high-quality composites that need a homogeneous dispersion of graphene-based particles within the material. Because this type of synthesis for pure graphene flakes is still not at a sufficient level, GO and rGO are utilized a lot in graphene-based composites. There are several possible methods to fabricate composite materials, that include molecular-level dispersion of graphene derivative within a polymer host, sandwich construction, solution intercalation (i.e. solution mixing) and melt-blending.[31]

Solution mixing has been shown to give the best dispersion of graphene flakes in a composite material, but it has the limitation of using only polymer matrixes and needs usually toxic solvents. Because of this, companies are not very interested nor able to do large scale production with this method. Therefore, melt-blending with its high dispersion is preferred.[31] Melt-blending has been used by Song *et al.*[32] who have fabricated a mixture of polypropylene and rGO flakes. They first created a dispersion of rGO flakes and added polypropylene latex so that the individual flakes were coated with the material. This prevented the flakes from agglomerating. Then the coated flakes were mixed into polypropylene in a temperature of 180 °C, which is above the melting point of polypropylene. The mixture was then pressed into a 1 mm thick film with a pressure of 10 MPa while maintaining the high temperature. This allowed the flakes to be evenly dispersed into the composite and increased the strength of the material by 75%.

A two-layer sandwich construction process has been demonstrated by Quan *et al.*[33] in response to a complicated electrode fabrication method that has been difficult to scale up. Their method is a simple filtration process in which a rGO dispersion is first filtrated via suction. Right when

the solvent was about to get used up, another solution containing rGO functionalized with Ni–Mn layered double hydroxides was added. The end result gave a free-standing rGO paper electrode with pseudocapacitive properties and good cycle stability. The suggested applications were energy storage in flexible and wearable devices.

It would seem like that even though these composites are usually called graphene-based indicating that graphene would be the main component, it is more common that the weight percentage of graphene in the material is very low and it is only added to some another matrix. However, as demonstrated by the sandwich structured electrode of Quan *et al.*[33] some applications using actual graphene layers as a part of a composite film are also used. Other examples are non-uniform graphene layers as a part of a polymer film with applications in load-bearing membranes and photovoltaic devices.[34] One important aspect to consider in the graphene-based materials research that has been paid more attention to in recent years is the safety and toxicity of the materials. Especially since many of these materials show promising properties in biomedicine.[31]

4 Basics of Electrochemistry

The following section provides a summary of the theory of electrochemistry from the book by Bard and Faulkner[1]. The reader is recommended to read the original publication for a more in-detail description of electrochemical methods. For a more practical approach to the measurements with these methods, see the section 10 of the experimental part of this thesis.

Electrochemistry is a vast field of chemistry with several topics ranging from devices and technologies to different phenomena. However, for this thesis it is sufficient to focus mainly on applying electrochemical methods in studying electrochemical systems. In these systems the transportation of charge over an interface between two conductive media is of interest. Such as, the charge transfer between a solution (electrolyte) and a conductor (electrode). The charge is transferred by the movement of ions in the electrolyte and by the movement of electrons in the electrode. For this to be possible, the electrolyte solution has to be conductive enough (i.e., has a low enough resistance). Frequently used electrolytes are water-based solutions containing ions such as H^+, Na^+ and Cl^-. However, also other solvents containing ions can be used instead of water. Others, less typical electrolytes can be ion conductive polymers[35] or even solid

electrolytes[36]. For the electrode, a solid conducting metal, liquid metal, carbon or a semiconductor can be used.[1]

To transfer the charge from the electrode to the electrolyte, two types of processes can happen: faradaic or non-faradaic. Faradaic processes get their name from the fact that they follow Faraday's law[37]

$$n_i = \frac{v_i}{v_e F} I_F \Delta t = \frac{v_i}{v_e F} j_F A \Delta t \tag{1}$$

where n_i is the amount (in moles) of the species i used in the reaction, v the stoichiometric coefficient for the species i or the electrons e exchanged in the reaction, F is the Faraday constant $(9.6485 \cdot 10^4 \text{ C/mol})^{[38]}$, I_F the current passed in amperes, j_F the current density in A/m^2, A the surface area of the electrode in m^2 and Δt the duration in seconds during which the current passes. This means that the current flow is proportional to the amount of oxidized or reduced (i.e. reacted) molecules. The electrodes, where reactions happen, are known as charge transfer electrodes. On the other hand, non-faradaic processes happen when the electrode cannot donate electrons to the solution. In this situation, such reactions are kinetically or thermodynamically unfavorable. However, adsorption or desorption can still happen at the interface. In addition, the interface between the electrode and electrolyte can change with an alteration in the potential applied or in the composition of the solution. This type of effects have the common name of non-faradaic processes.[1]

The ideal non-faradaic electrode, known as an ideally polarizable electrode (IPE), cannot exchange electrons from the electrode to the solution or vice versa despite a potential applied to the system. Naturally, it is not possible for real electrodes to work in such manner, but there are systems that can approach an IPE's behavior in certain potential ranges. Because no current can cross the IPE–electrolyte interface, it can be considered as a capacitor. A traditional capacitor, an electric circuit element, has two parallel metal plates facing each other while being separated by a dielectric material (i.e. a polarizable insulator[39]). The capacitance C of a dielectric-filled capacitor is defined by

$$C = \varepsilon \cdot \varepsilon_0 \frac{A}{d}, \tag{2}$$

where ε is the dielectric constant of the material, ε_0 is the permittivity of vacuum, A is the area of the charging plate of the capacitor and d is the distance between the plates of the capacitor.[39] A capacitor's behavior follows the equation

$$C = \frac{q}{E},$$ (3)

where q is the charge passed and E is the potential applied over the capacitor. This behaves so that when a voltage is applied, a current will flow until the equation is fulfilled. However, as seen in the Equation (2) above, the capacitance of a capacitor does not depend on the potential applied, but only on the physical properties of the capacitor. An electrode–electrolyte interface (EEI) has been proven experimentally to behave similarly to a capacitor: When a potential is applied over an EEI, there is a charge q_M in the metal electrode and a charge q_S in the solution. The sign of these charges depends on the potential applied, but they are always the inverse of one another, $q_M = -q_S$. Often these charges are presented as charge densities rather than solely as the charge itself. This charge density is defined as $\sigma_M = q_M/A$ ($\mu C/cm^2$). When q_M is formed on an electrode, it can be considered as an accumulation or dissipation of electrons on a thin surface layer of the electrode. To counter this charge, the q_S forms something called the electrical double layer. In actuality, the structure of this double layer only vaguely seems like two electrically charged layers. (Figure 4a)) We also have to remember that in a real experimental setup, there would be two metal electrodes with their own EEIs facing each other. But to simplify the situation, we can focus only on one of the interfaces.[1]

The electrode's side of the double layer is quite simple if a metal electrode is used. Because a metal is considered a good conductor, it does not have any electric field within it. Therefore, all the charge accumulated at the electrode is on its surface. On the other hand, the solution's side of the double layer is nowadays thought to consist of several different planes following the Gouy-Chapman-Stern model. Starting from the electrode's side, first is the inner Helmholtz plane (IHP). In this region, there are solvent molecules and some ions or molecules that are called specifically adsorbed. Next layer is the outer Helmholtz plane (OHP), where the charged particles are surrounded by the solvent. These particles only interact with the electrode by long-range electrostatic forces. This type of interaction is not dependent of the chemical characteristics of the particle and therefore, these particles are called nonspecifically adsorbed. The last layer is called the diffuse layer that extends all the way to the bulk of the solution. In
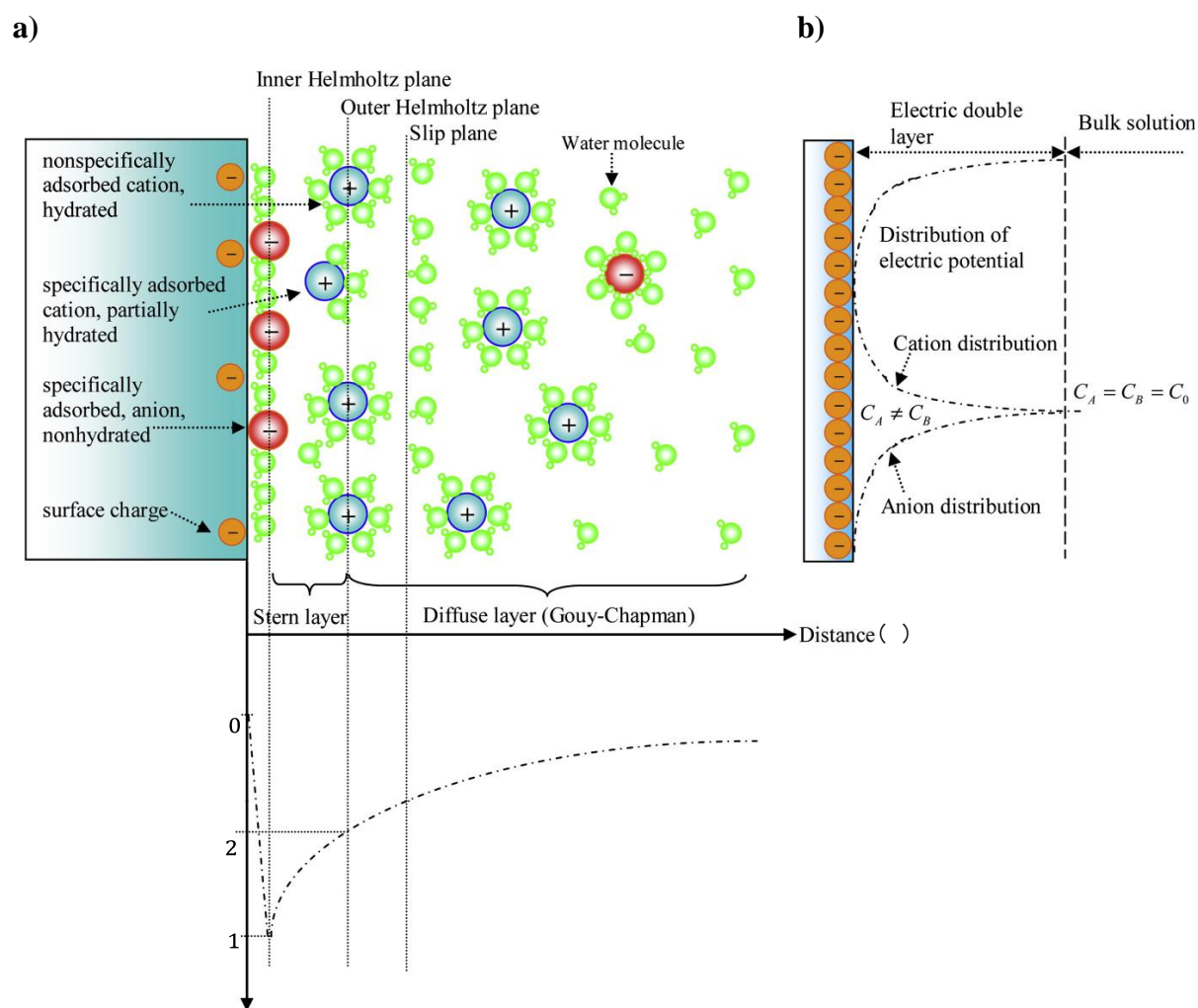
Figure 4: a) The structure of the electric double layer forming at an electrode's surface according to the Gouy-Chapman-Stern model and **b)** some properties of the electric double layer. As it can be seen, the double layer is indeed the surface of the electrode and the electrolyte creating an interface.[85]

this region, the thermal energy in the solution is enough to cause the nonspecifically adsorbed ions to distribute between the OHP and the bulk of the material.[1]

The name of the double layer comes from the hypothesis of Helmholtz, who assumed that the charge accumulated at the surface of a metal electrode would be countered by another layer at the surface of the electrolyte. This would give a constant capacitance in the whole electrolyte solution, when traveling further away from the EEI so that the potential experienced would not change. This would be the case in the dielectric filled capacitor as described above. However,

the potential decreases when the distance from the electrode surface increases. This decrease has been described by Gouy and Chapman.[1]

The Gouy-Chapman model describes how the charge is distributed within the electrolyte. Because the electrolyte has a limited amount of charge carriers, the charge is not all restricted at the surface. Instead, a significant volume of the solution is required to counter the charge accumulated at the metal electrode's surface. The required volume especially increases when the concentration of the electrolyte is low. Therefore, Gouy and Chapman used a diffusion layer to describe the charge distribution within the EEI with

$$\frac{\tanh\left(\frac{ze\phi}{4kT}\right)}{\tanh\left(\frac{ze\phi_0}{4kT}\right)} = \exp(-\kappa x),\tag{4}$$

where

$$\kappa = \left(\frac{2C^*z^2e^2}{\varepsilon\varepsilon_0 kT}\right)^{1/2}.\tag{5}$$

Here z is the charge of an ion of the electrolyte, e the elementary charge of an electron $(-1.6 \cdot 10^{-19}$ C$)^{[37]}$, ϕ the electrostatic potential at the distance x from the electrode surface in mV, ϕ_0 the potential at the solution's side when $x = 0$, k the Boltzmann constant $(1.38 \cdot 10^{-23}$ J/K$)$, T the absolute temperature in Kelvins, κ a double layer thickness parameter in cm^{-1} that can be regarded as a characteristic thickness for the diffuse layer, C^* the amount of ions in the bulk solution per cubic centimeter (cm^{-3}), ε the dielectric constant of the electrolyte and ε_0 the permittivity of free space $(8.855 \cdot 10^{-12}$ C^2 J^{-1} m$^{-1})^{[37]}$. For dilute aqueous solutions, when the $\phi_0 \leq 50/z$ mV and $\varepsilon = 78.49$ at 25 °C these two equations can be approximated to be

$$\phi = \phi_0 \exp(-\kappa x)\tag{6}$$

and

$$\kappa = (3.29 \cdot 10^7)zC^{*1/2},\tag{7}$$

where C^* is the concentration of the $z:z$ electrolyte in moles per liter. The shape of the distribution of electric potential described by these equations can be seen in Figure 4b) and the derivations for these equations are presented in the book by Bard and Faulkner.[1]

The Gouy-Chapman model fails when the polarization of the electrode or the concentration of the electrolyte is high, because it assumes that all ions are infinitely small and therefore, they can approach the electrode surface unlimitedly. This causes at small distances the potential ϕ to increase unlimitedly even though that real systems do not exhibit this behavior. This means that a correction introduced by Stern has to be used. The correction takes into account the fact that the ions of the electrolyte cannot approach the electrode surface closer than the ionic radius. In addition, if the ions are surrounded by the solvent (e.g. hydrated in aqueous solutions) and/or the electrode is covered by a layer of the solvent, the thickness of this layer also has to be taken into account. Therefore, a plane forms at a defined distance x_2, where the centers of the ions are located. This plane is the OHP. Because the Equation (4) still works within the diffuse layer (i.e. when $x \geq x_2$) only a small modification needs to be made:

$$\frac{\tanh\left(\frac{ze\phi}{4kT}\right)}{\tanh\left(\frac{ze\phi_2}{4kT}\right)} = \exp\left(-\kappa(x - x_2)\right), \tag{8}$$

where ϕ_2 is the potential at x_2 and κ is the same as in Equation (5). From the electrode ($x = 0$) to x_2 a linear drop in the potential is experienced. In summary, the differential capacitance C_d of the GCS is

$$\frac{1}{C_d} = \frac{1}{C_H} + \frac{1}{C_D} = \frac{x_2}{\varepsilon\varepsilon_0} + \frac{1}{\left(\frac{2\varepsilon\varepsilon_0 z^2 e^2 C^*}{kT}\right)^{1/2} \cosh\left(\frac{ze\phi_2}{2kT}\right)}, \tag{9}$$

where C_H is the capacitance at OHP and C_D the capacitance at the diffusion plane. As it can be seen, the C_H is not dependent on the potential applied, which is somewhat analogous to the dielectric-filled capacitor although the C_d as a whole is dependent on the potential.[1]

Although the Gouy-Chapman-Stern model (GCS) does succeed in many cases, it still only takes into account the long-distance electric interactions between the charged surface and the

particles in the electrolyte. This type of interaction is called nonspecific adsorption as it does not depend on the chemical properties of the ion. However, it is common that the chemical reactions happening at the electrode surface and the specific adsorption of ions due to these reactions has to be taken into account. It is called specific adsorption because the chemical nature of the adsorbed particle affects the adsorption at the very small distances that this happens. These ions are thought to have their centers at a distance x_1 from the electrode surface, between 0 and x_2. This is called the inner Helmholtz plane (IHP). As one might think, the specific adsorption does affect the charge distribution at the double layer. When the electrolyte has anions and cations in it, which can both adsorb specifically to the electrode surface, the Stern-Grahame model describes the surface charge density σ for an ion i at the IHP as

$$\sigma_i = \frac{z_i e N x^S (b_+ - b_-)}{1 + (b_+ - b_-) x^S}, \tag{10}$$

where z is the charge of the ion, e the elementary charge of an electron, N the total amount of locations on the electrode where ions can be adsorbed to, x^S the molar fraction of the ion in the bulk solution and

$$b = \exp\left(-\frac{\Delta G_{ads}^0}{kT}\right) \tag{11}$$

where

$$\Delta G_{ads}^0 = -kT \ln(K), \tag{12}$$

which is the standard free energy of adsorption per ion with K being the equilibrium constant between the ratios of adsorption and desorption processes. When only one species is allowed to adsorb to the surface, Equation (10) simplifies to

$$\sigma_i = z_i e N x^S \exp(-\frac{z_i e \phi_i + \theta_i}{kT}). \tag{13}$$

Here $z_i e \phi_i$ is an electric contribution and θ_i is a chemical contribution of the adsorption energy as discussed by Stern[40]. To help understand what this behavior of the charge density of a specifically adsorbing ion means in practice, Figure 5 shows a situation where only negatively

charged anions are adsorbing specifically to an electrode surface. When the electrode is charged positively, a negative charge forms on its surface causing a drop in the potential. This charge then has to be compensated by a distribution of counterions in the solution. If the concentration of the specifically charged species is high enough, it is even possible to reverse the sign of the potential as happens with the most positive potential of Figure 5.[41]

In opposition to non-faradaic systems, faradaic systems do have a current flowing through. Since the electrolyte does not have free electrons to allow the passage of current, a reaction has to happen at the EEI. For example, this reaction can be a typical redox half-reaction

$$\text{Fe}^{+3} + e^- \rightarrow \text{Fe}^{+2} \tag{14}$$

resulting in the change of composition of the solution, formation of gases or solid metals or adsorption of species from the solution onto the electrode.[37] To generalize the discussion of the electrode reaction, the reaction from Equation (14) is often written as
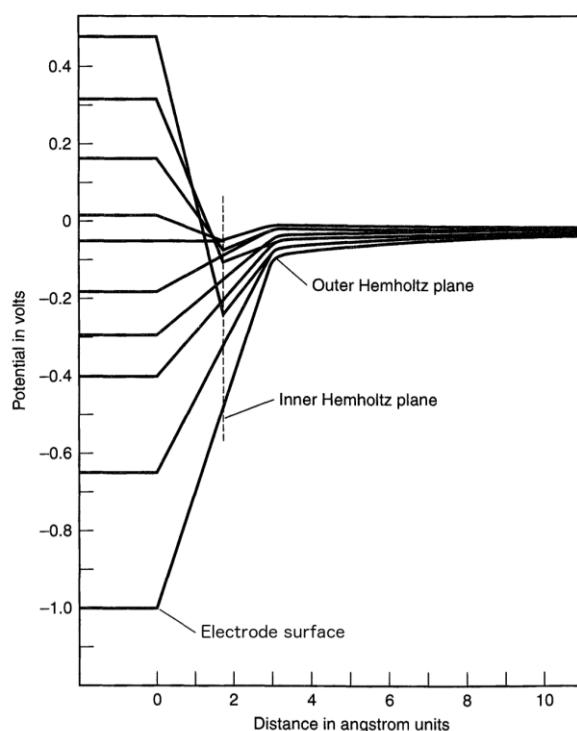

Figure 5: A calculated representation of the effect of specific absorption happening at the EEI double layer. The 1:1 salt has a negatively charged anion that specifically absorbs to the metal electrode's surface at positive applied potentials.[1]

$$O + ne^- \rightleftarrows R \tag{15}$$

To inspect the potentials of electrochemical systems, the reactions have to be reversible. This is due to thermodynamics only being exact at equilibrium.[1]

The two types of faradic systems are galvanic and electrolytic cells. These are commonly known and have several commercial applications. In a galvanic cell, reactions start to happen spontaneously when the two electrodes of the cell are connected via a lead. Common single-use batteries or rechargeable batteries are typical examples of this. For galvanic systems, for the reactions to happen an external potential has to be applied to the system. This is used, for example, in electroplating or even a typical lead car battery can be considered to be a galvanic system when it is being recharged.[1]

When the current is flowing through a faradaic system, the current is usually limited by some property of the system. One of the most common limiting factors is mass-transfer, which is the movement of species in the electrolyte. The mass-transfer can happen either by migration, diffusion or convection. Migration is movement due to an electric field affecting a charged particle, diffusion is due to a chemical potential such as a concentration gradient and convection is due to mechanical perturbation such as stirring the solution. In a mass-transfer-controlled system the kinetics of all the reactions happening have to be fast in comparison to the rate of mass-transfer. This means that if the reactions happening are fast and reversible, the reaction rate v_{rxn} follows an equation similar that of the Faraday law from Equation (1)

$$v_{rxn} = v_{mt} = \frac{I}{nFA}, \tag{16}$$

where v_{mt} is the rate of mass-transfer. Systems like this are called reversible or Nernstian, but these terms are not interchangeable. This is because systems that are Nernstian systems, which are reversible only in a very small potential range around the equilibrium, do exist.[37] In addition, mass-transfer-controlled and Nernstian systems are also different things as there are quasi-reversible systems which are Nernstian, but which are not mass-transfer-controlled.[37] A Nernstian system is defined by the fact that the half-reaction happening at the EEI follows an equation similar to the Nernst law

$$E = E^{0\prime} + \frac{RT}{nF} \ln\left(\frac{C_{Ox}}{C_{Re}}\right). \tag{17}$$

Here E is the electrode potential, $E^{0\prime}$ the formal potential, which is a variation of the standard reaction potential incorporating factors such as activities of the species at hand and some properties of the solution, R is the ideal gas constant (8.314 J K^{-1} mol^{-1})[37], T the temperature in Kelvins, n the stoichiometric number of electrons involved in the electrode reaction and C the concentration of oxidized (O) and reduced (R) species of the redox reaction happening at the EEI.[1]

An important property of a system being limited by for example mass-transfer is the so-called steady-state. The simplest way to describe what is steady-state is that no change is seen in the behavior of the system over time. This means that the change over time is constant and for example the current measured is constant. However, the system does not have to be at equilibrium as equilibrium is only a special case of a steady-state when the overall current is zero. Steady-state systems have characteristic $I - E$ curves that stay stable during electrochemical measurements. The shape in the situation when the initial solution does not include any reacted species is presented in Figure 6. With some initial concentration C_R the current at lower potentials usually has the opposite sign compared to the higher potentials.[1,37]

Usually when measuring electrochemical systems, the interest is only what happens at one electrode. Therefore, the reactions presented are simplified so that only the half-reaction happening at the electrode of interest is shown. This electrode of interest is called the working electrode (WE). To complete the cell, another electrode is needed to couple with the WE. The
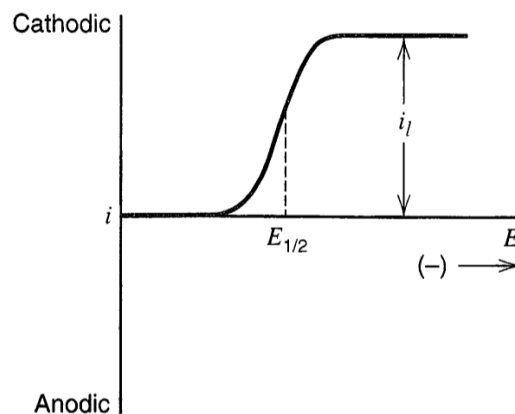

Figure 6: The wavelike *I–E* behavior of a Nernstian steady-state system.[1]

other electrode needs to be approaching an ideally nonpolarizable electrode's (INE) behavior so that its potential does not change and that its potential is known. This electrode is called the reference electrode (RE). For the RE, several standardized electrodes are available that approach ideal behavior, but all in all are not ideal. The common ones are the standard hydrogen electrode (SHE), saturated calomel electrode (SCE) and the silver-silver chloride electrode (Ag/AgCl). Because the measured potential between the WE and the RE depends on the electrode used, the potential is usually noted as against the RE used (e.g. "vs. Ag/AgCl"). The formed system, the so-called two-electrode system (see Figure 7) can be used in current versus potential (I–E) measurements when the passage of current does not change the potential of the RE. This typically means that the current passing through (I_F) times the resistance of the solution (R_S) should give potentials less than 1–2 mV. For example, the two-electrode system can be used when the surface area of the WE is very small, making the I_F in the scale of 1 nA. If this is true, even if the R_S is in the scale of MΩ, the gained results do not experience major complications.[1]

In experiments, when $I_F R_S$ is expected to be high, a three-electrode system (see Figure 8) can be utilized to have reliable measurements. Measurements needing the third electrode can be such that have organic solvents with high resistance or simply, large electrodes. In a three-electrode system, the potential is measured again between the WE and the RE, but the negative effect of the current passing through the RE is prevented with a counter electrode (CE). The CE can basically be any electrode available, because it does not alter the behavior of the WE.
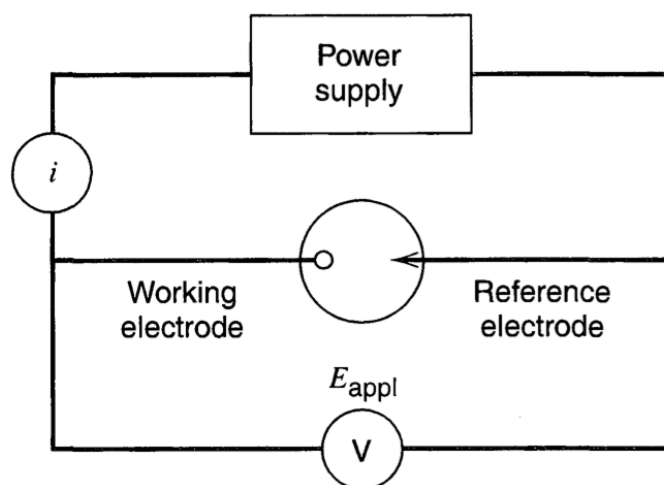

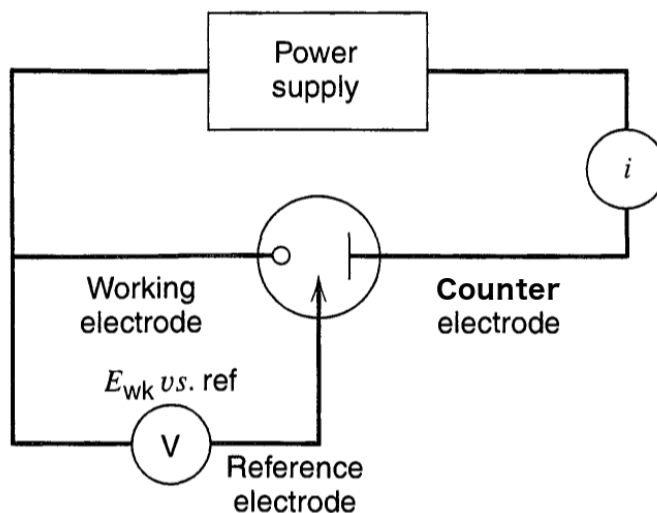**Figure 7:** A two-electrode setup.[1]

Figure 8: A three-electrode setup.[1]

However, it is usually chosen to be an inert metal electrode so that no reactions will form that could have products that might reach the WE. A typical material for the CE is platinum. This measurement setup is the most commonly used setup in all electrochemical measurements.[1]

The starting point for actual measurements is typically the equilibrium potential E_{eq} of the measured system. When the system is altered from this equilibrium, the system is polarized. To indicate how much the system has been polarized, a commonly used quantity is the overpotential

$$\eta = E - E_{eq}, \tag{18}$$

where E is the potential difference between the WE and RE. When the potential is measured against a nonpolarizable RE, a small drop in the voltage called the ohmic drop is always present. The magnitude of this drop is IR_S and it is due to the inherent resistance of the electrolyte. The effect of the ohmic drop can be reduced by minimizing the distance between the WE and the RE in the three-electrode setup. When this distance is smaller, only a small uncompensated fraction of R_S marked as R_U causes the ohmic drop as illustrated in Figure 9. However, the RE cannot be too close to the WE or otherwise shielding effects will start interfering with the measured current. The shielding blocks the current path through the solution and gives uneven current densities. Because of the inevitable presence of the ohmic drop, if the RE is assumed to
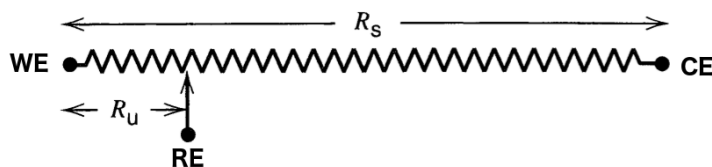
Figure 9: An illustration of when the effect of the ohmic drop is reduced by minimizing the distance between WE and RE.[1]

be ideally nonpolarizable, the relation between the potential applied (E_{app}) and the current (I) in electrochemical measurements is in general

$$E_{\mathrm{app}}(\text{vs. RE}) = E(\text{vs. RE}) - IR_S = E_{\mathrm{eq}}(\text{vs. RE}) + \eta - IR_S. \tag{19}$$

where the terms η and IR_S are related to the flow of the current and R_S and R_U can be used interchangeably depending on the measurement setup. When the current measured at the WE is anodic (i.e. WE is negatively charged) both the overpotential and the ohmic drop are negative and when the WE is experiencing cathodic current, the two terms are positive.[1]

5 Electrochemical methods

In this chapter different electrochemical methods are discussed starting from the simplest chronoamperometry method and then moving on to more complex ones. The intention is to give a theoretical understanding of the methods. For a more experimental approach see Chapter 10 of the experimental section of this thesis or other literature[1,37]. The discussion here is mainly limited to the so-called small *A/V* conditions referring to small electrode area to solution volume ratio. This is essentially true for microelectrodes, where the size of the electrode prevents the reactions happening at the electrode surface from altering the concentrations of the bulk solution. Since the concentrations are not altered, probing measurements on the system instead of altering it are possible. In addition, the responses described are mainly for a simple, fast and reversible redox electrode reaction such as that seen in equations (14) and (15).[1]

In all electrochemical measurements the system is controlled and measured by using a potentiostat. This computer-controlled device is able to maintain the potential difference between the WE and RE stable or control it essentially in any way desired. The control is achieved by having a feedback loop between the potentiostat and the measured system. The control allows the usage of different perturbation methods for probing and studying different properties of the measured system.

5.1 Potential Step Methods

The defining characteristic of potential step methods is that the change between different potentials is abrupt. This means that when changing the potential applied between the WE and RE, a vertical line is seen between the first and second applied potentials. The potential is then maintained constant for a time giving a horizontal line in the potential versus time graph. The shape of the end result reminds that of a step of staircase, where the name of the method type comes from.

In the simplest possible measurement of potential step methods, the potential applied to the setup is abruptly changed once and then kept constant. When the potential is maintained constant, the conditions in the solution change and a current will flow. When this current is measured over time, the method is called chronoamperometry (CA). A typical shape in the response behavior of the current in a faradaic system is exponential decrease. In a system like this, in the beginning all of the electroactive species on the surface will immediately undergo reduction or oxidation when the applied potential is high enough. This sudden change will give a high current, but as time goes on the mass-transport from and to the electrode surface will limit the amount of current able to pass. In addition, as the potential is maintained, the concentration of the original species at the EEI decreases, and the concentration of the reacted species increases. Therefore, less and less current will be detected over time, because the thickness of the layer where the original species has been depleted will increase.[1]

A variation of CA is a method called double potential step chronoamperometry. As the name suggests, instead of doing only one potential step, there are two. After the first potential step, the conditions are maintained constant for a fixed period of time until the potential is returned to the original potential. Just like in CA, the response to the first potential step has a large current response. The reversibility can be seen in the second potential step, because in a perfectly reversible system the current versus time behavior is essentially a mirror image of the

first peak in current, but in the opposite direction on the current axis. This is because after the first step a product will start forming at the electrode surface. When the potential is applied long enough, the concentration of the product is larger than that of the original species at the interface. Then, when the potential is returned to the original, the product cannot exist at that potential. Therefore, the product reacts fast back to the original species giving a large current. As its concentration depletes from the surface, less and less current is detected when time goes on. A method like this, where the reversibility of the system is tested, is called a reversal method.[1]

Both of these chronometric methods mentioned can be altered so that instead of measuring the current over time the current is integrated over time. As the integral of current over time is the amount of charge passed, methods like this are called coulometric. The corresponding methods for CA and double potential step CA are chronocoulometry and double potential step chronocoulometry. In theory also derivative methods could be possible, but they are rarely used as this would increase the noise of those methods significantly.[1]

Also, measurements are not limited only in current versus time behavior. Many methods analyzing current versus potential behavior are commonly in use. The simplest one in the potential step method regime being the sampled-current voltammetry method. Here first several CA measurements are made so that the solution is well mixed between each run. This returns the system to its original status before the measurement as the reacted species at the electrode surface will be removed from the interface. Then, for each measurement the potential step size from the original potential is varied. When the decaying current I at the different potentials is recorded at a chosen time τ the received $I(\tau)$ versus potential curve follows the steady-state behavior discussed before.[1]

5.2 Potential Sweep Methods

Even though it is possible to gain a three-dimensional plot of the I–t–E behavior of a system using several potential step measurements, it can be very tedious as many measurements with small step size differences would have to be used. An alternate method is to change the potential applied as a function of time, which at a qualitive level has the same result. Common method of altering the potential is linearly as a function of time. The rates can vary from 10 mV/s to 10^6 mV/s, when using microelectrodes as with macroelectrodes the highest rates are around 1000 mV/s. Potential sweep methods are usually done in a solution with a standard redox couple

to inspect the electrode's properties. The simplest method used in this manner is called linear sweep voltammetry (LSV). In it, following the red points shown in Figure 10, starting from a potential, that is typically a positive value or zero (point **A**), a single-direction sweep is made until a decided potential (point **D**). This gives a response with a peak (point **C**) forming after crossing the formal potential of the redox reaction. The peak diminishes even though the potential keeps increasing, because the mass-transfer of the original species limits the reaction speed giving a smaller current as the diffusion layer becomes larger. As it can be seen from the Figure 10, LSV can be expanded on by a backwards scan. When the backwards scan is added, the method is called cyclic voltammetry (CV).[1,42]

Assuming that the reduced species is absent in the beginning of the measurement, the detected current of potential sweep methods is always dependent on measurement parameters following the equation
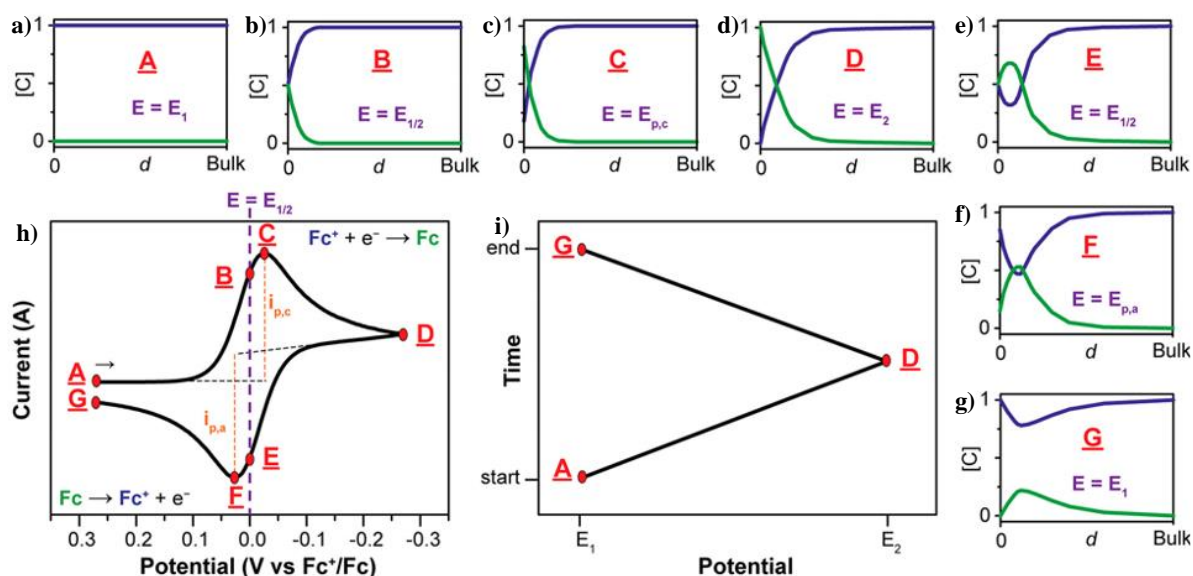

Figure 10: a)-g) Show the concentration profile of the oxidized (blue) and reduced (green) species as a function of the distance from the electrode, **h)** shows the shape of a cyclic voltammogram in the *I–E* plot with an arrow indicating the scan direction and **i)** shows the relation between time and potential in a cyclic voltammetry measurement. Note that the potential increases to the left in the voltammogram. This is the US convention, but for example, the data of the experimental section of the thesis uses the IUPAC convention that has potential increasing to the right. Adapted with permission from reference[42],
© 2017 ACS, https://doi.org/10.1021/acs.jchemed.7b00361

$$I = nFAC_O^* (\pi D_O \sigma)^{1/2} \chi(\sigma t), \tag{20}$$

where C_O^* is the concentration of the oxidized species in the bulk solution, D_O the diffusion coefficient of the oxidized species, $\chi(\sigma t)$ a dimensionless number representing the normalized current and

$$\sigma = \frac{nF}{RT} v, \tag{21}$$

where v stands for the used scan rate. From these two equations it is apparent that the current depends on the electrode area (A), analyte concentration in the bulk of the solution (C_O^*) and the square root of the used scan rate ($v^{1/2}$). Therefore, when presenting measured data of potential sweep methods, the data is often normalized using the area and the other two parameters are presented.[1]

From the Equation (20), the peak current I_P can be calculated numerically. The function $\pi^{1/2}\chi(\sigma t)$ reaches its peak value at 0.4463. When doing this substitution for Equation (20) and implementing conditions that $T = 25$ °C and presenting A in cm^2, D_O in cm^2/s, C_O^* in mol/cm^3, v in V/s and I_P in A, the peak current is[1]

$$I_P = (2.69 \cdot 10^5) n^{3/2} A D_O^{1/2} C_O^* v^{1/2}. \tag{22}$$

In contrast to potential step methods, in potential sweep methods a charging current I_C is always flowing, because of the always changing potential. The magnitude of this current is

$$|I_C| = A C_d v. \tag{23}$$

When comparing equations (22) and (23) it can be seen that I_P is dependent on $v^{1/2}$, but I_C is dependent on v. This means that with higher scan rates the charging current becomes more dominant and important. By combining these two equations, the ratio between the two currents will be gained:

$$\frac{|I_C|}{I_P} = \frac{C_d v^{1/2} (10^{-5})}{2.69\, n^{3/2} D_O^{1/2} C_O^*}. \tag{24}$$

If the value of v is remarkably high or C_O^* is very low, the shape of the voltammogram will distort. This distortion will change the ratio between the two currents essentially flattening the shape. Because potentiostats generally alter the $E + IR_U$ instead of the actual potential between the WE and RE (see Equation (19)) and the I changes as a function of time, the error caused by the Ohmic drop varies. With a large enough Ohmic drop $I_P R_U$ the potential experienced by the WE will not really be linear in nature. This will move the potential at which the peak current is detected. However, in most biosensor applications this should not be a problem since the used sweep (or scan) rates are within the mV/s range[43] and with microelectrodes the limit is around 10^6 V/s.[1]

5.2.1 Cyclic Voltammetry

Cyclic voltammetry (CV) is a popular and powerful tool for mapping electron transfer-initiated (e.g. catalysis) or redox reactions. It can be considered to be the potential sweep equivalent of the double potential step CA, because it is also a reversal method. In comparison to the LSV, CV is essentially (at least) two symmetric LSV measurements done back to back but changing the scan direction at a certain potential (i.e. the switching or vortex potential). It can be possible to use a different scan rate from the initial rate when doing the reversal, but this is almost never used. A typical shape of a cyclic voltammogram can be seen in Figure 10h) with the symmetric triangular potential wave presented in Figure 10i). The peaks of the voltammogram form when the redox agent in the solution is being reduced (the potential is decreasing, point **C**) or oxidized (the potential is increasing, point **F**). The measurements are typically done so that the initial scan direction is towards a more negative potential giving the cathodic current. This makes the reversal scan into the direction of a more positive potential that gives the anodic current. The switching potential (point **D**) is therefore typically a negative value. Just like in the LSV, the current grows smaller after a certain potential because of the movement speed of the reacted species is limited. The reacted species cannot move fast enough away from the electrode and the Helmholtz planes become saturated. After this, only the diffusion of the not-reacted species controls the current. The reactions happening at the electrode are described by the Nernst equation, which gives the relation between the cell potential E, the system's standard potential E^0 and relative activities of the reduced (a_{Re}) and oxidized components (a_{Ox}) at equilibrium:

$$E = E^0 + \frac{RT}{nF}\ln\frac{a_{\mathrm{Ox}}}{a_{\mathrm{Re}}} = E^0 + 2.3026\frac{RT}{nF}\log_{10}\frac{a_{\mathrm{Ox}}}{a_{\mathrm{Re}}}, \tag{25}$$

where R is the ideal gas constant, T the temperature, n the stoichiometric number of electrons involved in the electrode reaction and F the Faraday constant. However, this can be approximated by changing the activities to more experimentally available parameters, the concentrations and substituting the standard potential with the formal potential $E^{0\prime}$

$$E = E^{0\prime} + \frac{RT}{nF}\ln\frac{[\text{Ox}]}{[\text{Re}]} = E^{0\prime} + 2.3026\frac{RT}{nF}\log_{10}\frac{[\text{Ox}]}{[\text{Re}]} \qquad (26)$$

The formal potential depends on the experimental setup and is always specific to it. It is often approximated by experimentally determined $E_{1/2}$ value (points **B** and **E**). This is essentially the halfway point between the reduction and oxidation peaks on the x-axis.[42]

In CV measurements it is important to choose carefully the solvent, electrode and supporting electrolyte in respect to the analyte. All these factor into the available potential window that can be used in experiments. For example, the available potential window for carbon-based electrodes is approximately from -1.0 to 1.0 V. Another important thing is that the solvent is able to completely dissolve the analyte and large concentrations of the supporting electrolyte. This is necessary, because all theoretical models ignore convection and migration of the analyte and only take into account the diffusion. Convection is the movement of the analyte by physical factors (e.g. stirring or vibrations) and migration is the movement by an electric field. Convection can be prevented by simply not stirring the electrolyte. On the other hand, the migration of the analyte can be prevented with high concentration of the supporting electrolyte. The high concentration makes it statistically more probable for the supporting electrolyte to move to neutralize the charge instead of the analyte. Thus only the diffusion causes mass transfer of the analyte.[42]

Before the measurements can be begun, it is important to have the working electrode clean. For this, a so-called pretreatment is required. With metallic working electrodes the cleanliness can be ensured with mechanical polishing of the electrode and any left-over particles can be removed by ultrasonication. After this, absorbed species are commonly removed by running several CV cycles until the cycles overlap.[42]

As discussed before, during measurements the measured potential might not be exactly the same what the solution experiences. Because of the resistance of the solution, the Ohmic drop between the WE and RE can occur. This means that because the measurement setup cannot compensate for the whole resistance of the solution, a smaller potential is measured. In CV, an indication that the Ohmic drop is happening, is increased peak to peak separation in the cyclic voltammogram. As with LSV, the drop follows Ohm's law $E = IR$, where E is potential, I current and R resistance. Therefore, the effect can be compensated by reducing the size of the WE, only using slow scan rates (lower I) or by reducing the resistance of the solution (smaller R).[42]

When analyzing voltammograms, the usual parameters of interest are the ratio of the peak currents for the anodic and cathodic peaks (I_{Pa}/I_{Pc}) and the peak-to-peak distance on the potential axis ($E_{Pa} - E_{Pc}$, also ΔE_P). The anodic (i.e. the oxidation) current and peak happen when the potential applied is scanned towards higher/positive potentials and the cathodic (i.e. reduction) one, when going towards lower/negative potentials. For Nernstian systems the ratio I_{Pa}/I_{Pc} should always equal to 1 independently of parameters such as scan rate, switching potential or diffusion coefficients as long as the switching potential is greater than $35/n$ mV over the E_{Pc}. ΔE_P should also be a constant for Nernstian systems with a value of 2.3 RT/nF, which is $59/n$ mV at 25 °C. However, in reality this value is affected slightly by the switching potential. In addition, with repeated cycles I_{Pc} decreases and I_{Pa} increases changing ΔE_P to be $58/n$ mV at 25 °C. In order to calculate the I_{Pa}/I_{Pc} ratio, one would have to be able to separate the I_C from I_P as the charging current is essentially a baseline that should be corrected. But if only a voltammogram is presented, this can be difficult. Therefore, a treatment described by Nicholson[44] that uses the uncorrected peak current in relation to zero current (i.e. the absolute measured current value) $(I_{Pa})_0$ and the current at the switching potential $(I_{sp})_0$ should be used:[1]

$$\frac{I_{Pa}}{I_{Pc}} = \frac{(I_{Pa})_0}{I_{Pc}} + \frac{0.485\,(I_{sp})_0}{I_{Pc}} + 0.086 \tag{27}$$

5.3 Pulse Voltammetry

Historically speaking pulse voltammetry methods have been developed from polarographic measurements that were conducted using mercury-based electrodes. These electrodes include the dropping mercury electrode, the static mercury drop electrode and the hanging mercury drop electrode. The methods used with these electrodes are such as tast polarography, normal pulse polarography and differential pulse polarography, but they cannot be used with other types of electrodes. Therefore, only the more flexible and modern pulse voltammetry methods such as normal, reverse and differential pulse voltammetry and square wave voltammetry will be discussed here.

The common factor for all pulse voltammetry methods is that the current response is sampled only at a certain point in the perturbation in contrast to the previous methods, where the sampling can be considered continuous. The simplest pulse voltammetry method is normal pulse voltammetry (NPV). In it, a base potential E_b is selected so that no electrochemical reactions happen at it. This potential is maintained constant for a waiting period of 0.5 to 5 s that is of fixed length for a full measurement. Pulses of 1 to 100 ms to a potential in the direction of the formal potential $E^{0\prime}$ are made after the waiting period. For each consecutive potential pulse, the change in the potential (ΔE, i.e. the pulse amplitude) is increased. The increase of ΔE per cycle is usually a couple of mV. The current is measured at the end of the pulse, just before returning back to the E_b. Just like in CA, the response for a single abrupt change in the potential (in this case the pulse) is a big increase in current that decreases exponentially. The sampled currents are presented as a continuous response as a function of the pulses' potentials. For this plot to show a well-behaved response (see Figure 6), NPV relies on the fact that the diffusion layer is restored to its initial state after each pulse (i.e. during the waiting period). As normal stationary electrodes are depleting the reactant from the diffusion layer, instead of seeing the well-behaved response, a peak will be seen around the $E^{0\prime}$. The current response is diminishing at later potentials for the same reasons as described with LSV. To prevent this from happening and to restore the diffusion layer for each cycle, either chemical, convective or diffusive renewal can be used. Chemical reversibility is not limited to fast and perfectly reversible reactions, as the E_b is maintained for a long time in comparison to the pulses' durations. Therefore, only the possibility of the reaction to go backwards over some time at E_b is sufficient. For convective renewal, the solution can be stirred so that the original reactant is replenished at the EEI from the bulk of the solution even though if the reaction itself cannot be reversed. However, this can cause alterations in the current sampled during the pulse. Yet, this

error is usually relatively small or irrelevant as the short pulses create a diffusion layer that is restricted to the EEI or calibration can be used. If neither of these methods can be used, diffusive renewal essentially means that the waiting period is adjusted to be long enough that diffusion can renew the diffusion layer.[1]

Reverse pulse voltammetry (RPV) is the reversal method version of NPV. In comparison to NPV, the RPV has a different E_b, that is at a potential past the $E^{0\prime}$ so that the reaction happening at the EEI is already in its diffusion-controlled state. The pulses are then made in the reversed direction in contrast to NPV so that the current detected is from the reaction going backwards. The pulse shape, current sampling and plotting are all identical to NPV and the resulting response is similar in shape, but it seems to have been shifted downwards: lower currents at high potentials and negative currents at the lower potentials are measured. This is because at the E_b of RPV only a small diffusion-controlled current is detected and when the reaction is traversed to the direction of the reactant, a current in the opposite direction is formed. RPV can be used to inspect the stability of the product where as NPV is more suitable for concentration measurements. In addition, clear similarities between NPV, RPV, sampled-current voltammetry and double potential step CA can be seen, and they have similar theoretical treatments.[1]

Improvements on the sensitivity of the previous pulse voltammetry methods have been achieved by using differential pulse voltammetry (DPV). DPV does not have a constant E_b, but instead the pulse height (10 to 100 mV) and shape are always maintained constant. E_b increases after each pulse as ΔE is smaller after the pulse than in the beginning of the pulse. Also, as contrast to the previous methods, two current sampling points are measured per cycle. The first one at time $\tau\prime$, just before the pulse and the second one just at time τ before the end of the pulse. The resulting plot is calculated from these two currents: $\delta I = I(\tau) - I(\tau\prime)$, which gives the word differential to the method's name. The shape of the response is a peak around the potential region of $E^{0\prime}$ instead of the wavelike response of the previous methods. This shape forms because before the applied potential reaches the $E^{0\prime}$ region, the current does not change with the pulses ($\delta I \approx 0$). As the experiment goes on, around $E^{0\prime}$ the pulse causes an increase in the measured current due to faradic processes. When this region is passed, the base potential is already causing the electrode reaction to be at its maximum, diffusion-controlled rate. Therefore, the pulses cannot increase the reaction rate and increase the current and $\delta I \approx 0$ once again. Despite the fact that with traditional electrodes the diffusion layer cannot be renewed,

DPV works well for them. When a DPV measurement goes on, the increasing base potential creates a thicker diffusion layer with apparent bulk concentrations. When the pulses are used to probe this layer, the diffusion layer is altered, but with reversible reaction kinetics the base potential is able to restore the situation for each cycle because of the small amplitude of the pulses. However, the background is typically dominated by the faradic currents forming due to the interaction of the electrode and electrolyte and this can result in a significant amount of noise. But because the usage of fast pulses and short waiting periods is possible, this can be improved on in the method called square wave voltammetry.[1]

5.3.1 Square wave voltammetry

Square wave voltammetry (SWV) is described as the pulse voltammetry method, that takes and combines the good properties of almost every other pulse voltammetry method mentioned so far. SWV is also considered as the most versatile and newest method of this group.[1,45] Here the working principle of SWV and the theoretical response in the case of a simple fast and reversible electrode reaction will be discussed. For other and more complex cases the reader is guided to read the extensive publication by Mirceski *et al.*[46].

The waveform that is used in modern SWV measurements is presented in Figure 11. From the figure, it is easy to see where the name of the method is coming from. Exactly like with other pulse voltammetry methods, the system goes through several consecutive cycles of stimulation. The specialty of SWV in comparison to other pulse voltammetry methods is that the diffusion layer is never renewed as the pulses forward (reductive) and backward (oxidative) are of the same duration. The Figure 11 shows also the important parameters of SWV measurements: E_{st} is the starting potential, E_{sw} the pulse height (positive for forward and negative for backward pulses) that is known as the square wave amplitude, I the current forming at the corresponding pulses forward (f) and backward (b), ΔE the increase in potential per cycle (i.e. potential increment), τ the staircase period (i.e. the time it takes from the beginning of the forward pulse to the end of the backward pulse) and t_0 the optional delay time to gather reactant to the electrode surface before starting the measurement.[1,46]

The scan rate of SWV is defined as $\Delta E/\tau$ and just like discussed with potential sweep methods, the faster the scan rate the larger the measured currents are. Considering the currents measured, it is typical for SWV methods to use a sampling window in contrast to previous methods' sampling, where only one measurement point is used. This sampling window is measured from
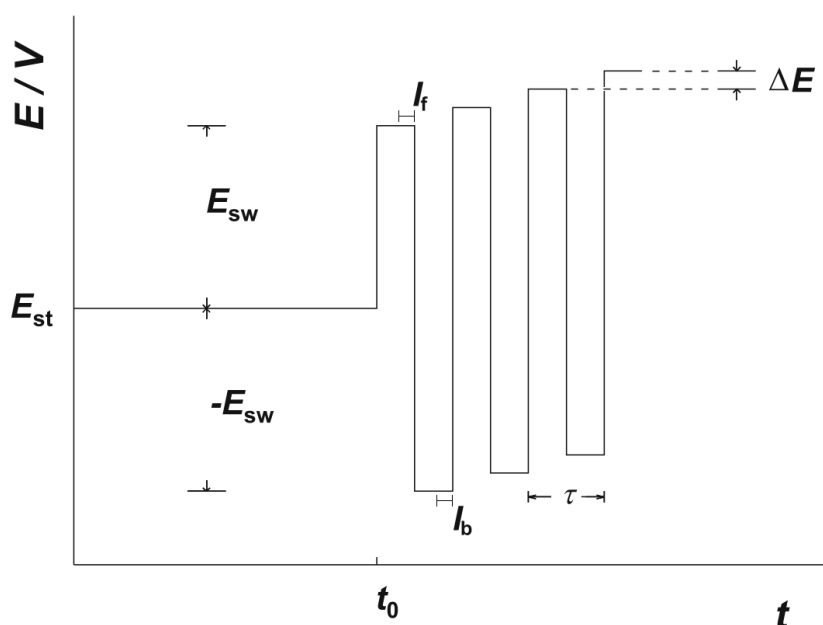
Figure 11: Potential scheme for the excitation in modern square wave voltammetry.[46]

a small fraction (couple of µs) of the pulses' duration at the end of the pulse and the current values of it are averaged to gain I_f and I_b. The advantage of using a window instead of just one point is that this reduces the noise of the final result of the measurement. I.e. a wider sampling window gives a smoother response curve, that is desirable as a common problem with SWV is high electrical noise in the signal. Therefore, also other smoothing procedures are often used.[1,46]

In SWV the recorded response is a differential from the forward and backward signals

$$\Delta I = I_f - I_b, \tag{28}$$

but because the individual signals themselves have their own diagnostic value, all three signals are typically stored and presented. Even though the resulting data from SWV is normally drawn as a line, the graph in reality is a collection of individual measurement points and the line connecting them does not have any theoretical basis. Each measurement point is presented as the function of their corresponding staircase potential. This potential is the average potential of the forward and backward pulses within one cycle. The shape of the response in SWV for a fast and reversible electrode reaction is presented in Figure 12. Here the presented data are calculated net dimensionless responses that are related to the actual measured currents through
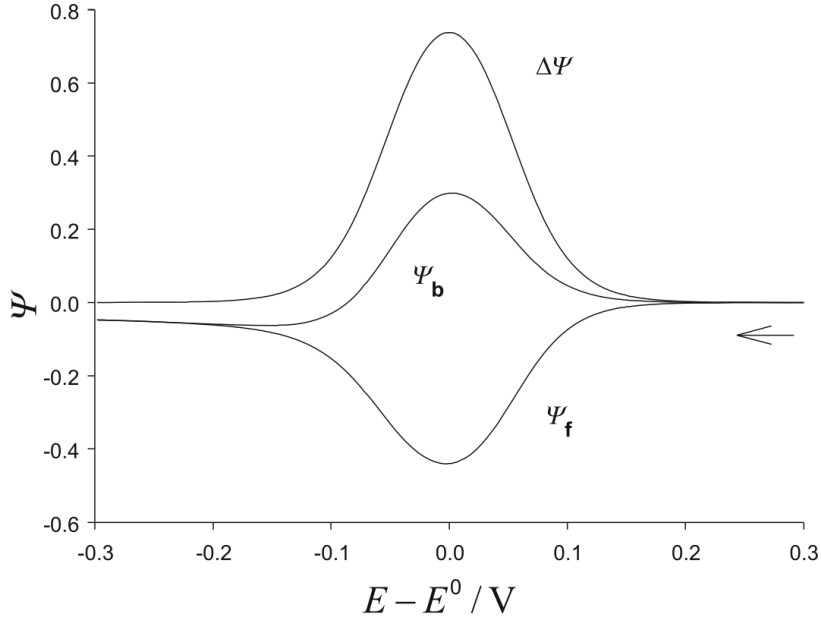
35

Figure 12: A calculated dimensionless net current SWV response ($\mathbf{\Delta\Psi}$) of a fast and reversible reaction with its components for the forward ($\mathbf{\Psi_f}$) and backward ($\mathbf{\Psi_b}$) currents displayed. The arrow indicates the scan direction.[46]

$$\Delta\Psi = \frac{-\Delta I}{nFAC_0^*\sqrt{Df}},\qquad(29)$$

where D is a diffusion coefficient and $f = 1/\tau$, which is called the frequency of the signal (essentially the frequency of the stimulation). The corresponding forward (Ψ_f) and backward (Ψ_b) values are calculated by replacing ΔI with either I_f or I_b, respectively. This representation is used, because of the derivation of the required formulas (shown elsewhere[46]) gives equations in this unit for the responses. The voltammograms resulting from SWV are characterized by peak current and the corresponding staircase potential. These would be the peak net current ΔI_p and the peak net potential E_p for the total net response. The reductive and oxidative responses are naturally characterized respectively with their corresponding minimum and maximum currents and staircase potentials. ΔI_p can be calculated from the response presented in Figure 12 by rearranging Equation (29) into

$$\Delta I_p = -nFAC_0^*\sqrt{D}\Delta\Psi_p\sqrt{f},\qquad(30)$$

where $\Delta\Psi_p$ is the dimensionless peak net current. A characteristic of these fast and reversible systems is that the peak potential (E_p) for any of the responses does not change as a function of the square wave frequency f.[46]

5.4 Impedance-based Methods

Up until now, the methods presented always perturb the system so that it is driven far away from equilibrium. This has given us a transient signal as the system has been altered. Another approach is using a perturbation so small that the system maintains itself in a quasi-stable state. This makes it possible to make precise measurements, because the response of the system can be infinitely stable. Also, since the perturbation is small, the I-E characteristics of the system do not have to be well-known. This is because simplifications to a linear stable state response can be used.[1]

There exist several methods taking advantage of the concept of impedance. Essentially all voltammetry methods can be done with an alternating current (AC) superimposed on the direct current (DC) creating AC voltammetry methods. These methods are, for example, linear sweep AC voltammetry and cyclic AC voltammetry. Despite of these hybrid methods existing, here only electrochemical impedance spectroscopy will be explored in more detail after the description of impedance. For the descriptions of the other methods, see the original publication.[1]

5.4.1 Impedance

To understand what impedance is, some knowledge of basic AC circuits is required. Therefore, a short discussion of the basics of AC circuits is presented. First of all, a sinusoidal AC signal of the frequency f can be described as

$$E = A_E \sin \omega t, \tag{31}$$

where E is the potential as a function of time, A_E the amplitude of the signal, ω the angular frequency ($2\pi f$) and t time. In reference to the potential, the current can be at a different phase depending on the system. The difference in phase θ is called the phase angle. Therefore, the detected AC current I can be described as

$$I = A_I \sin(\omega t + \theta), \tag{32}$$

where A_I is the amplitude. When an AC signal is used to perturb the simplest AC circuit, a single resistor, the relationship between the potential and current in phasor representation follows the Ohm's law. So, for the resistor it is

$$\dot{E}_R = \dot{I}R. \tag{33}$$

In this case, there is no phase difference between the current and potential. If the only component of the circuit is a capacitor with capacitance C, the current detected is

$$I = \omega C A_E \cos \omega t = \frac{A_E}{X_C} \sin\left(\omega t + \frac{\pi}{2}\right), \tag{34}$$

where $X_C = 1/\omega C$ is called the capacitive reactance. As it can be seen, the phase angle has the value $\pi/2$ (90 °). Because the angle is positive, when imagining these phasors in the circle representation, the current would lead the potential by the phase angle. Now that these two phasors have a straight angle between them, a plane can be defined with them using complex notation. This is done by introducing the complex number $i = \sqrt{-1}$ to the phasors. With this, for the capacitor the relationship of the potential and current phasors can be represented as

$$\dot{E}_C = -iX_C\dot{I}. \tag{35}$$

Now, if the resistor and capacitor are in series, by using equations (33) and (35), at a potential $\dot{E}$, the behavior is

$$\dot{E} = \dot{E}_R + \dot{E}_C = \dot{I}(R - iX_C) = \dot{I}Z, \tag{36}$$

where Z is the impedance. Practically impedance is a generalized resistance and Equation (36) is the generalized Ohm's law. The relationships between all the variables related to impedance is illustrated in Figure 13.[1]
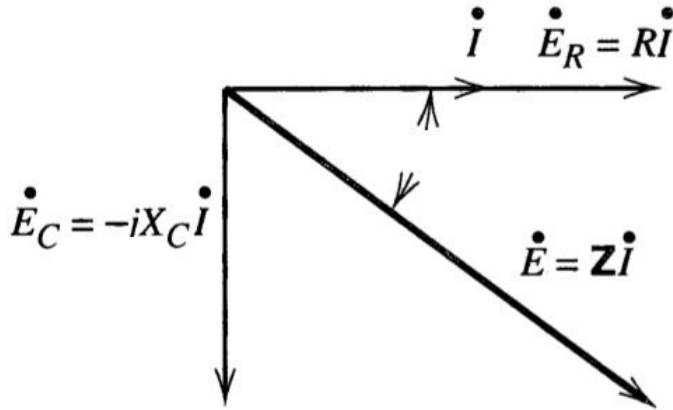
Figure 13: Phasor diagram illustrating how the variables related to impedance are tied to one another in a circuit with a resistor and a capacitor in series.[1]

5.4.2 Electrochemical Impedance Spectroscopy

Electrochemical Impedance Spectroscopy (EIS) studies the EEI by means of its impedance. The description of the measurement technique and the data plotting are discussed in the experimental part of this thesis, in section 10.2. To avoid repetition, only the theoretically predicted response to an EIS measurement is discussed in this section. This is done to the extent that to help understand the starting point of the following discussion, it is recommended to see section 10.2 first.

Continuing from the situation of Equation (36), in an EIS measurement the total measured response Z is a combination of the system's resistance R_B and capacitance C_B. These give the real and imaginary parts of the impedance so that $Z_\mathrm{Re} = R_\mathrm{B}$ and $Z_\mathrm{Im} = 1/\omega C_\mathrm{B}$. As it is in the Nyquist plot, the impedance is a function of the frequency according to

$$Z = Z_\mathrm{Re} - iZ_\mathrm{Im} = R_\mathrm{B} - \frac{i}{\omega C_\mathrm{B}} \tag{37}$$

From this equation it is possible to separate ohmic solution resistance R_Ω, differential capacitance of the double layer C_d, solution resistance R_s and pseudocapacity C_s. When in low frequencies ($\omega \to 0$), the relationship between the imaginary and the real part is linear according to

$$Z_{\text{Im}} = Z_{\text{Re}} - R_\Omega - R_{\text{ct}} + 2\sigma^2 C_d \tag{38}$$

with the coefficient

$$\sigma = \left(\frac{1}{nFA\sqrt{2}}\right)\left(\frac{\beta_O}{D_O^{1/2}} - \frac{\beta_R}{D_R^{1/2}}\right) \tag{39}$$

where β is a parameter that depends on the kinetics of the system for the corresponding species. This response is controlled by the Warburg impedance, which is diffusion controlled. It can be described as a resistance due to mass-transfer. However, because in higher frequencies the double layer capacitance C_d and charge transfer resistance R_{ct} become more dominant, high frequency response has to be inspected separately. In high frequencies the relationship follows

$$\left(Z_{\text{Re}} - R_\Omega - \frac{R_{\text{ct}}}{2}\right)^2 + Z_{\text{Im}}^2 = \left(\frac{R_{\text{ct}}}{2}\right)^2. \tag{40}$$

This gives a circular plot centered at $Z_{\text{Re}} = R_\Omega + R_{\text{ct}}/2$ and $Z_{\text{Im}} = 0$ with a radius of $R_{\text{ct}}/2$. The shape can be explained intuitively so that it is only dependent on the C_d. At the highest frequencies the imaginary component only has contribution from C_d to the impedance and it is zero. All the resistance present is from the solution's ohmic resistance and the current flowing is charging current. When the frequency decreases C_d becomes apparent. With a low enough frequency, the imaginary part becomes small again due to the current flowing mainly through R_Ω and R_{ct} as C_d causes a high impedance blocking the current. However, the real response usually is not a perfect half circle as Warburg impedance starts to affect the response. In real systems the response is a combination of (38) and (40) as shown in Figure 14.[1]

5.5 Controlled Current Methods

So far, the methods discussed have only been limited to the situation in which the measurement has been made by controlling the potential applied over the interface. However, this is not the only way of making electrochemical measurements, as also the controlling of the current and letting the potential vary is possible. In fact, this requires a simpler measurement setup as no feedback loop between the sample and the device controlling the measurement is required. Only a power supply applying a strong voltage and forcing stable current flow between the WE and
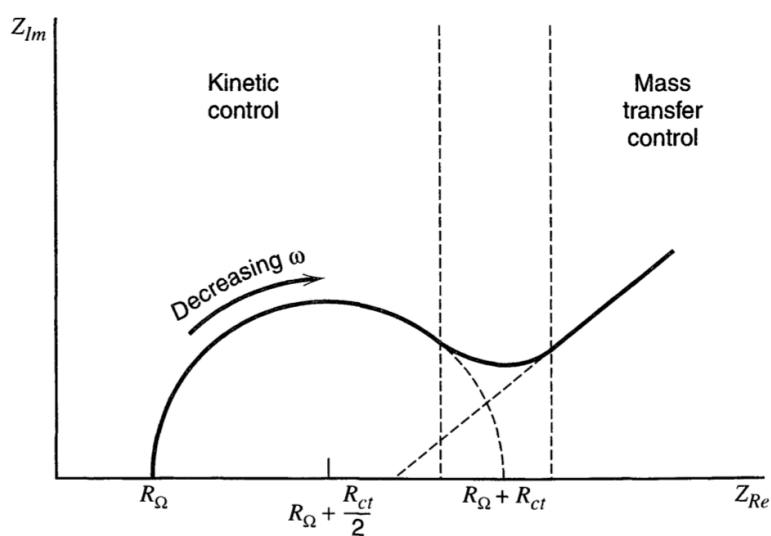
Figure 14: The theoretical response of an EIS measurement.[1]

CE, which is controlled with a resistor, and a potential meter between WE and RE are needed. As there is a current forced through the system, these methods are suitable for example for electrode stripping or solution depletion of reactive species. Because of the always present current, the system is shifted very far from equilibrium. In addition, the current causes double layer capacitive properties to be larger than in potential controlled measurements and the capacitance is changing when the measurement proceeds. This results in data that is difficult to be corrected.[1] Therefore, even though it is important to note the possibility of current control, it would seem like that current controlled methods are not suitable methods for biosensing and will not be discussed further here.

6 Electrochemical Methods in Biosensing

In any chemical sensor, the principle working method is the same. An analyte, that can, for example, be a chemical compound or a biological molecule, is detected by a receptor. The receptor is chosen so that it has a preferably specific interaction with the desired analyte or a group of analytes. When talking about a biosensor, the analyte is a biomolecule. The chemical information from the receptor is then made into a measurable signal by a transducer material. The transducer can be, for example, a graphene-based material.[47] Electrochemistry comes into play with chemical sensing in the measuring and interpretation of the signal given by the transducer material. Here, recent research papers are discussed as examples for using CA, LSV, CV, EIS, chronocoulometry, DPV and SWV with a very brief historical background.

One of the earliest biosensors was proposed already in 1962 by Clark and Lyons[48] and it worked using electrochemical methods. The proposed measurement setup used a two-electrode setup with a pH or oxygen sensitive WE and a platinum RE. It used an enzyme to transform glucose into gluconic acid. This reaction caused a change in the pH of the solution in which the WE and RE were. During this reaction, oxygen was consumed, and CA was used to detect the amount of oxygen used.[49]

Even nowadays, the largest market of medical analysis in the field of biosensors is glucose sensing[50]. An example of a more modern version of glucose sensing could be a device presented by Kong *et al.*[51]. They have proposed a novel disposable paper-based design for glucose sensing in blood samples with no required pretreatment. Although their publication's novelty is in the fabrication method and materials of the device, they also do use DPV for the electrochemical measurements for the design to work. The device itself was fabricated following an earlier publication[52]: First, in a dispersion, a mixture of graphene and polyaniline was created and modified by growing Au nanoparticles in it. This dispersion was stabilized using chitosan and mixed with a solution containing glucose oxidase enzyme. A drop of this final mixture was then put onto and dried on top of a commercial screen-printed carbon electrode to modify it. To prevent losing the enzyme, an additional layer of Nafion was added on top of the electrode. This modified electrode was used as the WE in a three-electrode setup. The RE was a Ag/AgCl electrode and the CE a carbon ring. The electrochemical measurements with the DPV were conducted by scanning from 0.0 V to -0.7 V with a small pulse amplitude of 15 mV and pulse length of 20 ms, but the length of the wait period between the pulses is not given. Their DPV results showed a decrease in the peak intensity around the $E^{0\prime}$ with increased glucose concentrations. They were also able to show with DPV that each material added in the electrode modification actually increased the peak intensity for DPV (higher currents), which they claimed to increase the sensitivity of the method.

In a work by Bonnani and Pumera[4], electrochemical transduction was used in a DNA detector for diagnosing misfunction in an allele connected to Alzheimer's disease. A dispersion of three to four-layer graphene was used to create electrodes. The room temperature dried electrodes were functionalized with hairpin-DNA with physical adsorption and were used for EIS measurements. The measurements were conducted within a frequency range of 0.1 MHz to 0.1 Hz with a perturbation amplitude of 10 mV and an applied potential bias of 0.15 V. In their

results the authors say that their method using EIS was so sensitive that they were able to detect mutations of the size of a single nucleotide in DNA sequences. The change was detected by using equivalent circuit fitting on their impedance data. When the hairpin-DNA hybridized with a DNA sequence with a mutation, the decrease was less significant than with a non-mutated DNA sequence. However, it is interesting to point out that Bonnani and Pumera[4] were able to distinguish how the resistance of the solution and charge transfer resistance affect the system separately despite the fact that they are essentially two resistances in series in the Randles equivalent circuit. This is made possible with the fitting done on the EIS data.

Bonnani and Pumera[4] also used chronocoulometry to study the hybridization mechanism of the hairpin-DNA. By extrapolation of the measured data, the results showed that the surface concentration of the hairpin-DNA at the electrode did indeed decrease when complementary DNA were introduced to the solution. The authors say that they used electrochemistry-based sensing as a preferred method over an alternative fluorescence assay, because of the possibility of future miniaturization for point-of-care diagnostics.

In addition to medical monitoring, a field that is expected to see a lot of growth is wearable biosensors for commercial consumer use. A recent review[49] on wearable biosensors states that recently most of the reports on epidermal wearable biosensors (i.e. biosensors that are put in contact with skin) use electrochemical or colorimetric methods in transducing the signal. However, apparently other methods are also used. One epidermal wearable biosensor using electrochemical methods is a temporal tattoo that was used to monitor lactate levels in human epidermal biofluids.[3] These biofluids consist mainly of sweat. The screen-printed biosensor tattoo had dispersed carbon fibers in its ink, and it consisted of a three-electrode setup similar to the device of Kong *et al.*[51]: a lactate oxidase functionalized WE, Ag/AgCl paste RE and a carbon ink CE. In the characterization of the device, LSV was used to find at what potential the device should be used. After the selection of the final operating potential, CA measurements were used in the actual lactate monitoring. The measurements showed selectivity so that an increased current was detected in the CA with increased lactate levels.

As a more of a curiosity, but continuing with enzymes, in a paper considering a method to measure H_2O_2 concentrations Zhou *et al.*[43] use a good variety of different electrochemical methods. The methods are used in characterization and utilization of an enzyme called sarcosine oxidase (SOX). Its direct electrochemistry had not been previously successfully utilized when

immobilized on a surface.[43] They modified a glassy carbon electrode (GCE) surface by first adding graphene-chitosan composite to the surface. This was conducted by air drying a graphene flake dispersion in chitosan onto the GCE. Then electrodeposition was used to grow Ag nanoparticles from a solution of $AgNO_3$ and NH_4NO_3 onto the electrode. The layer of Ag nanoparticles was coated by drop-casting the SOX enzyme. This material was used as the WE and the other two electrodes were a saturated calomel electrode (SCE) as the RE and a Pt wire as the CE.

Initial characterizations of the modified electrode were conducted by using EIS. This included confirming the immobilization of SOX on the electrode surface and also seeing how the other components of the surface modification actually altered the EEI. The immobilization was seen as an increase in interface resistivity as the enzyme slowed down electron transfer. Further characterization was conducted by CV, which was used to show that the addition of graphene in the structure was indeed needed. Graphene increased the conductivity within the EEI, and it was seen as an increase in the currents measured with CV. The voltammograms were also used to show that only SOX was an electroactive species, as without it, no redox peaks were detected. In addition, a linear dependency between the pH of the electrolyte solution and the redox peak position was discovered from CV. The final measurements for determining the concentrations of H_2O_2 were conducted using CA. A linear region formed in the response seen in the current as a function of the H_2O_2 concentration.[43]

An application going more into environmental analysis has been presented by Du et al.[53]. They combined immunochromatographic separation of a biomarker from a sample with electrochemical quantification of the separated biomarker. The result was a precise method for detecting organophosphorus (OP) compounds. OP compounds are used as pesticides and target the nervous systems of animals. Because of the nature of the compounds, even a small exposure can be fatal. Therefore, very precise detection is of importance. Previous methods to accomplish this require large automated laboratory equipment, but this paper reports a portable point-of-care device. This was done by having two parallel lateral flow devices, where a biomarker would be separated by attaching it to the test zone of the lateral flow device. Altered levels of this biomarker's concentration is a direct indication of the presence of OP compounds. From the test zone, the biomarker was then transferred to a commercial carbon nanotube modified disposable three-electrode measurement setup. By measuring the biomarkers from two parallel lateral flow devices, one of them was possible to be used as a background. This eliminates the

need for a control sample and just the difference between the two parallel samples gives the concentration of the analyte. The SWV measurements were conducted by scanning from 0.1 V to 0.8 V with a step potential of 0.4 mV, pulse amplitude of 25 mV and with a pulse frequency of 15 Hz. The authors report that by having a higher concentration of the biomarker in the solution, a more intense peak in SWV can be detected. Their data indicates that a linear dependency is present at concentrations as low as 0 to 10 nM.

7 Summary and Conclusions of the Literature Review

As shown in this literature review, electrochemical methods are a vast and versatile family of methods that are being used in a variety of applications related to biosensing. The methods' measurement techniques, responses and overall theory was discussed. Since the methods are used in a versatile way, it is useful to be familiar with several methods. This allows the consideration of the benefits and disadvantages of several methods when choosing the measurement method for an application. In comparison to other methods, typical reasons for using electrochemical methods are their good possibilities for commercialization, miniaturization and portabilization of the devices. Electrochemical methods have been used historically and in recent publications in both characterizations of biosensors in vitro and in analytical measurements in vitro and in vivo.

In addition to discussing electrochemistry and electrochemical methods, it was shown that graphene and its derivatives are good and promising materials for applications related to biosensing and electrochemistry. Even though different types of applications require different properties from the materials used, the tunability and flexibility of graphene-based materials seems to be able to answer to many of the challenges presented. Also, the research in the field of creating new graphene-based materials is active and seems to not show any signs of slowing down. It is also important to point out that in addition to electrochemical biosensors that use electrodes, transistor-based biosensors exist. However, they were not the focus here even though in literature, several promising applications utilizing transistors exist. A common example would be a field-effect transistor[47] that has graphene as its gate material.

As this is essentially only an introduction level text into the three fields: graphene-based materials, electrochemistry and biosensing, further reading is suggested for the deeper understanding of the topics.

Experimental Section

8 Introduction

8.1 Motivation

Biosensors are devices designed to measure a biological signal converting the measurement into a signal that is typically electric. These types of devices open countless possibilities for industries such as healthcare, food and process control, environmental monitoring, defense and security. The biggest of them, with a global market worth over 11 billion in euros, is medical diagnosis. This is mainly due to the high demand of glucose detectors for diabetics. However, it is assumed that other applications in the field of personalized medicine are going to have a huge impact on the field of biosensors.[50] One practical example of the need for fast development of new biosensors is the ongoing COVID-19 pandemic, which requires quick detection of the virus in order to identify infected individuals.

A commonly used working principle of biosensors is based on electrodes. For example, for the glucose detectors, a metal electrode functionalized with glucose oxidase made a simple platinum electrode into a powerful analytical tool to detect glucose levels in human samples.[50] Due to technological advances these sensors can be made into more and more affordable, lightweight and easy to use variations.

One of the most commonly used detectors based on electrodes is the pH meter. Typically, the state-of-the-art pH meters are glass electrodes that are ion specific for H^+ ions. The change in the open circuit potential (OCP) is linearly dependent of the pH. Therefore, using solutions of known pH, the meter can be calibrated so that a measured potential can be translated into the corresponding pH.[38] However, these electrodes experience potential shift and require frequent calibrations. In addition, the glass breaks relatively easily, the devices are not the most portable and normally they require a relatively large volume of solution to measure the pH from.

An application in the field of medical devices is a device that measures the pH of a wound when it is healing. Studies have shown that pH does depend on the healing process[54] and therefore measuring it is of interest. Previously, due to the limitations of glass electrodes, the devices used to measure the pH of chronic wounds were a custom flat glass electrode.[54] Therefore, an integrated sensory concept that could monitor infections more diversely (more parameters than just pH), cost efficiently and at point-of-care has been designed.[55] However, the problem with this kind of devices could be their single-use nature, if they were to be integrated in a bandage,

for example. In this case, it would be preferable to use a material that can be disposed for the device.

Graphene oxide has previously been shown to be a material that can be used to create a working pH detector.[56] As a material for the applications discussed above, the advantages graphene has are its biocompatibility and biodegradability. This means that if single-use devices were to be made with graphene being the functional material rather than more traditional electrodes e.g. based on expensive metals, less of these materials that ate potentially toxic for the environment would have to be used. Therefore, in this study a novel graphene-based material is investigated for possible applications in pH measurements.

8.2 Scope of the Work

This experimental work aimed to find a method to measure pH with an electrode made out of a three-dimensional porous graphene-based material. First the material was characterized with three different general methods and two electrochemical methods. After this, four methods for finding a pH sensitivity were studied. These results are presented and discussed. Aspects such as the material's fabrication are not discussed.

This experimental section of this thesis is divided as follows. First, the theory and practice of the used general methods applicable for characterizing graphene-based materials are discussed in Chapter 9. Afterwards the used electrochemical methods that have been discussed in theory within the literature review section are discussed in more practical sense in Chapter 10. Some essential theoretical concepts are covered to rationalize the analysis discussed later in the thesis. Then, in Chapter 11 the experimental equipment, materials and details are described followed by showing the main results and having a discussion over them in Chapter 12. Finally, in Chapter 13, a summary of all of the results and conclusions is presented.

The work reported here was carried out in collaboration with the Advanced Electronic Materials and Devices Group of the Catalan Institute of Nanoscience and Nanotechnology (ICN2) in Barcelona. It was a part of a project funded by the European Union Horizon 2020 Innovation program aiming to develop wearable and disposable electronic devices. The experiments were completed during the autumn of 2019.

9 Characterization Techniques for Graphene-Based Materials

9.1 Raman Spectroscopy

Raman spectroscopy is a popular, fast and effective method to characterize chemical and physical properties of graphene-based materials.[57] More specifically, the method used in this work is vibrational Raman spectroscopy. It is based on using a monochromatic light source to excite the inspected material to a virtual excitation state. Energy from this state is released by three different types of scattering: Rayleigh, Stokes and anti-Stokes. Rayleigh scattering has the same energy (wavelength) as the light used for excitation. However, a small amount of the emitted photons is emitted with a smaller (Stokes) or greater (anti-Stokes) energy than the original. From this shift, the energy difference between the ground state and excited state can be determined.[58] A spectrum of pristine one-layer graphene (1LG) is presented in Figure 15a), which only shows a few of the many different vibrational modes that graphene can have. Most of these modes have been found present in graphite whiskers.[57] The Raman spectrum of graphite whiskers is shown in Figure 15b).[59]
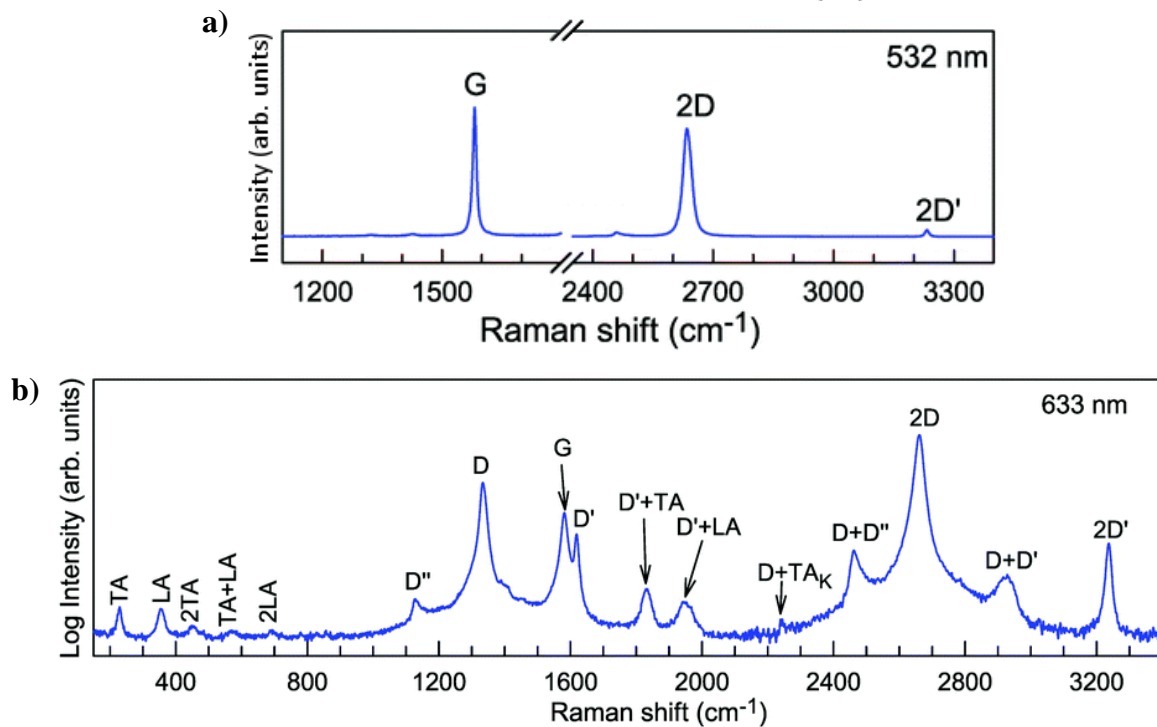

Figure 15: a) Raman spectra of pristine 1LG excited with excitation wavelength of 532 nm. **b)** Raman spectra of graphite whiskers, where all of the expected Raman modes can be observed. The excitation wavelength is 632.8 nm.[57]

The most typical Raman active modes of graphene-based materials are G, D, D´, 2D and 2D´ modes. The G mode (~1582 cm^{-1}) is characteristic for all graphene-based materials. This peak can shift if the material has defects or doping or is experiencing strain or temperature changes. Other characteristic peaks seen even in pristine graphene are 2D (~2700 cm^{-1}) and 2D´ (~3240 cm^{-1}), which are related to the linear distribution of electronic bands in the material and the associated resonance processes. D (~1330 cm^{-1}) and D´ (~1620 cm^{-1}) modes are associated with defects in the material. Therefore, they are not detected in perfectly pristine 1LG. However, D and D´ modes can be detected around the edges of pristine 1LG, because an edge in the material breaks the symmetry of the material.[57] They also have been associated with other types of induced defects such as oxidation level[57], ion-implantation[57] or laser irradiation[60]. The number of defects in the honeycomb lattice of graphene significantly affects the wavelength, size and shape of the measured D and D´ peaks.[57] Eckmann *et al.*[61] found that the intensities of different modes follow a two-stage evolution as the amount of defects is increased. The different stages signify low (stage 1) and high (stage 2) defect concentrations and within these stages the behavior changes significantly, as seen in Figure 16.

Comparison of measured Raman spectra can be difficult due to differences in intensity of peaks between separate samples. A significant difference can happen, for example, because of only a small shift of focus during the measurement. Therefore, comparing absolute values might not be the best way to compare changes in a graphene-based material. Instead, ratios between
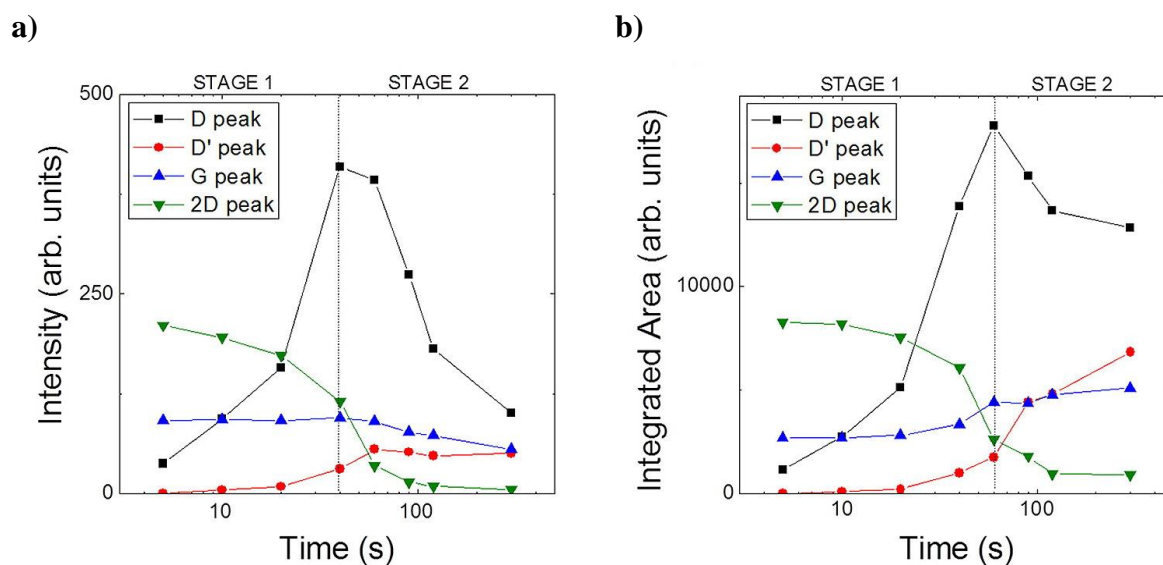

Figure 16: Raman signal's intensity as **a)** amplitude and **b)** integrated area for a sample of graphene that is oxidized with an increasing plasma exposure. Reproduced with permission from reference[61]. Copyright (2012) American Chemical Society.

different peaks of the same spectrum can be used to better describe a material's properties. (e.g. defect concentration or defect nature). Some commonly inspected ratios are the intensity ratios $I(D)/I(G)$ and $I(2D)/I(G)$. Here $I()$ stands for intensity for the Raman mode within the parentheses. However, to avoid the effect of peak broadening or excitation wavelength dependence, the integrated area of the peaks can be used (e.g. $A(D)/A(G)$).[57] In addition to the trends discussed so far, Ma *et al.*[62] have found that the area ratio of $A(D+G)/A(D)$ is directly proportional to the conductivity of reduced graphene-oxide.

A paper by Díez-Betriu *et al.*[63] describes how the reduction of graphene oxide can be monitored by following how several parameters change. The parameters they used are $I(D)/I(G)$, $I(2D)/I(G)$, $w(G)$, $w(2D)$ and $w(D)$. Here $w()$ refers to the full width at half-maximum (FWHM) of the corresponding peak. Depending on the state of reduction of the material, three different phases are present. The behavior of these parameters is presented in Figure 17.

To attain values used for the comparisons, the peaks on the Raman spectra have to be fitted. The used parameters are the position, intensity, FWHM and the peak's line shape. These give information on the vibrational states that correspond to peaks and are used to calculate the area of a peak. For graphene two different line shapes are detected in different types of samples:
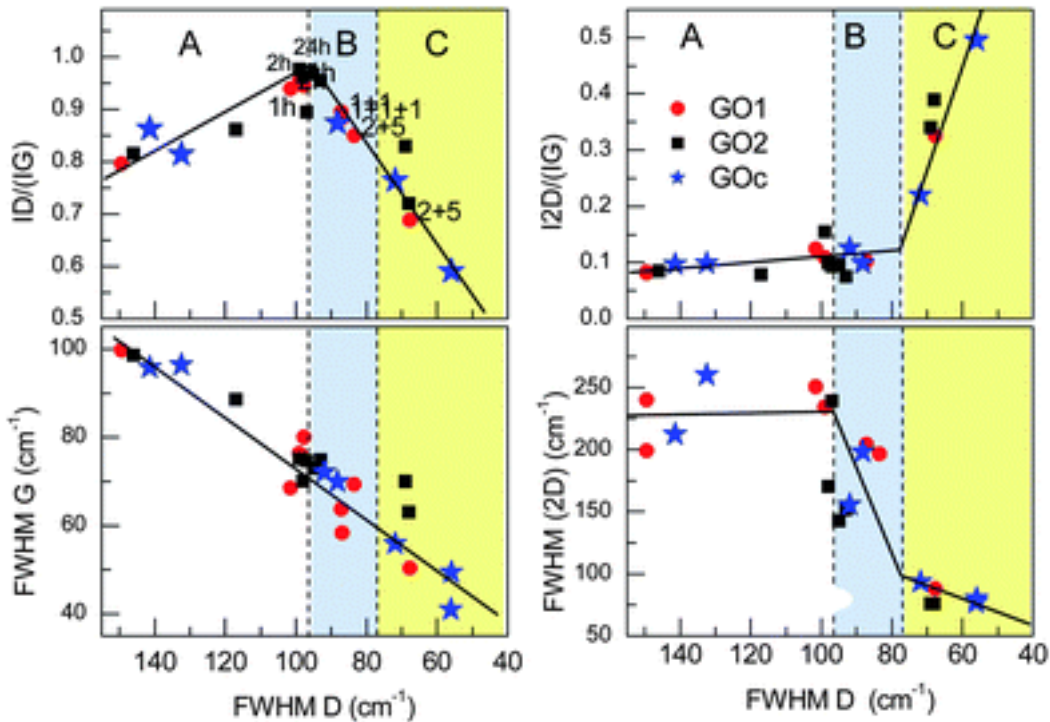

Figure 17: Behavior of several Raman parameters of GO thin films against the FWHM of the D peak during a reduction process. The material is GO on the left and rGO on the right.[63]

Lorentzian and Fano.[57] The Lorentzian is a symmetric and Fano an asymmetric line shape and both of them are fundamental spectroscopic signatures. These line shapes quantify nuclei's, atoms', molecules' and solids' structural and dynamical properties. An in-depth description and discussion of them is presented elsewhere.[64]

9.2 SEM

Scanning electron microscopy (SEM) is a method where instead of visible light a beam of accelerated electrons is used to scan a sample. The advantage is seeing objects with a resolution superior to that of visible light. The diffraction limit of visible light prevents resolving objects smaller than 200 – 250 nm. So, since the wavelength of electrons in a typical SEM setup is around 10 pm, the theoretical resolution is within the picometer range. However, the focusing of electrons with magnetic lenses has some practical issues. Therefore, the resolution of SEM setups is only usually around 50 nm although some manufacturers claim their equipment to be able to reach a resolution of 0.4 nm. But it is not possible, for example, to resolve individual atoms using SEM.[65] A schematic of a scanning electron microscope is presented in Figure 18a).

When accelerated electrons hit a sample in vacuum, several different phenomena can happen, as seen in Figure 18b). The electrons can scatter with the same energy as they had when they hit the surface (elastic scattering) or lose some energy (inelastic scattering). The differently scattered electrons can give information about the composition, topography, density and crystal structure of the sample. Depending on the sample's properties or material, different amounts of
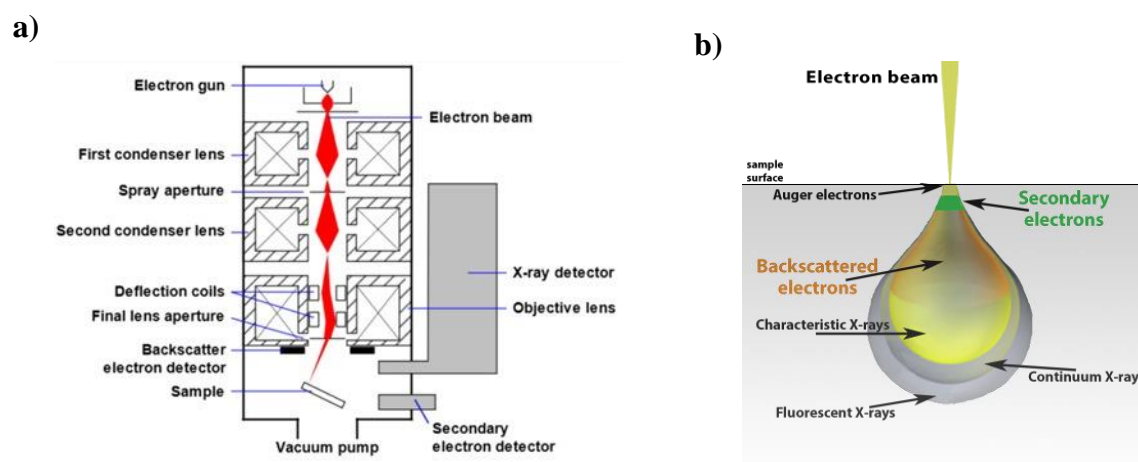

Figure 18: Schematics of **a)** a scanning electron microscope and **b)** electron-sample interaction.[86]

electrons can escape the sample. The amount of the electrons escaping from the sample at every scanned point can be measured and this forms the image. The electrons that scatter elastically and nearly trace back their movement path are called backscattered electrons (BSE). Inelastic scattering can also result in production of X-rays when the primary electrons in the beam interact with the tightly bound inner shell electrons of the sample. Another product of the collisions is secondary electrons (SE), which are formed when the primary electrons eject loosely bound electrons from the outer shells or the conduction band of a metal. These SE are the most commonly used form of scattering for SEM imaging.[66]

The most important characteristic of SE is their low kinetic energy. This allows them to only scatter from the surface within a depth of a few nanometers compared to the hundreds to thousands of nanometers of BSE. Because the SE move slowly, they need to be accelerated for collection. This is usually done by charging a detector positively, so that the electrons are accelerated towards it. Even though the required voltage to accelerate the electrons can be quite high (around +10 keV), the magnitude of this interaction is low enough so that the BSE will not be affected by it. This is because of their greater kinetic energy in comparison to the SE. Therefore, only the slower SE are collected and, in the final image, because SE scatter to all directions, no shadows will be formed.[66]

Because SEM uses electrons to excite samples, insulating samples will start to accumulate a negative charge on their surface. Therefore, they usually have to be coated with a conductive material that will be grounded. This way a path for discharging the sample is possible. However, charging phenomena can happen in any sample no matter how conductive it is. Especially if the surface is uneven with small depositions or similar shapes on top of it. Then, if charging happens, some artifacts can be seen on the images. For example, these artifacts can be extremely bright areas or dark halos. If coating is not a possibility, the imaging method can be altered. One of the possible alterations is increasing the scan rate of the electron beam. This reduces the dwell time of the electron beam on a single spot, so that less electrons can hit the surface adding to the accumulated charge. Unfortunately, a faster scan rate results in a worse signal to noise ratio (SNR) when imaging. To combat this change, several scans of the whole area can be done with a fast scan rate and the consecutive images can then be summed to have an image with a better SNR. Additionally, some imaging software are equipped with smart drift correction modes that recognize patterns from the image and sum the images so that if some image shifting were to happen, it will be compensated.[66]

Pure one-layer graphene is a conductor so no charging effects should be seen, but as more defects are added, the conductivity of graphene typically decreases. This is especially true with graphene oxide. Therefore, when characterizing graphene-based materials, a clear indication of the properties of the sample can be the amount of charging seen on the sample when imaging.

9.3 XPS

X-ray photoelectron spectroscopy (XPS) is a popular surface analysis method that utilizes X-rays. The popularity of XPS can be explained with its ability to identify and quantify all elements present in a solid sample's surface within the first 10 nm. It is also able to reveal the chemical environment where the detected element exists meaning the different bonds the element has formed in the material under inspection. In addition, this information is available quite easily and with relatively small amount of sample preparation.

In an XPS measurement, a sample is placed in a vacuum where it is excited with monochromatic X-rays so that it emits photoelectrons. Photoelectrons are electrons that have absorbed enough energy from a photon to be emitted from an atom. These electrons are collected and directed with an electron lens to a detector. Based on the number of electrons emitted at a certain binding energy (E_B), comprehensive information about the sample can be gained. The most commonly used part of the information is identification of all elements (except for H and He) and determining the surface composition and the molecular environment. However, with more sophisticated analysis methods even more information can be gained. A schematic of a modern XPS device with its main components named and an example survey spectrum of a hard-segment polyurethane (the molecule in the inset) showing the typical elements found also in different graphene-based materials are presented in Figure 19.[67]

The photon-electron interaction that happens when the photoelectrons are emitted is known as the photoelectric effect. In it, the photon transfers all of its energy to the electron. The emitted photoelectron has a kinetic energy specific to the environment and element it was emitted from. When the detector of an XPS device is used to measure the kinetic energy E_K and the excitation energy of the X-rays hv is known, the binding energy of an electron E_B is calculated with
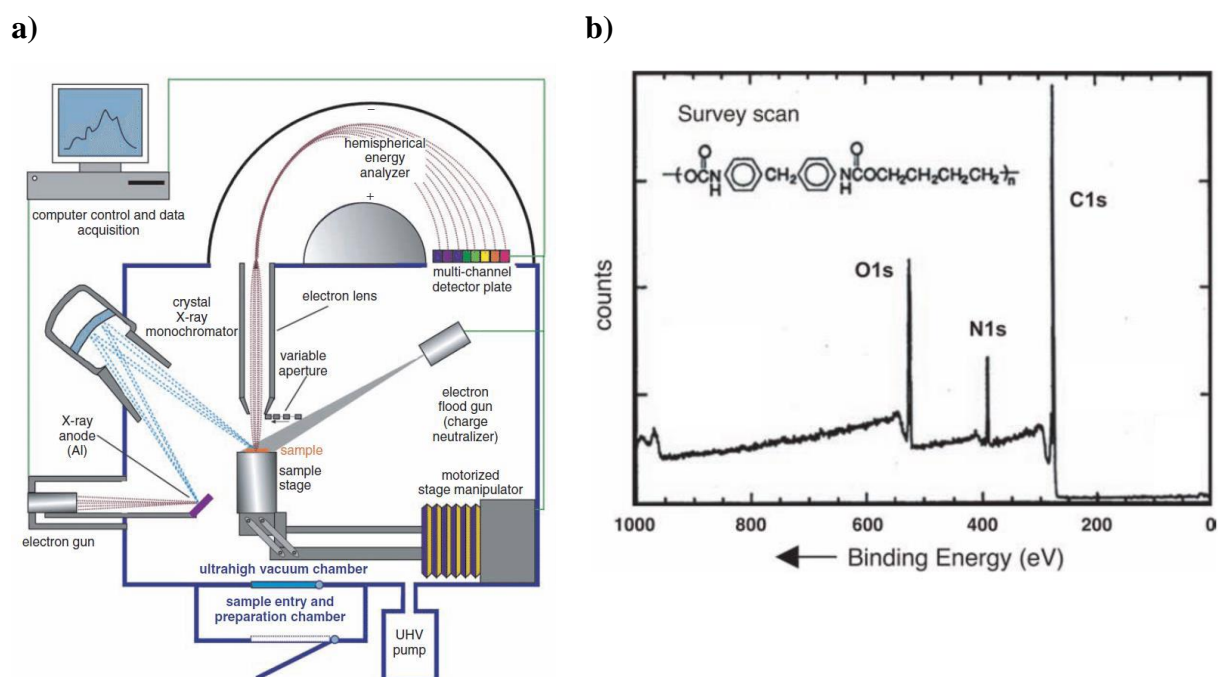
$$E_B = hv - E_K. \tag{41}$$

Figure 19: a) A schematic of an XPS device and **b)** a survey scan spectrum of hard-segment polyurethane film with an arrow beneath it showing in which direction the E_B increases in a typical plot.[67]

Typically, the E_B is presented in electron volts (eV). 1 eV corresponds to $1.6 \cdot 10^{-19}$ Joules.[67] Every element has different electronic states that can be excited by X-rays. For example, silicon has two transitions, Si2s and Si2p, that have intensities useful for quantifying the amount of Si in a sample. However, in this work, the transitions that are going to be used are the C1s for carbon and O1s for oxygen. The names of these transitions refer to the electron shell where the electrons are emitted from.[68]

The binding energy related to a transition for an element is dependent on the energy of the initial (E_i) and final (E_f) states of the material as follows:

$$E_B = E_f - E_i. \tag{42}$$

In an ideal situation, where the material is just an element and all electrons are assumed to be "frozen" in their place, the binding energy would be approximately the negative orbital energy ($-\varepsilon_k$). This approximation is called Koopman's theorem:

$$E_B \approx -\varepsilon_k. \tag{43}$$

However, in reality the electrons do not stay still and therefore this approximation is not valid. Instead, the remaining electrons rearrange to shield or minimize the energy of the ionized atom. This decrease in energy is called the relaxation energy and it is a final state effect.[67]

Following Equation (42), the initial and final states affect the binding energy. The initial state refers to the chemical environment in which the material is. This means that when, for example, the element at hand forms chemical bonds, the binding energy changes. This is called the chemical shift (ΔE_B). A typical assumption is that the chemical shift is only affected by the initial state effects. This would mean that the binding energy would increase when the oxidation level of the element increases, resulting in

$$\Delta E_B = -\Delta\varepsilon_k, \tag{44}$$

where $-\Delta\varepsilon_k$ is the change in initial state effects. This is usually adequate for most samples and gives each chemical bond or functional group of the material a corresponding shift in binding energy. Some relevant binding energy values using this method for C1s have been listed in Table 1 and for O1s in Table 2. The precise binding energy observed depends on the chemical environment and the typical variation of the range is $\pm$ 0.2 eV.[67] For a more comprehensive

Table 1: Binding energies for chemical bonds relevant in graphene's C1s peak[69]

Bond type	Binding energy (eV)
C-C (sp^2)	~284
C-C (sp^3)	284.8
C-O	~286
C=O	~289

Table 2: Binding energies for chemical bonds relevant in graphene's O1s peak[69]

Bond type	Binding energy (eV)
C=O	531.5–532
C-O	~533

listings for different elements the reader is guided to online resources[69] or to the book by Beamson and Briggs[70].

With this information, the peaks can be resolved into their corresponding subpeaks by peak fitting, which is effectively functional group fitting. For this, parameters such as background, line shape (Gaussian, Lorentzian, asymmetric or some mixtures) and peak position, height and width can be used. Most commonly used and simple background model is the Shirley inelastic scattering background[71]. After this, initial guesses are made either by previous experiments, prior knowledge of the sample or manual graphical fitting. Using a fitting algorithm, the final values are obtained.[67]

When determining the atomic concentrations and ratios of different elements from the resolved XPS spectra, relative sensitivity factors (RSF) have to be used. These factors are theoretically calculated values that assume the material as homogenous and depend on the material's properties, such as the photoelectric cross-section for the atomic orbital, efficiency of the photoelectron formation process and the mean path of photoelectrons in the sample.[72] The RSF are used to scale the measured raw peak so that it represents the quantity of its corresponding element in the sample. Most common reason for incorrect quantification is the usage of incorrect RSF.[68] The concentration X_i for an element i is calculated by

$$X_i = 100 \frac{A_i}{\sum_{i=1}^{m} A_i},$$

(45)

where the normalized intensity A_i is determined by

$$A_i = \frac{P_i}{T(E)\, R_i}.$$

(46)

Here P_i is the raw area or intensity of a peak, $T(E)$ is a transmission correction accommodating instrumental variations and R_i is the RSF of the corresponding element from an RSF database. The RSFs used in this work with the $T(E)$ incorporated in them for quantifying the amount of carbon and oxygen are 1.0 for C1s and 2.93 for O1s transitions.[68]

Another aspect of XPS that has to be taken into account when analyzing data, is charging of the surface. This is a phenomenon that happens especially with insulating samples, such as

graphene oxide. When the positive charge formed on the surface due to the emission of electrons cannot be neutralized with movement of electrons within the sample, the binding energy of the remaining electrodes is affected. Therefore, charging can be seen in the spectra as a peak shift in binding energy. This can also alter the shape of the peaks, which will make accurate functional group fitting impossible. However, this effect can be prevented with charge compensation during the measurement. Charge compensation can be executed with flooding the sample with monoenergetic, low energy electrons. In addition, when analyzing the data, one characteristic peak, such as C1s, can be detected from the spectrum and the all the measured intensities shifted to correspond actual values.[67]

10 Electrochemical Methods

This section describes the used electrochemical methods in a practical manner. Measurement parameters, setups and data processing are discussed. For a more theoretical approach, see the section 4 of the literature review part of this thesis.

10.1 CV

In this work cyclic voltammetry (CV) is used to inspect the capacitive and electrochemical properties of the electrode material. On the contrary to the typical theoretical cyclic voltammograms that can be seen in literature[42], the measurements here are not begun from a set high potential, scanned to a low switching potential and then again to the initial potential. Instead, all the measurements are begun at OCP, scanned to low potential, from there to high potential and this cycle is repeated several times. Depending on what is wanted to demonstrate, the voltammograms are either shown as measured, or the current is normalized with the surface area of the electrode representing the current density.

A cyclic voltammogram has two main parameters to consider. The first one is the used potential window, which is defined by two vertex potentials (E_1 and E_2). The size of this window has limitations based on the electroactive window defined by the used electrolyte, electrode and solvent. An illustration of these different limitations is presented in Figure 20a). The second parameter is the scan rate. The scan rate controls the speed of the change of the applied potential. This affects also the measured current, because a faster change in potential results in a faster change in current.[42] The effect of scan rate is visible in Figure 20b). In addition to these

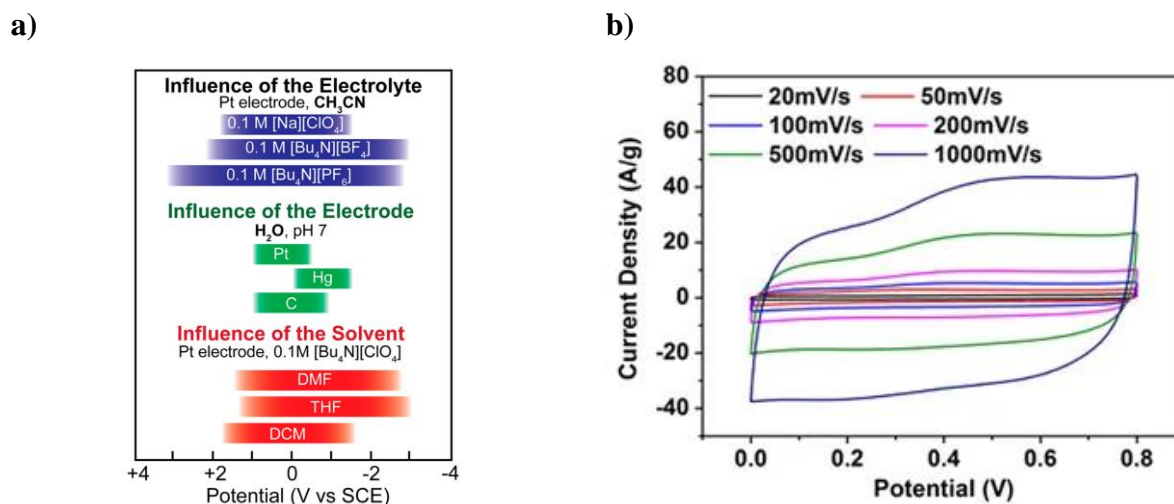a)   b)

Figure 20: a) The effect of electrolyte, electrode and solvent on the limitations of the potential window used in CV. Reproduced with permission from reference[42], © 2017 ACS, DOI **b)** Cyclic voltammograms of photoreduced graphene oxide with different scan rates. The current is normalized with the mass of the electrode.[73]

two parameters, depending on the measurement software, other parameters related to sensitivity can be required. For example, current and potential ranges or step size.

The possible measurement setups used for CV are a 2-electrode setup and a three-electrode setup. In both of these the working electrode (WE) is the electrode of interest, at which the reactions being studied happen. In the 2-electrode setup, the second electrode is the reference electrode (RE). RE has a well-defined and stable equilibrium potential. It is a reference point against which the potential of the WE can be measured. Commonly used REs in water solutions are saturated calomel electrode, saturated hydrogen electrode and the Ag/AgCl electrode. They are typically separated from the electrolyte solution by a porous glass plug.[42]

In the three-electrode setup a third electrode, the counter electrode (CE) is added to contact with the electrolyte solution. It is necessary to have a CE when the potentials applied to the system are great enough to allow significant oxidation or reduction of the analyte in the solution to happen. When this happens, a current will start to flow, which would disturb the equilibrium within the RE. Therefore, the CE will complete the electric circuit by allowing the current to go through it. CE should be as inert as possible to prevent any reactions happening at its surface from inhibiting the reactions of the WE. Also, to ensure current flow the area of the CE should be bigger than that of the WE. The CE is typically a platinum wire or disc, but some carbon-based options are also available.[42]

The shape of the voltammogram gives information about the properties of the material. A typical shape seen with graphene-based materials is a faradaic peak-incorporated rectangular shape as presented in Figure 20b). This box shape indicates that the electrode has an ability to transfer charge fast in a double-layer capacitance. The broadened peak shape at $0.2 - 0.6$ V also indicates the presence of pseudocapacitive phenomena.[73] In short, pseudocapacitance is a capacitance that can be associated to cations depositing to a negatively charged electrode, redox processes in the electrolyte or chemisorption of anions onto an electrode's surface. It is common that double-layer capacitive and pseudocapacitive processes are coupled, forming the total capacitance of the electrode-electrolyte interface.[74]

Determining the capacitance of an electrode from a cyclic voltammogram can be done by approximating it as ideal. For ideal capacitors the capacitance C in farads is

$$C = \frac{Q}{V}, \tag{47}$$

where Q is charge of the capacitor in Coulombs and V is potential over the device in volts. In cyclic voltammetry measurements, a current is formed according to

$$I = \frac{dQ}{dt} = C\frac{dV}{dt}, \tag{48}$$

where $\frac{dQ}{dt}$ is the accumulating charge over time and $\frac{dV}{dt}$ is the scan rate used to change the potential in volts per second. Using this equation and taking the average of the anodic and cathodic currents at 0 V for an electrode, an approximated capacitance can be calculated. A more precise value for capacitance can be determined by integrating the area within the voltammogram. A possible integration method is described in the section 11.4.

10.2 EIS

Electrochemical impedance spectroscopy (EIS) was used to study the electrodes' electric properties and the interface between the electrode and the electrolyte. The used method was Potentio-EIS (PEIS), which uses potential control to perturb the system. Other option would be Galvano-EIS (GEIS), which uses current control. In an EIS measurement the studied system is

stimulated with an AC electrical current or voltage within a selected frequency range and the response (the voltage or current) is recorded. A variation of the PEIS measurement is to alter the average potential of the applied AC potential so that effectively a DC voltage bias is applied onto the sample. This can give additional information about the different components of the inspected system. Because the response is normally assumed as time-invariant in EIS, the system measured has to be in a stable state. This can be achieved with a pretreatment protocol. (See section 11.3) The information gained from EIS measurements is usually either about the properties of the electrolyte or from the electrode-electrolyte interface. For the former, the parameters definable can be such as conductivity, dielectric constant or charge mobilities. For the latter, e.g. capacitance of the interface or diffusion rates of neutral particles onto the electrode can be defined.[75]

Electrochemical impedance measurements are automated by using a commercial potentiostat when inspecting the electrode-electrolyte interface. The computer operated potentiostat is combined with a frequency response analyzer (FRA), which is connected to the inspected system through the potentiostat. Because of the connection through the potentiostat, the bandwidth chosen for a measurement is very important if accurate high frequency measurements are to be made. A potentiostat consists of a power amplifier, a control loop to maintain voltage or current over the measured system (depending on if PEIS or GEIS is used), connections to the electrodes (WE, CE, RE) of the system and connections to the FRA. One of the most important aspects of a good potentiostat is the ability to maintain DC conditions on the measured system. This is important because a vital part of typical impedance measurements is staying in a linear area of current versus voltage response of the system as seen in Figure 21a). Here both, the AC current and voltage have symmetric sinusoidal nature. If the amplitude of the perturbation used is larger than the linear response area or the DC conditions shift from said area, significant inaccuracy can be present in the final data. This effect is demonstrated in Figure 21b), where an asymmetric current response can be seen due to the used amplitude of the voltage perturbation being too high.[75] However, pseudolinearity can be achieved with using a small amplitude.

The standard and most precise method of measuring impedance is applying a low amplitude single-frequency stimulus to a system over a range of frequencies. Then the resulting AC voltage over the system and AC current passing through the cell at the used frequency are measured. These two parameters are used by the FRA to calculate the impedance. In addition
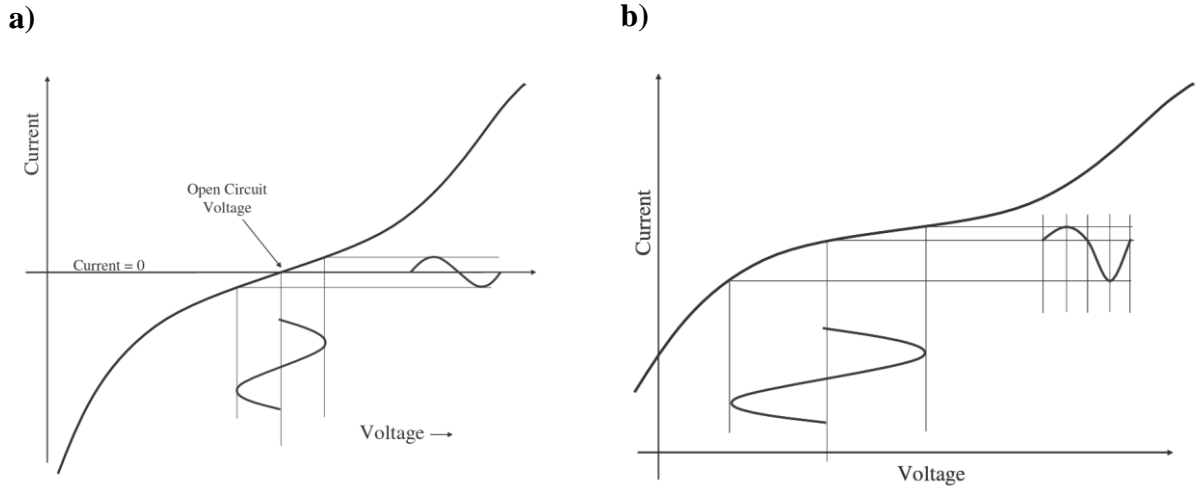
a)

b)

Figure 21: Illustrations of how the shape of the current response of an impedance measurement changes when the DC conditions are within **a)** linear and **b)** non-linear regions of the current-voltage curve.[75]

to this single-frequency method, a fast Fourier transform method with multiple frequency stimulus can also be used, but it will not be discussed here.[75]

The property of a material, impedance (Z) is, in short, the complex resistance of a system under an AC perturbation at one frequency. The monochromatic AC voltage perturbation as a function of time (t) is presented as $v(t) = V_m \sin(\omega t)$. The response is a current as a function of time $i(t) = I_m \sin(\omega t + \theta)$. Here the subscript m refers to the monochromatic nature, ω is the used frequency and θ is the phase difference (i.e. phase angle) between the voltage and current. From here differential presentations for both current and potential can be given, but the mathematical treatment can be simplified by doing a Fourier transform to give an impedance function $(Z(i\omega))$ comparable to Ohm's law. The impedance function is defined as a combination of the Fourier transformed current $(I_{FT}(i\omega))$ and voltage $(V_{FT}(i\omega))$, which are all complex functions of the frequency ω

$$Z(i\omega) = \frac{V_{FT}(i\omega)}{I_{FT}(i\omega)}, \tag{49}$$

where i is the imaginary unit $(i = \sqrt{-1})$. In relation to the impedance function, impedance is the function's value at one frequency. When the excitation is a monochromatic single sine wave, the Fourier transformed voltage and current become $V_m \pi$ and $I_m \pi \exp(i\theta)$ respectively.

For purely resistive behavior $\theta = 0°$ and for purely capacitive behavior $\theta = 90°$. To simplify the presentation of the impedance function it is often written as $Z(\omega)$.[75]

Impedance is typically represented in two different ways. The first one is the Nyquist plot, in which the negative imaginary part $-\text{Im}(Z(\omega))$ is plotted against the real $\text{Re}(Z(\omega))$ part. This is called the complex plane and also known as the Argand diagram. The second one is called the Bode plot, which can be calculated directly from the Nyquist plot. In the Bode plot logarithm of impedance and phase angle are plotted against a logarithm of the frequency of the perturbation. To gain these values, the required calculations are

$$|Z| = \sqrt{\left(\text{Re}(Z(\omega))\right)^2 + \left(\text{Im}(Z(\omega))\right)^2} \tag{50}$$

for impedance and

$$\theta = \tan^{-1}\left(\frac{\text{Im}(Z(\omega))}{\text{Re}(Z(\omega))}\right) \tag{51}$$

for the phase angle. Example plots for simplified Randles equivalent circuit using both the Nyquist and Bode plots are presented in Figure 22. The advantages using the different variations to plot impedance are that they provide different descriptions of the system at hand. In the Bode
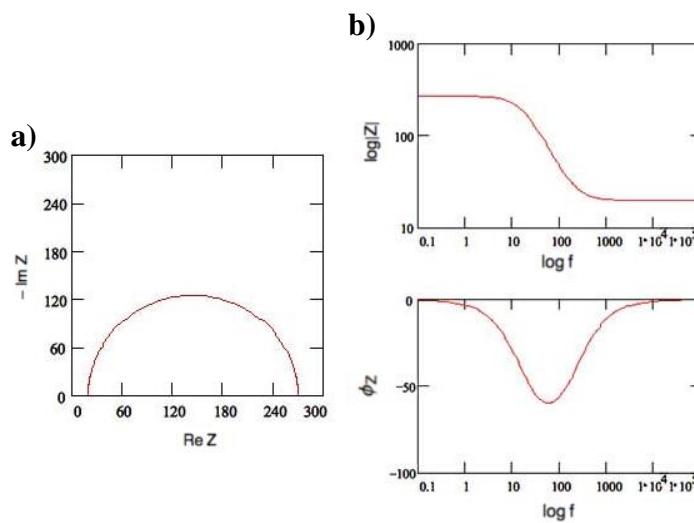

Figure 22: Example plots of the simplified Randles circuit presented in Figure 23 using **a)** Nyquist and **b)** Bode plots.[87]

plot the frequency dependence of the system is clearer than in Nyquist. However, Nyquist is often used to show the present diffusion processes, because they can be seen as additional half cycles (finite diffusion) or as a linear region with a slope of 1 (infinite diffusion). The diffusion happening at the surface of the electrode can be represented with the impedance of a Warburg element, which has been discussed in the literature review part of this thesis (section 5.4.2).[75,76]

To analyze this kind of plots, a common method of modeling electrochemical systems uses equivalent circuits. They are theoretical circuits that are formed using electric components with well-defined electrical properties. The purpose is to find circuits that would behave in the same manner as the electrochemical system that is being studied. This is a very useful method in EIS, because the behavior of this kind of circuits at different frequencies is well known. A common approximation of a non-ideally polarizable electrode is the Randles equivalent circuit presented in Figure 23. The plots shown in Figure 22 are calculated using the simplified version of this circuit. The different components of the circuit are R_{hf}, CPE_{dl}, R_{ct} and Z_D. R_{hf} is the high frequency resistance that can be associated to the bulk of the electrolyte, but it can also contain contribution from the electrode material. This resistance is seen in the Bode plot, within the high frequencies when the phase angle is $0°$ and impedance is constant. When the frequency is lowered, the phase angle begins to increase and the CPE_{dl} (constant phase element representing the double layer at the electrode's surface) will start to have enough time to charge up and become more and more insulating. A constant phase element is used to represent a non-ideal capacitor that has both capacitive and resistive properties. If the capacitance of the electrode would be ideal, the phase angle would go to $90°$. When the frequency slows down enough, the CPE_{dl} becomes an insulator and the current measured is due to leakage through the electrode's
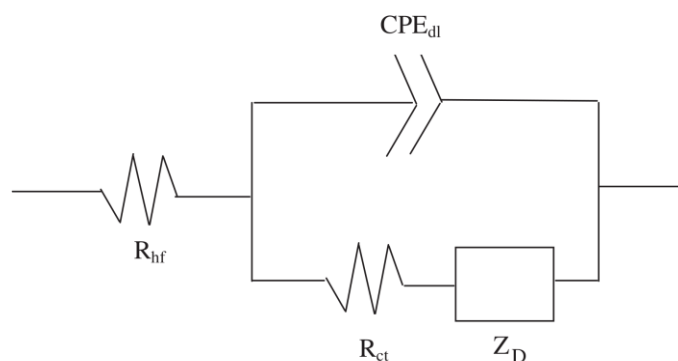

Figure 23: Randles circuit that represents a non-ideally polarizable electrode. The simplified version of the Randles circuit doesn't have the diffusion related Warburg impedance (Z_D).[75]

charge transfer resistance (R_{ct}) and the diffusion happening at the double layer (Z_D, often also W). For an explanation of the double layer, see section 4 of the literature review.[75]

Electrodes made out of single layer graphene have previously[77] been characterized using impedance measurements. These electrodes follow relatively well the behavior of the Randles circuit. In the low frequencies range impedance is dominated by the electrolyte's resistance and the charge transfer resistance of the electrode ($R_{hf} + R_{ct}$). When the geometry of the measurement setup is changed from that of the paper by Drieschner *et al.*[77] in a manner that all of the graphene has a contact with the gold, within the high frequencies the impedance is dominated by the contacts in the measurement setup (ideally zero) and R_{hf}. These two have no dependence over applied DC potential and therefore when impedance is plotted over potential, the behavior should be constant. If some change is detected in the impedance over potential, the change should be in the material's resistance. In mid frequencies the change in impedance is typically dominated by the capacitance that can be presented in an equivalent cell of the system (CPE_{dl}). This property gives graphene electrodes' impedance an upward opening parabolic behavior when plotted against DC bias voltage.

10.3 Chronometric Measurements

The chronometric measurement techniques used in this work are chronoamperometry (CA) and potentio electrochemical impedance spectroscopy wait (PEISW). The former method includes applying a stabilized potential over the measured system and measuring the current over time. Latter is essentially an PEIS measurement, but instead of using several frequencies to measure over a range, only one frequency is used. This allows monitoring the development of the impedance at one frequency over time.

11 Methods and Equipment

11.1 EGNITE

Engineered graphene for neural interfaces (EGNITE) is a novel graphene-based material created at ICN2 in collaboration with the Graphene flagship project. The material is highly porous giving it a large active surface area and capacitance. These properties allow it to have a high charge injection capacity and therefore it is ideal for neural stimulation and recording. The porous 3D structure of EGNITE is formed by stacking reduced graphene oxide (rGO) flakes.

These stacks are typically 1 - 2 µm thick with the sheet spacing being 4.8 Å.[78] EGNITE has already proven to be a promising material in these applications and several in vivo experiments have already been conducted.[79] These studies were on different microelectrode arrays and their acute implantations in rats. For example, a 64-electrode array on the cortex or a 9-electrode array in an intrafascicular multichannel electrode. Due to its stability and promising properties, EGNITE as a material was chosen for the biosensor measurements presented in this work.[78,79]

11.2 Material Characterization

The EGNITE for the electrodes was fabricated in house at ICN2. When received, the roughly 2 cm x 2 cm SiO_2 chips had first 10 nm of Ti and then 150 nm of Au deposited on them. A 7 mm x 7 mm square of roughly 1 µm thick EGNITE had been transferred on top of the gold layer.

The transferred EGNITE was fixed to the gold with low density fast curing MED2-4220 Silicone Elastomer (NuSil Technology), dried on a hot plate (95 °C, 10 min) and autoclaved (Autoclave Med20, Selecta) for three hours in 134 °C. One autoclaved sample and one untreated sample were chosen for Raman, scanning electron microscopy (SEM) and X-ray photoelectron spectroscopy (XPS) analyses. It was assumed, that all of the samples were identical in their chemical properties and that these two could represent the changes experienced by all of the samples.

Raman spectra were measured with Confocal Raman Microscope alpha300 R (Witec). The used grating was 600 g/mm, center wavelength 550 nm, laser wavelength 488 nm and intensity 500 µW. Every spectrum was integrated over 10 s and had 2 accumulations to prevent cosmic spikes from appearing. Nine points were measured within a 200 µm x 200 µm area to represent the samples, assuming that the samples were uniform. Analysis of the spectra was processed with the software Project FIVE 5.0 (Witec) and Origin Pro (OriginLab)[80].

Determining the surface areas of the electrodes was done with the Raman setup and its optical camera. Because the area of the electrodes was significantly greater what the setup was able to image in one photo, a stitching method was used. This method consisted of the imaging software taking several images of the whole electrode and then automatically combining them into one larger image. The final combined image was 600 x 600 px^2 representing an area of 9000 x 9000 $µm^2$. This gives for the size of one pixel 15 x 15 $µm^2$. From these images, using

the path tool of the open source GNU image manipulation software[81] the area of the electrode was identified and filled in with one color. The final area was measured using Fiji (ImageJ)[82].

SEM images were obtained using a Quanta 650FEG (Thermo Scientific) scanning electron microscope. Due to the non-conductive nature of the samples, a drift correction imaging mode was used. The XPS spectra were measured by the personnel of the ICN2 Photoemission Spectroscopy Facility with an XPS and UPS setup with PHOIBOS 150 hemispherical energy analyzer (SPECS). Analysis of the said data was performed on the software CasaXPS (Casa Software Ltd).

11.3 Electrochemical Measurements

For the electrochemical measurements a silicone pool was fixed on the chip around the EGNITE. At the same time the contact area of the EGNITE was reduced by passivating part of the sample under a microscope. Both the pool fixing and sample passivation were made with a structural adhesive Quick Set Epoxy 132-605 (RS Pro). An illustration of the used measurement setup is presented in Figure 24.

The reagents used when preparing solutions for the measurements were Phosphate buffered saline (PBS) tablets (Sigma-Aldrich), KCl (BioXtra, ≥99.0 % purity, Sigma-Aldrich), 1 M HCl (Fisher Scientific) and 1 M NaOH (Fisher Scientific). The electrodes used as counter and reference electrodes were a Pt wire and a flexible Ag/AgCl electrode (Flexref, 1.5 mm diameter, World Precision Instruments), respectively.

Initial measurements were made in a 10 mM PBS buffer solution and pH was adjusted by making additions of 10 mM HCl or 10 mM NaOH. The PBS buffer was created by dissolving one PBS tablet to 200 ml of deionized (DI) water. According to the information provided online by Sigma-Aldrich[83], this yields a 10 mM PBS, 2.7 mM KCl and 137 mM NaCl solution with the pH 7.4. 10 mM HCl and NaOH solutions were prepared by a single dilution of 1 M solution with DI water by a factor 1:100. In PEISW measurements, to ensure that the conductivity of the solution does not affect the measurement, a new set of solutions was created. A 10 mM PBS, 150 mM KCl solution was prepared by dissolving one PBS tablet and 2.2331 g of KCl into 200 ml of DI water. A HCl solution with a corresponding total ion concentration was prepared by dissolving 2.1609 g of KCl into 100 ml of 10 mM HCl solution. A 299.7 mM KCl solution was prepared for blank measurements. For PEIS measurements, to ensure that the only

change observed was the effect of change in pH, solutions with the same matrix and total ionic concentration as the 10 mM PBS solution were prepared: 10 mM HCl, 2.7 mM KCl and 137 mM NaCl and 10 mM NaOH, 2.7 mM KCl and 137 mM NaCl. For blank measurements a solution of 12.7 mM KCl and 137 mM NaCl was created. All the used variations of the solutions and in which measurements they were used are named and listed in Table 3.

In order to know the required volume to alter the pH of the buffer solution within a desired range, calibration measurements were made. This was conducted with a commercial pH meter (HI-3221 pH/mV/ISE/°C Bench Meter, Hanna Instruments). The calibrations were measured in 15 ml of PBS solution. Based on the calibration data, scaled down additions were calculated so that the increase of the HCl concentration was maintained in a smaller volume of 1 ml.

All electrochemical measurements were conducted with SP-200 Potentiostat (Bio-Logic) using the three-electrode setup illustrated in Figure 24. Before every measurement, a pretreatment protocol was run to make sure no species were adsorbed onto the electrode's surface and to stabilize the electrode. An increase of the open circuit potential (OCP) between the working and refence electrodes was typically observed. This protocol consisted of a PEIS measurement and seven sets of CV measurements followed by another PEIS measurement. Within the sets

Table 3: Used variations of solutions with the experiments that they were used in

Characterization	pH measurements				Solutions
All methods	CV	CA	PEIS	EIS*	
x	x	x	x		10 mM PBS, 2.7 mM KCl, 137 mM NaCl
	x	x			10 mM HCl
	x				10 mM NaOH
	x	x			10 mM KCl
				x	10 mM PBS, 152.7 mM KCl, 137 mM NaCl
				x	10 mM HCl, 289.7 mM KCl
				x	299.7 mM KCl
			x		10 mM HCl, 2.7 mM KCl, 137 mM NaCl
			x		10 mM NaOH, 2.7 mM KCl, 137 mM NaCl
			x		12.7 mM KCl, 137 mM NaCl

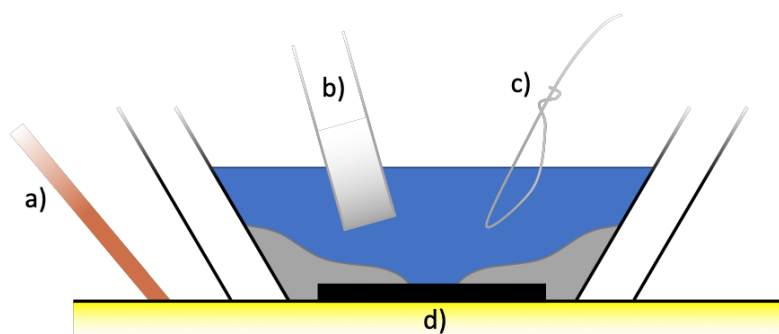*Chronometric EIS measurements (PEISW)

Figure 24: Illustration of the three-electrode measurement setup used in the electrochemical measurements: **a)** Cu wire used to make contact with the EGNITE working electrode through gold, **b)** Ag/AgCl reference electrode, **c)** Pt wire counter electrode and **d)** the partly passivated EGNITE working electrode. The passivating resin is shown in gray.

of CVs, first the potential window used was increased and when the maximum potential window had been reached, the scan rate was progressively decreased. All CVs were started from OCP and first scanned to the reduction direction (cathodic current, towards lower potentials). After the activation, a set of PEIS and CV were measured in order to follow the long-term stability of the sample. The precise parameters for both, the activation and the stability check, are presented in Appendix 2.

The rest of the CV measurements were conducted with similar parameters with varying scanning rates. Activation optimization measurements were measured with a scan rate of 50 mV/s with a potential window of 1.7 V (from – 0.9 V to 0.8 V). For the CVs for pH measurements a scan rate of 100 mV/s was used with the same potential window as before.

PEIS measurements were used to investigate the properties of EGNITE and its pH sensitivity. For the characterization, the mean voltage of the AC applied in the impedance measurements was altered. The first scan was measured at – 0.4 V and every consecutive scan had the potential increased with a step size of 0.05 V so that the last scan was at 0.4 V. In one scan, every measurement point was averaged from three measurements to reduce noise. Otherwise, the measurement parameters were the same as in the long-term stability PEIS measurements presented in Appendix 2. The pH measurements were conducted with the same settings, except that only a scan with the average potential applied at 0 V was used.

For chronometric impedance (PEISW) and amperometry (CA) measurements, a DC potential of -0.4 V was applied over the working and the reference electrodes. Both of the measurements

had the time resolution of one measurement point for each second, but for PEISW measurements three consecutive points were averaged to reduce noise.

11.4 Data Processing

To determine the capacitance of electrodes from a cyclic voltammogram, a program was written using Excel Visual Basic for Applications (VBA) programming language. The part of the program that integrates the area is presented in Appendix 3. This integration method uses linear interpolation between datapoints, which means that it assumes linear behavior between datapoints in the current vs potential curve of the CV. Thus, the total area can be formed by the sum of areas of right trapezoids. Area of a right trapezoid (A_{rt}) is the average of two values of consecutive currents (I) times the change in applied potential (ΔE):

$$A_{rt} = \frac{I_n + I_{n+1}}{2} \Delta E. \tag{52}$$

The anodic and cathodic charges (areas above and under the x-axis) are integrated separately and the sum of their absolute values is used to calculate charge storage capacitance (C_{CSC}) per area of the electrode. This is acquired by dividing the total area of the I-V curve with the scan rate used in the measurement and the area of the electrode. From the C_{CSC} the capacitance (C) can be calculated by dividing it by two (taking the average C_{CSC} of the anodic and cathodic C_{CSC}) and the potential window of the measurement (ΔV)

$$C = \frac{C_{CSC}}{2 \, \Delta V}. \tag{53}$$

12 Results and Discussion

First, this chapter presents the measured properties of EGNITE and the changes undergone during autoclaving. This is followed by the preparation for the electrochemical measurements and their optimization with the results of the electrochemical characterizations. Finally, the results for the attempted methods to measure pH using EGNITE electrodes are shown. All the samples are named using the format B#S#, B standing for batch and S for sample. For example, B1S2 is the second sample of the first batch. In addition, some samples had their surface area reduced and these changes are indicated after the sample's name in parentheses with the words

big (before reduction) or small (after reduction). A table of all the samples used in the data presented in this experimental section can be seen in Appendix 1 with their stitched images.

12.1 Characterization

12.1.1 Raman Spectroscopy

First the chemical properties of EGNITE were of interest. To inspect them, Raman spectra were measured from an untreated and an autoclaved sample to understand the chemical modifications experienced in the autoclave process. The Raman setup used allowed taking optical images of the sample areas showing the macroscopic surface texture. These areas are presented in Figure 25 for both of the two samples. The images show, that the macroscopic structure does change and some deformations happen. It is important to point out that these images are from two separate samples (B1S1 and B1S2) and not the same sample before and after autoclaving. Therefore, the chemical changes nor changes in the details seen on the material's surface cannot be observed for a unique sample. However, these two samples are from the same batch of EGNITE and it was assumed that the material would be identical in both of the samples. For that reason, the measurements are considered to be representative of the general changes undergone by the material. Because only two samples were used for characterization with Raman, SEM and XPS before and after autoclaving, it can be seen as a reasonable cause for inaccuracy in the results of these methods.
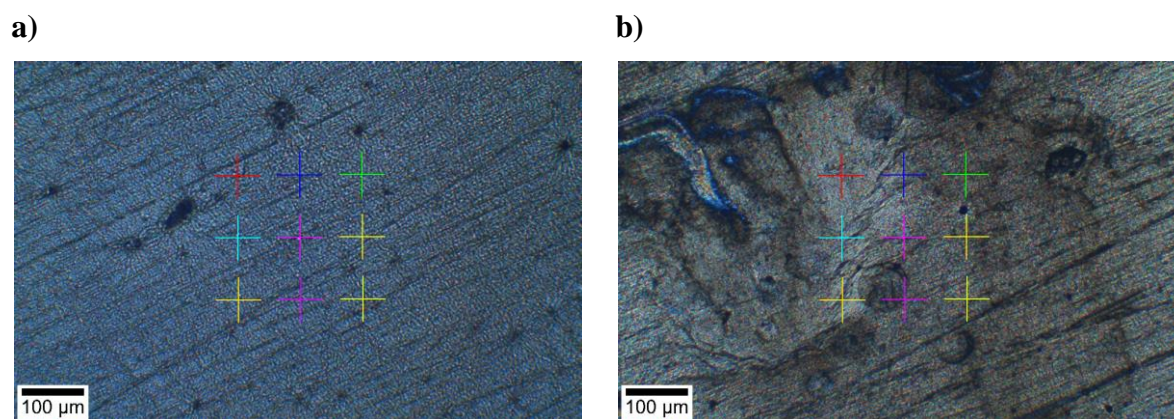
a)   b)

Figure 25: Optical images of **a)** untreated (B1S1) and **b)** autoclaved (B1S2) samples using the Raman microscope setup. Colored crosses mark used points to measure the Raman spectra. Brightness and contrast increased by 40 % and 20 % respectively.

All the measured Raman spectra were normalized so that the middle of the G-peak was set to 100 and the minimum of the spectrum was set to 0. After this, for one sample, all the spectra from different measurement points were averaged so that statistical differences between the two samples can be seen. In Figure 26 these averaged spectra are shown with the standard deviation of the peaks. The most notable change observed is in the intensity of the D peak in relation to the G peak. In addition, some intensity changes can be observed in 2D, D+G and 2D' peaks. The original spectra were fitted with Lorentzian shape peaks because of their clear symmetric nature and these results were used to calculate the parameters presented in the Table 4. These
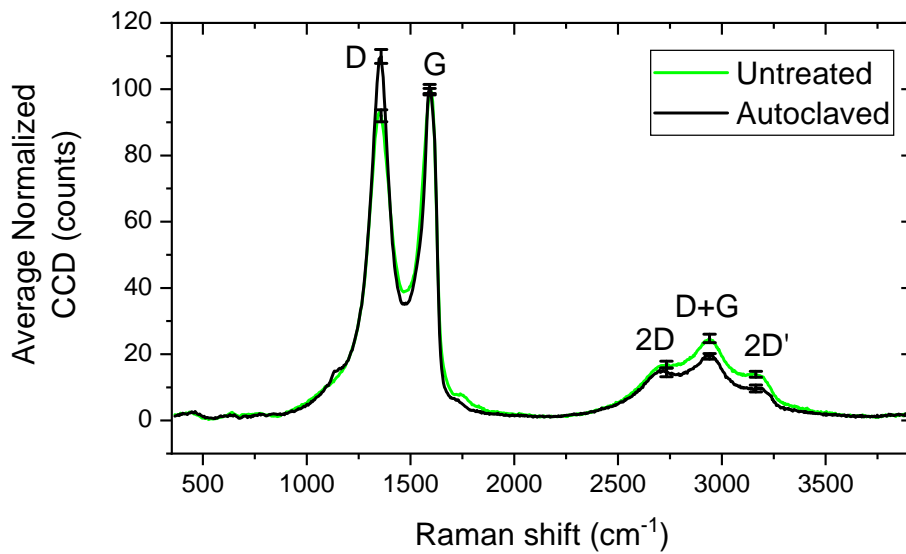
Figure 26: Averages of normalized Raman spectra for untreated and autoclaved samples with the observed peaks labeled. Error bars mark the standard deviation for each peak.

Table 4: Quality parameters calculated and obtained from the results of Raman spectra fittings

Param.	AVG untreated EGNITE	AVG autoclaved EGNITE	Difference	% change
$I(D)/I(G)$	0.929 ± 0.015	1.06 ± 0.02	0.136	+14.6 %
$I(2D)/I(G)$	0.126 ± 0.010	0.113 ± 0.011	-0.013	-10.3 %
$A(D)/A(G)$	1.79 ± 0.09	1.93 ± 0.04	0.14	+8.0 %
$A(2D)/A(G)$	0.39 ± 0.06	0.35 ± 0.08	-0.04	-10.1 %
$A(D+G)/A(D)$	0.36 ± 0.04	0.275 ± 0.008	-0.082	-22.8 %
$w(D)$ (cm^{-1})	150 ± 2	127 ± 3	-23	-15.5 %
$w(G)$ (cm^{-1})	78 ± 3	70.0 ± 0.9	-8.2	-10.5 %
$w(2D)$ (cm^{-1})	240 ± 30	220 ± 40	-26	-10.7 %

parameters are calculated from the intensity $I()$, integrated area $A()$ or FWHM $w()$ of their corresponding peaks D, G, 2D and D+G. Because the parameters are all normalized using another peak of the same spectra, they can be averaged and compared. The difference is calculated with the averages of both samples as change respect to the original, untreated state

$$Difference = AVG\left(\frac{A(D)}{A(G)}\right)_{Autoclaved} - AVG\left(\frac{A(D)}{A(G)}\right)_{Untreated}.$$

The percentual change, in turn, has been calculated by dividing the difference by the original value

$$\frac{Difference}{AVG\left(\frac{A(D)}{A(G)}\right)_{Untreated}} \cdot 100\%.$$

In their paper Eckmann *et al.*[61] show that the intensity ratio $I(D)/I(G)$ is below 1 in the stage 1 and an order of magnitude larger in the stage 2. As the ratio is around 1 in EGNITE before and after autoclaving, its defect concentration of seems to be in the stage 1 and slightly increase within the autoclaving process. To analyze the results presented in Table 4, the ratios between different peak's integrated areas can be used, following Figure 16. First of all, the ratio $A(D)/A(G)$ increases slightly. This could be interpreted so that the number of defects increases, if the material is at stage 1. The next parameter presented, $A(2D)/A(G)$ seems to stay virtually unchanged, since the detected change is within the statistical error. This is another indication that the material is in the stage 1 as within it the change undergone by $A(2D)$ is not significant.

Concerning the resistivity of EGNITE, $A(D + G)/A(D)$, as discussed by Ma *et al.*[62], can be used for analysis. A small decrease can be detected in this ratio, which would indicate that the resistance of the material decreases due to autoclaving. This is also supported by the increase in conductivity that can be seen in the SEM images of Figure 27 as a decrease in the amount of charge accumulation.

To see if EGNITE is reduced by autoclaving, the work of Díez-Betriu *et al.*[63] is used. According to their analysis presented in Figure 17, when $w(D)$ decreases, the sample is more reduced. The data presented here is in accordance with their results: A clear increase of $I(D)/I(G)$ and a decrease in the FWHM of G and D peaks are detected and $I(2D)/I(G)$ and $w(2D)$ do not

change. Therefore, it can be determined that autoclaving does indeed reduce EGNITE even though the defect concentration increases. This increase could be contributed to defect transformations, because when oxygen is removed from the sample, holes can form in the structure.[63]

12.1.2 SEM

To inspect closer the macroscopic structure of EGNITE, SEM images were taken. The acquired SEM images are presented in Figure 27. The untreated sample shows clear signs of charge accumulation: In the center of the image the darker area and the lighter area in the top of the image are most likely due to this effect. This would indicate that the untreated sample has low conductivity. Regarding the macroscopic structure of the sample, some wrinkles and minor depositions (white dots) can be seen on the surface. However, it seems that the sample is quite homogenous and, when compared to the autoclaved sample, smoother. The smoothness can also be a defect resulting from the drift correction imaging method averaging several images together. However, this should not be the case if the imaging method works as intended, but there is always a possibility for error. Keeping this in mind, the autoclaved sample has significantly more visible wrinkles in its surface. On top of that, more, larger and denser groups of unknown impurities can be detected on the surface. It could be possible that the deposition originates from the autoclaving process. More specifically, from the autoclave bags in which the electrodes are placed during the process. Other options could be longer exposure to room
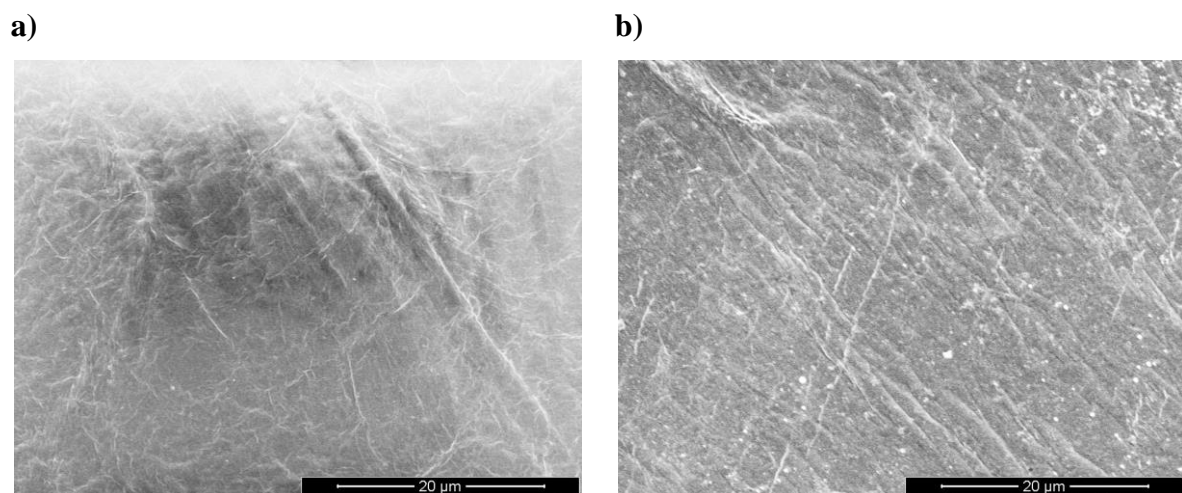
a)

b)

Figure 27: Acquired SEM images of **a)** untreated (B1S1) and **b)** autoclaved (B1S2) samples. A drift correction imaging mode was used to correct the effects from charge accumulation. Brightness and contrast have been increased.

air and therefore dust deposition from the air. However, the sample is clearly more conductive, since no signs of charge accumulation can be seen.

12.1.3 XPS

Quantification of the amount of carbon and oxygen in EGNITE before and after autoclaving was conducted with XPS. Figure 28 shows an overview of a larger measured binding energy range for untreated and autoclaved samples, Figure 29 depicts a more in detail shift corrected spectra from around the C1s and O1s peaks of graphene. All of these spectra have been normalized so that the highest intensity is set to 100 and the lowest to 0. For the high-resolution spectra in Figure 29 the normalization has been done so that the intensity ratio between the C1s and O1s has not changed for either of the samples. The two spectra of Figure 28 reveal that the intensity ratio between C1s and O1s changes significantly during the autoclaving process. By integrating the areas of these two peaks from both samples, a rough estimate for O/C (oxygen
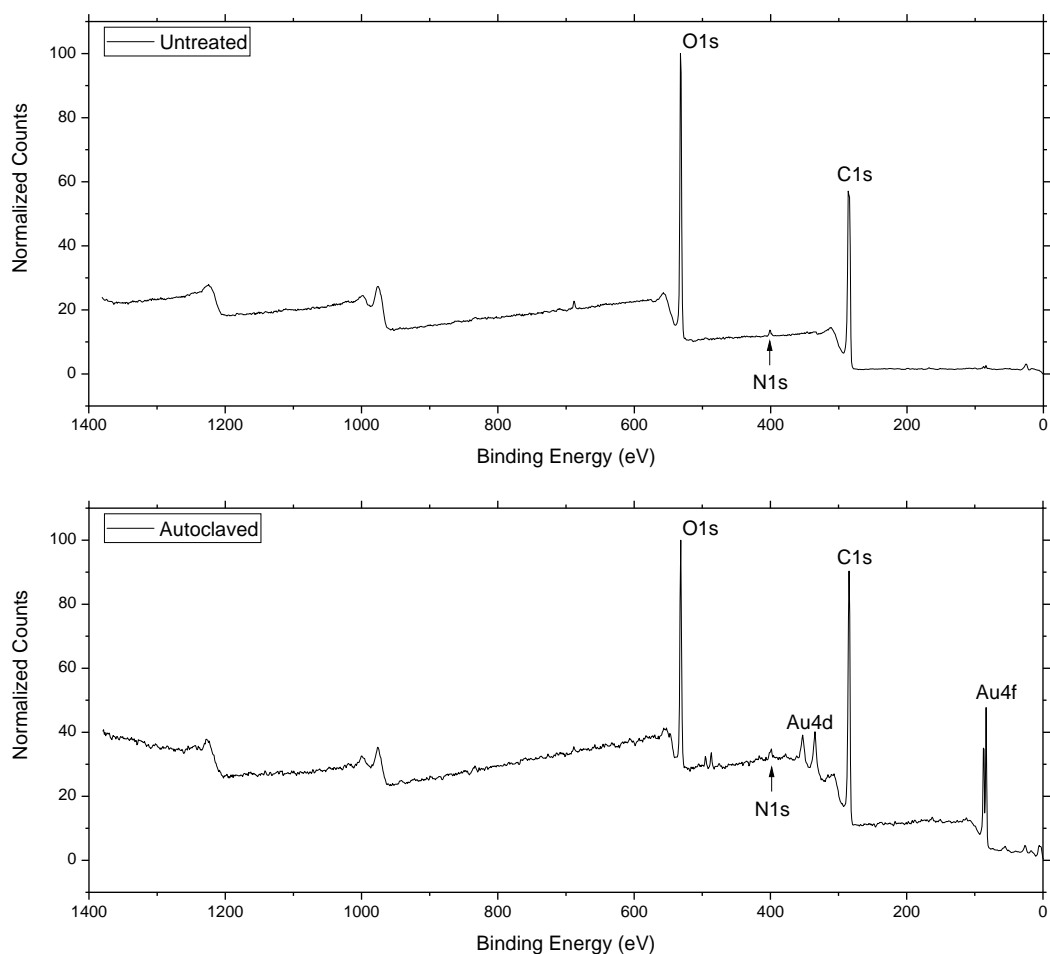
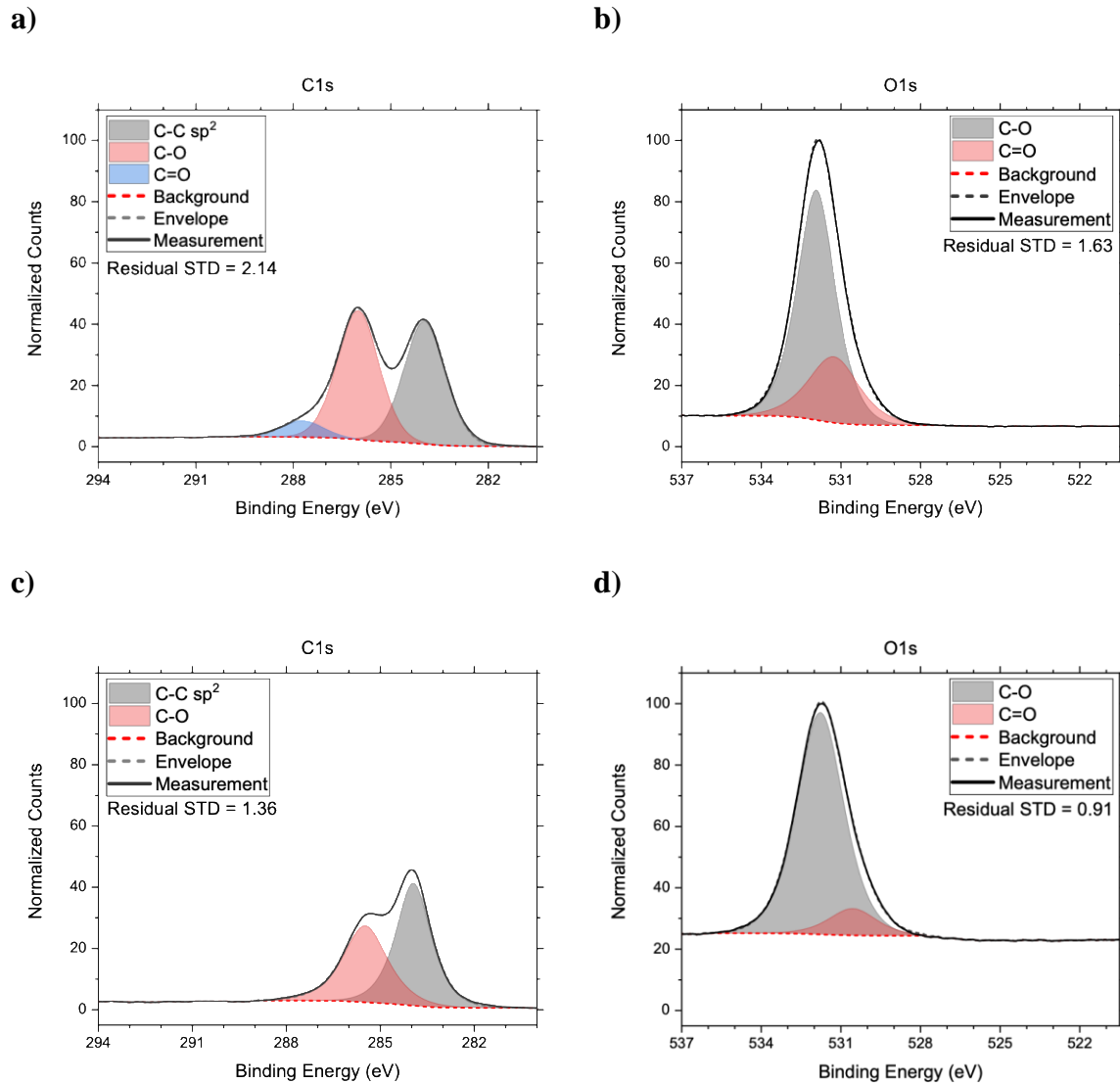**Figure 28:** Normalized overview XPS spectra of untreated and autoclaved samples.

Figure 29: Normalized XPS spectra for untreated (**a**) and **b**)) and autoclaved (**c**) and **d**)) samples measured separately with higher resolution from the C1s and O1s peak areas. Normalization has been made separately for both samples.

to carbon) ratio can be determined following Equation (45). For the untreated sample said ratio is 0.39 and for the autoclaved 0.27. This is only a rough estimation, because in the overview spectra, the step size is larger than in the corresponding high-resolution spectra. Therefore, it is possible that the true shape or the true maxima of the peaks is not detected.

The spectrum of the autoclaved sample reveals additional smaller peaks. They are from gold around the small area of EGNITE used to measure the spectrum. This is because of the spot size of the XPS measurement device being partially outside of the EGNITE and therefore the gold plating of the SiO_2 chip can be detected. Also, in both of the spectra, a small N1s peak can

be detected at around 400 eV. This is most likely contamination from the atmosphere, which is typically detected due to the imperfect vacuum within the XPS measurement chamber.

Inspection of the higher resolution spectra presented in Figure 29 gives a more precise O/C ratio, which is 0.50 and 0.31 for the untreated and autoclaved samples respectively. On this higher resolution spectra, a functional group fitting was done. The line shape was selected to be a mixture of Gaussian and Lorentzian shapes with a product formula provided by the used analysis software. The fitting shows the changes undergone by the samples in more detail. First of all, the shape of C1s peak lacks the tail around 288 eV. This change is tentatively attributed to the reduction in the amount of C=O groups during the autoclaving. The reduction is so significant that after the autoclave, the C=O functional group doesn't seem to contribute to the shape of the C1s peak at all. In addition, the ratio of C-O and C-C sp^2 is changed so that after autoclaving the signal of C-C sp^2 is more intense than that of C-O. The ratio C-O / C-C for the integrated areas of these peaks are 1.05 (before) and 0.79 (after). This ratio can be calculated with just the raw areas of the fitted peaks, because within one transition peak the RSF is same for all of the functional groups' signals.

In the O1s peak, due to the peak shape not being perfectly symmetrical and the C=O signal seen in Figure 29a), a C=O signal was fitted in addition to C-O. In the autoclaved sample, both of these two signals were used again to fit the peak, because this produced a smaller residual standard deviation. A significant change can be seen in the relative areas of these two signals during autoclaving. In relation to the intensity and area of C-O signal, the C=O signal decreases significantly. Before autoclaving the C=O/C-O ratio is 0.38, but after autoclaving this ratio drops to 0.12. However, since no C=O can be seen in Figure 29c), it could be possible that in reality no C=O groups are present in the autoclaved sample. In this situation, the double bonds are only contributing to the envelope shape due to the inaccuracy of the fitting in XPS data. Another important note on all the spectra of Figure 29 is that the intensities cannot be compared between different samples. Therefore, to see any change between different samples and sections, relative values have to be compared. However, because both of the high-resolution spectra for one sample have been measured during the same measurement, the intensities between different transition peaks are comparable. For example, the Figure 29a) and b) can be compared with each other.

12.1.4 CV

The electrochemical measurements require an electrode with a certain, known and stable state. Therefore, before doing any electrochemical measurements, the samples needed to be pretreated. To find out whether the samples were able to stabilize, a simple stability test was conducted with CV with a slow scan rate. Cyclic voltammograms of a sample were measured continuously until the CVs were overlapping. The corresponding data of said measurement is shown in Figure 30a). To actually see how the capacitance of the electrode developed during each cycle, it was determined for each cycle by integrating as described in section 11.4. The resulting capacitance as a function of cycle number is presented in Figure 30b). It can be seen that the capacitance reaches a certain value after a time and then stabilizes. In the inset of Figure 30b), an alternative parameter to indicate the reached stability is presented. This parameter is the current at the lowest potential applied (-0.9 V). As it can be seen, the shape of the behavior of both of these parameters is almost identical. Therefore, it can be said that both of them can be used for inspecting if a sample can reach a stable state. The advantages of having both of these parameters are that calculating the capacitance gives a more precise description of the stability, but the peak current is easier to extract from a set of CVs.
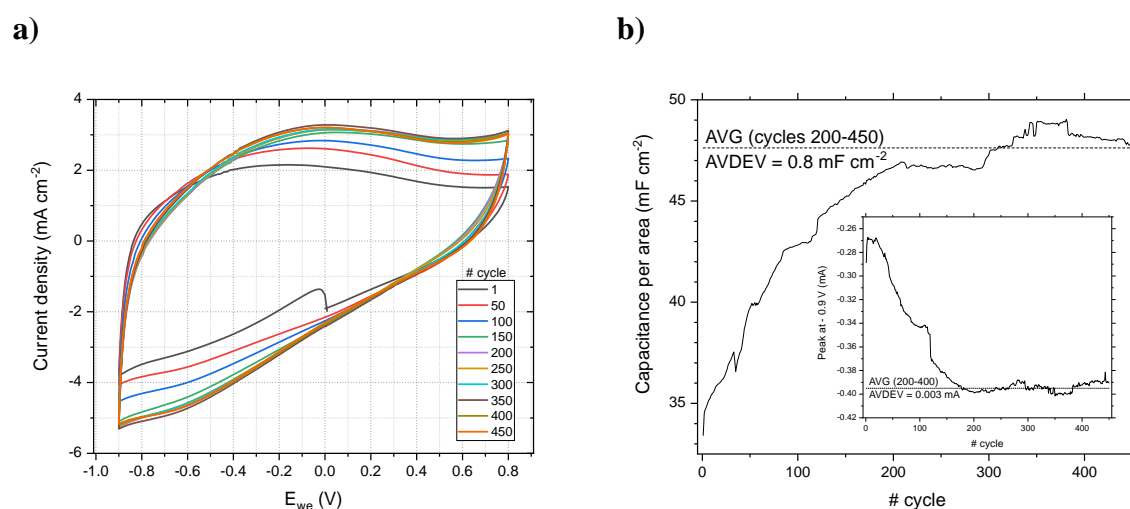
a)   **b)**

Figure 30: Activation optimization CV measurements of B2S1 normalized with the geometrical area of the electrode. The scan rate used is 50 mV/s. **a)** shows the measured CVs and **b)** the integrated area (capacitance) for each cycle. The capacitance can be seen to reach a plateau after a certain amount of cycles. The plateau (AVG) and its standard deviation (AVDEV) are presented. The inset shows the current at the lowest potential applied as an alternative parameter to indicate the reached limit.

After it was shown that the EGNITE electrodes used in these measurements could reach a limit capacitance, a pretreatment protocol was provided by the research group at ICN2. The original protocol was designed for microelectrodes with their diameter in the micrometer range. Therefore, the protocol was modified to correspond the larger macroelectrodes used here. Main alterations were changing the amount of CV cycles in a manner that kept the duration of the protocol reasonable. Typical CV scans of the activation protocol can be seen in Figure 31a). The capacitance of the electrode seemed to increase during this protocol, until it reached a certain value. After this, the potential window had to be increased to gain a larger capacitance.

The behavior of capacitance as a function of time with all of the three used potential windows at one scan rate have been presented in Figure 31b). As it can be seen, the capacitance increases fast in the beginning and then slowing down significantly. Every time when the potential window is increased, the initial increase in capacitance seems to be faster. However, with the larger potential windows, a saturation can be seen after which the capacitance seems to decrease. For the 1.4 V potential window this happens around 400 cycles and for the 1.7 V, already at 50 cycles. A possible cause could be that the activation protocol is too long, so that it already damages the material. Especially since the final capacitance with the largest potential window in Figure 31b) is lower than the initial capacitance.
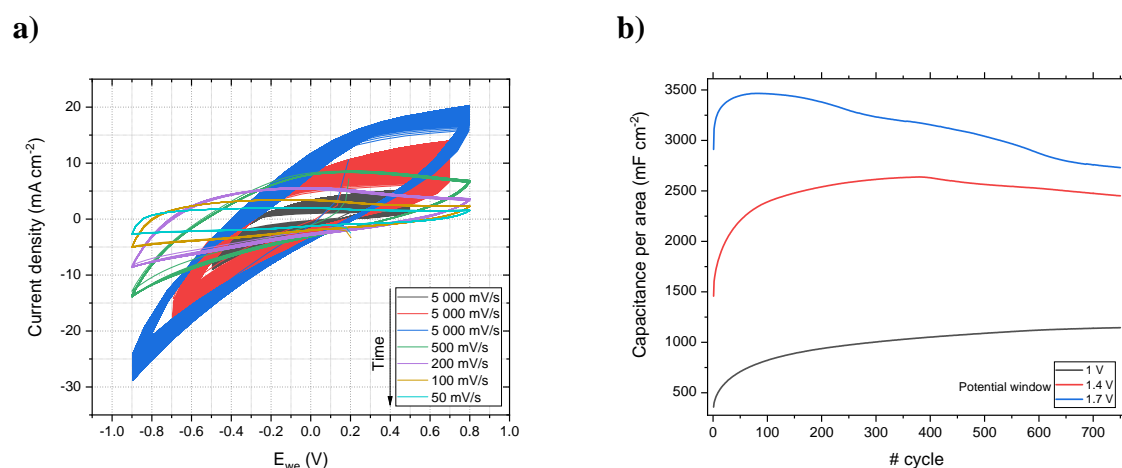
a)   **b)**

Figure 31: Typical activation procedure's voltammograms from B4S1, **a)** showing the measured voltammograms with different scan rates and **b)** the development of capacitance with different potential windows at 5 000 mV/s scan rate as a function of cycle number. The colors correspond to same cycles in both of the figures.

Due to the expected highly capacitive nature of EGNITE, comparisons between an ideal and the real electrodes were made. Figure 32 illustrates the behavior of an ideal capacitor, an ideal resistor and the data measured from EGNITE electrodes. The measurement used in the comparison is the last cycle from the data of Figure 30. As it can be seen, the capacitive region of the real electrode somewhat follows an ideal behavior in higher potentials when anodic current is measured. However, the behavior seems to have more of a resistive nature when cathodic current is measured. When looking at the shape of the voltammograms presented here, a typical box-like shape can be identified. As discussed before, this indicates a double layer capacitance present at the electrolyte-electrode interface. Also, in Figure 32 a broadened peak between -0.4 and 0.4 V can be seen indicating the presence of pseudocapacitance.

Further comparisons between ideal and real behavior were conducted by using long-term stability measurements made before every electrochemical measurement. From each day of measurements, the first long term stability test data was used to determine a sample's capacitance. In Figure 33a) the approximated ideal capacitance using Equation (48) is presented for one sample. In Figure 33b) the same data was used, but the actual area of the current-potential curve was used as described above. A relatively small difference between the ideal and real capacitances can be detected. For example, the final values presented in the figures are 52.2 mF / cm^2 and 41.9 mF / cm^2 for the approximation and real behavior respectively. Thus, the approximation gives roughly 25 % bigger estimates than what the reality is. According to
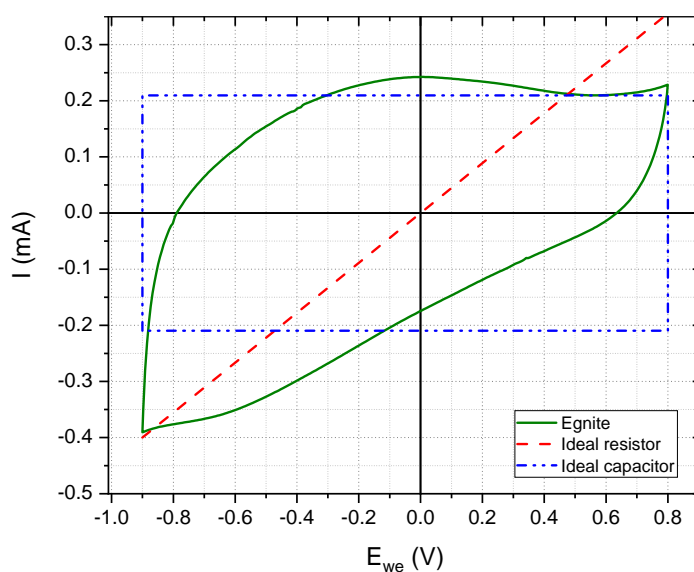

Figure 32: Cyclic voltammograms of EGNITE compared to an ideal resistor and capacitor's behaviors.
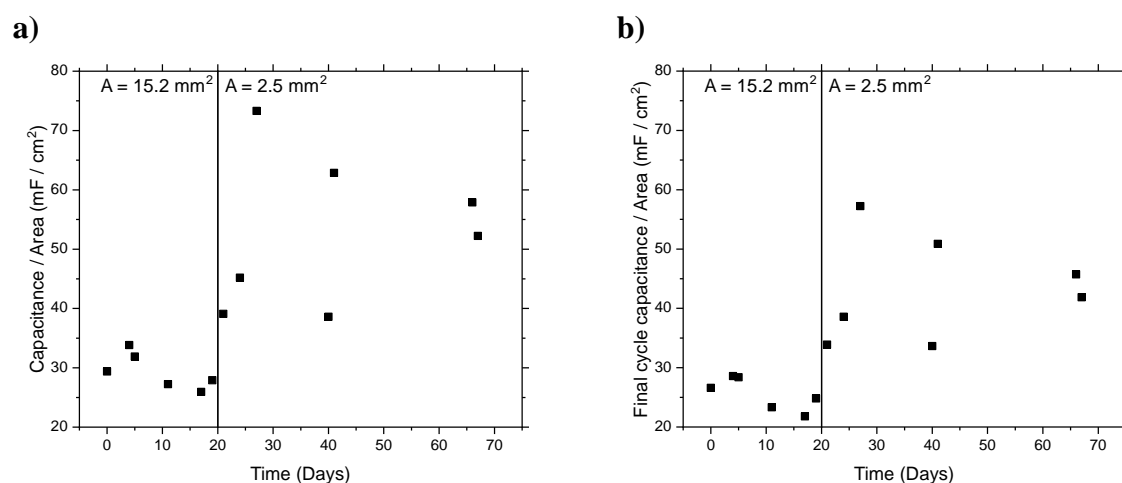
a)

b)

Figure 33: Long term stability of sample B3S3 with one measurement point presented per day of measurements. Capacitances in **a)** have been calculated by using the approximation presented in Equation (48) and in **b)** by integrating the whole area of the voltammogram as described in section 11.4. The geometrical area of the electrode was reduced at day 20 when the effect of this area was inspected in other electrochemical measurements. The scan rate used was 50 mV/s.

the review by Ke and Wang[15] these values are three orders of magnitude greater than the theoretical specific capacitance of 1LG (~21 µF cm^{-2}), and more than one order of magnitude larger than many other graphene-based material electrodes. However, some graphene-based nanocomposites and hydrogels have been shown to have higher capacities in supercapacitor devices.

Clear anomalies in the long-term stability of the electrode seem to be the increase in capacitance between the measurements of days 24 and 27 and 40 and 41. In both of the cases the capacitance seems to increase by over 60%. The CV measurement data for days 24 and 27 are presented in Figure 34. It can be clearly noticed that the behavior in the latter measurement is much more resistive than in the former measurement. It might be possible that an alteration in the measurement setup used, such as a bad contact between the gold and graphene, could have caused such an increase in the resistive nature of the electrode increasing the integral's area and therefore the determined capacitance. Another explanation for the increase between these said dates could be that during electrochemical measurements the EGNITE adsorbs the solution within the whole material, not only into the active part. This is supported by the fact that a
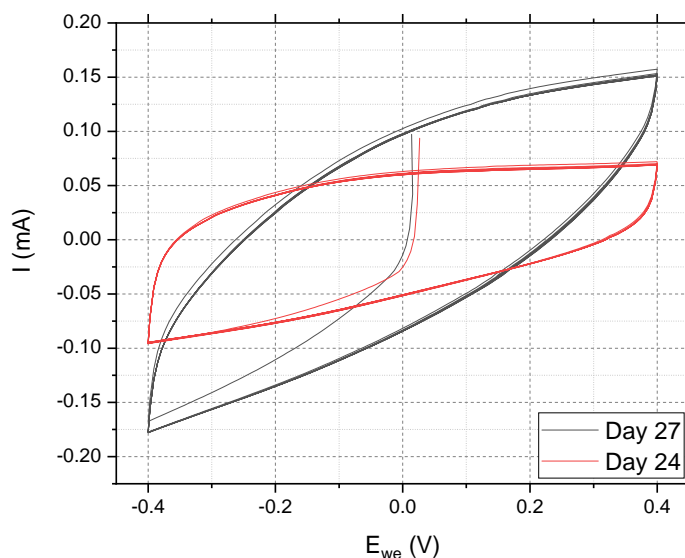
Figure 34: Two voltammograms from the long-term stability measurements presented in Figure 33. The used scan rate was 50 mV/s.

significant increase can be seen happening between two measurement days on two occasions when the time between is only a few days and the sample has not had time to dry.

No clear trends indicating the degeneration of the electrode material can be seen in the long-term stability data of Figure 33. In contrast, it would seem more like so that the material is becoming more capacitive as time goes on. Although, it is difficult to say in which direction the capacitance of the material is moving after the reduction of surface area, because the capacitance seems to fluctuate almost in a zigzag manner. However, the initial capacitance normalized with the area of the electrode seems to be lower than the final values. Even though one might then say that the capacitance increases, this does not give a certain result, because the normalization presented here does not take into account the active surface area of the electrode. Instead, only the geometrical surface area determined from the 2D images was used for the normalization. Therefore, the overall increase of the capacitance could be due to the solution being adsorbed into EGNITE. Then, when the surface area was reduced, i.e. the passivating layer on top of the electrode increased, the evaporation of the solution could have been slower. This would mean that the active area of the electrode remains similar even though if the geometrical area is decreased.

12.1.5 PEIS

To identify what type of equivalent circuit would represent the EGNITE electrode's behavior, PEIS measurements with an applied DC bias were conducted. The measurement data is presented for two different samples in Figure 35a) and b). Between the phase angle (top) and impedance (bottom) in the figures, a legend of the applied DC voltage is shown. The behavior as a function of potential applied for each of the three samples within three different frequency ranges is presented in Figure 35c) through e). The chosen frequencies to present low, mid and high ranges are 0.10 Hz, 1.52 Hz and 120 Hz, respectively.

In comparison to the response of graphene electrodes discussed in section 10.2, these EGNITE electrodes show a behavior that seems to have everything shifted towards lower frequencies. I.e. the resistive region for these samples, where the phase angle is near zero is at surprisingly low frequencies. In addition, the capacitive region seems to have shifted in the same manner so that even though relatively low frequencies have been used (down to 0.1 Hz), the behavior is still capacitive. This would indicate that EGNITE is more capacitive than graphene, because a lower frequency AC potential perturbation has to be used to see the effect of the charge transfer resistance of the material. This is supported by that, as discussed above, the determined capacitance of EGNITE is high.

A clear result from this data is that no DC bias dependence is detected in the high frequency range for any of the samples, as seen in the constant impedance of Figure 35e). This is to be expected since with the high frequency AC perturbation the electrode's hypothetical capacitive component does not have time to be completely charged. Therefore, only the resistance of the bulk of the solution limits the impedance. However, when the DC bias is applied, a change can be seen in the phase angle and impedance around the end of the resistive region: around 10 Hz for B2S1 and B3S1 (small). This DC bias dependence is most likely due to the double layer formed on top of the electrode being sensitive to the change. Given all the characterization data presented so far it is not likely that the change seen would be due to corrosion or drifting, because all the other experiments indicate the material being stable, although it can be a possible reason. Furthermore, according to Ambrosi *et al.*[18] graphene oxide is oxidized at potentials higher than +1 V and reduced at potentials lower than -1 V so no current due to redox reactions should be present. However, what is seen is that at higher potentials the impedance increases, which can be due to the diminishing of current flow. What can be said is that the main observation from Figure 35 is that the material seems to be stable in the applied potentials.
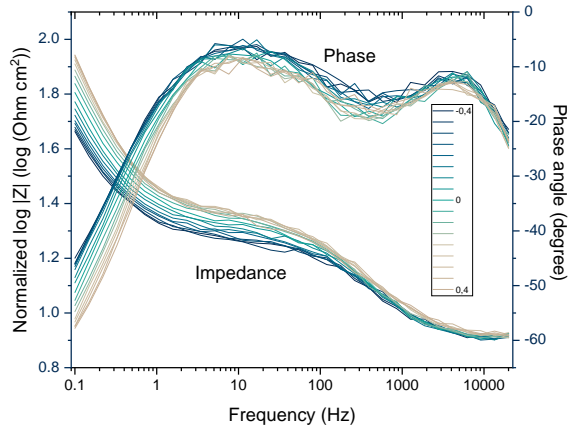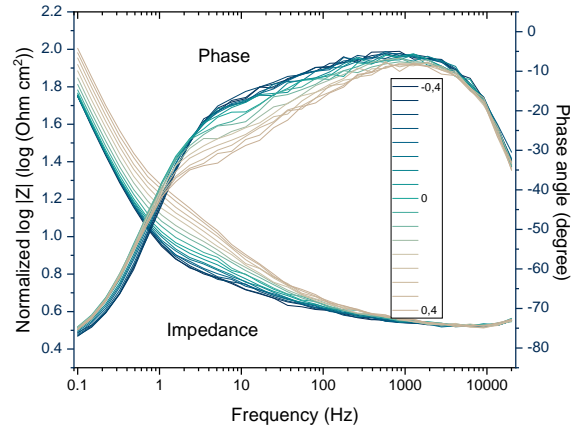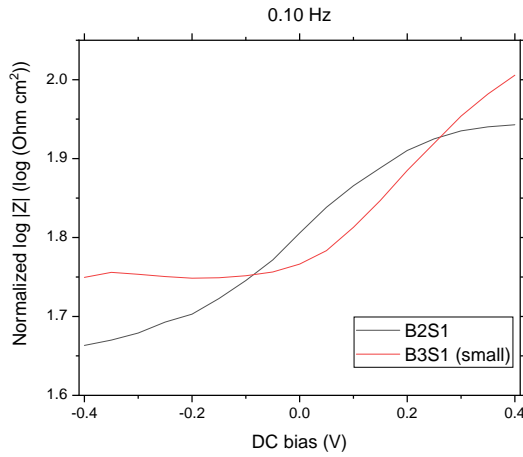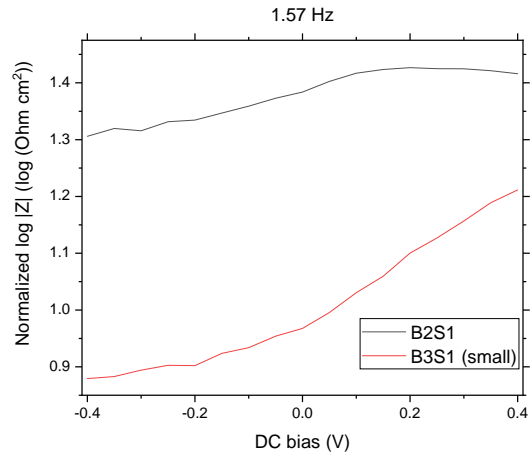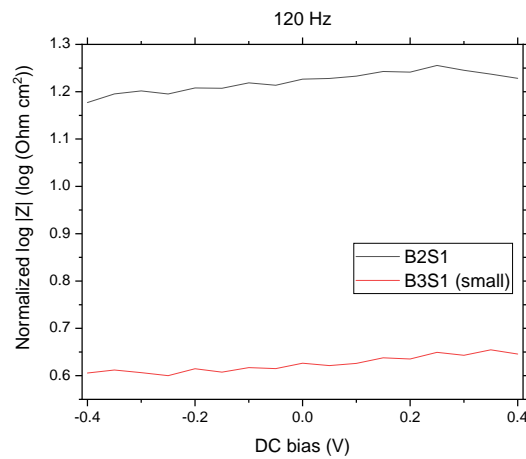
Figure 35: Applied DC potential dependence of **a)** B2S1 and **b)** B3S1 (small) and their behavior at three separate frequencies **c)** 0.10 Hz, **d)** 1.57 Hz and **e)** 120 Hz. Impedance |Z| has been normalized by multiplying it with the geometrical area of the electrode.

12.2 pH Measurements

Initial pH measurements were attempted with CV in a solution of PBS. First the pH was adjusted to 8.77 with NaOH from the initial 7.4 and then lowered with HCl while measuring a CV for each step. Figure 36a) shows how the shape of the voltammograms changed as the solution was made more acidic. From the anodic current part of this curve, a potential (-0.318 V) was arbitrarily selected to monitor the current change with pH. This change is shown in Figure 36b), where a somewhat linear regime can be detected within the pH window from 4 to 8. A fit was made in this linear regime, which is shown as a red line in the figure. From the slope of this fit, the sensitivity of this method was $(14.7 \pm 1.4)\ \mu A$ / pH.

Because of the low sensitivity of CV measurements, other amperometric methods were explored. A more suitable measurement method, CA, was tried out instead of CV. Data of the CA measurements are shown in Figure 37. For the duration of the measurement a voltage of -0.4 V was applied to the electrode. This was approximately the same voltage that had been arbitrarily selected from the CV measurements. The pH of the PBS solution was altered with a HCl solution and for the blank measurement, the corresponding additions were made with KCl. The chronoamperometry measurements seemed not to yield any kind of pH dependence and in these measurements the amplitude of the noise was typically around 3 μA. The only change seen in the CA data is that after every addition, a clear increase in current was detected. The decrease back to the saturation level was not found to follow any specific shape; the saturation levels after each addition did not seem to have any pH dependence. (Figure 37b)) The same
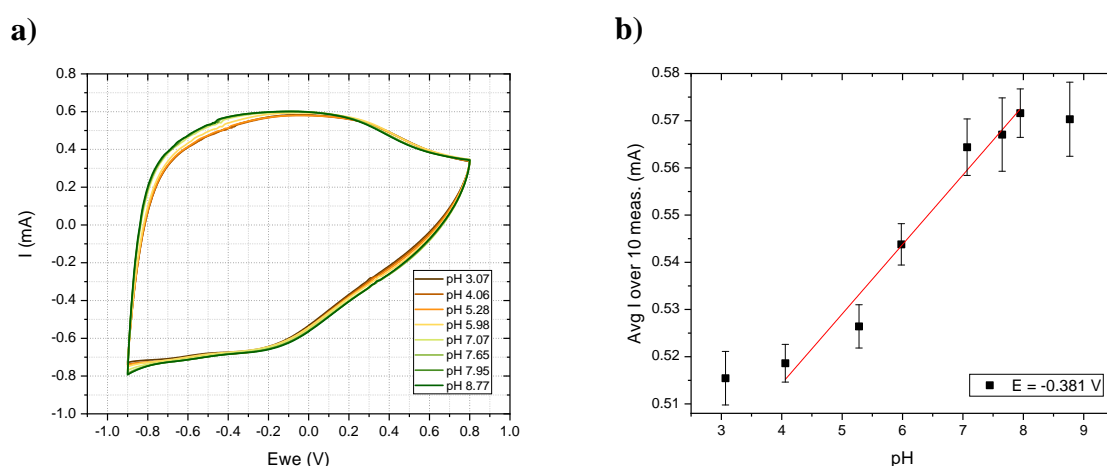
a)   b)

Figure 36: a) Voltammograms of sample B3S1 (big) in different pH and **b)** the behavior at one arbitrary selected potential within the reduction part of the cycle. Error bars show the standard deviation between the averaged cycles.
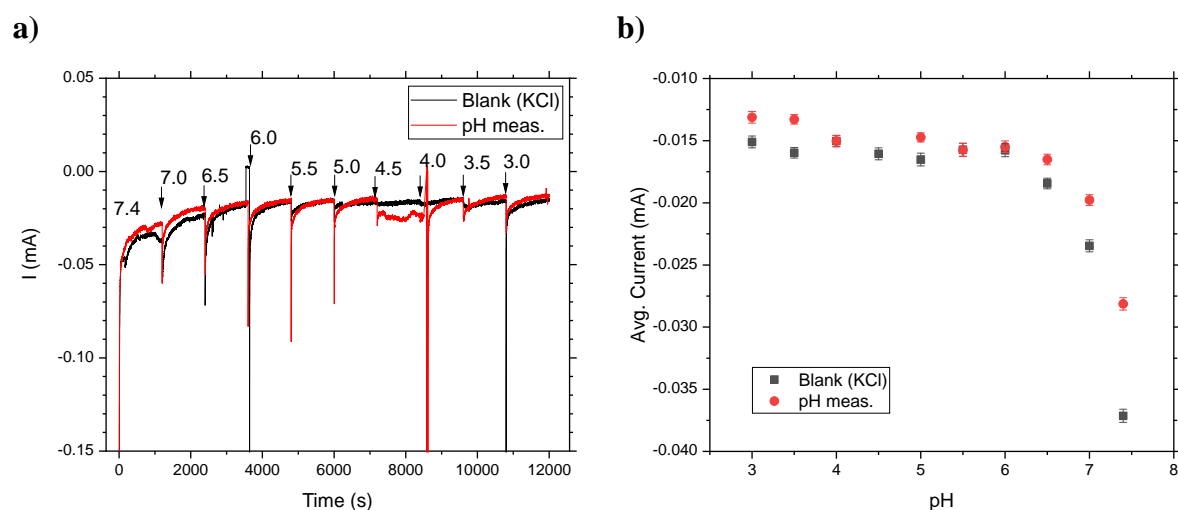
a)

b)

Figure 37: CA results with B3S3 (big). **a)** CA measurements. The arrows show when the pH was altered and the number above it indicates the pH target. The initial pH was 7.4. **b)** Average current from the last 30 seconds before another addition was made. In the blank measurement the initial pH does not change as shown by calibrations done before the measurement.

kind of transient can be seen even in the beginning of both, the blank and the pH measurement. This could indicate that the system was not yet stable when the experiment was begun. It is possible that this stabilization is seen because the pretreatment of the electrode was done around the OCP and during the measurement a DC potential was applied. Eventually both of the amperometric methods were discarded due to the low sensitivity in CV and relatively high amplitude of noise and the lack of a visible pH dependence in CA.

Next, impedance measurements were conducted to investigate the pH dependence. Figure 38 shows the pH dependence for three separate samples. In the figures, a color legend indicating the pH of the solution during the PEIS measurement is presented. Under each one of them, in Figure 38d) through f) the corresponding relative change is presented. The relative change has been calculated by first setting the initial situation (solution pH at 7.4) as 100%. Then for every measurement point for each frequency, the percentual change

$$\frac{\log|Z|_n - \log|Z|_i}{\log|Z|_i} \cdot 100\%$$

was calculated. This was done for both the actual measurement data presented in Figure 38a)-c) and the corresponding blank measurement data. The blank measurements' data is not presented, because they are practically identical to the initial situation of the actual measurement. After having both of these relative changes calculated, the blank measurement relative change was subtracted from the actual pH measurement relative change. Two different frequencies were selected to represent low (0.1 Hz) and mid (120 Hz) frequencies for Figure 38d)-f).
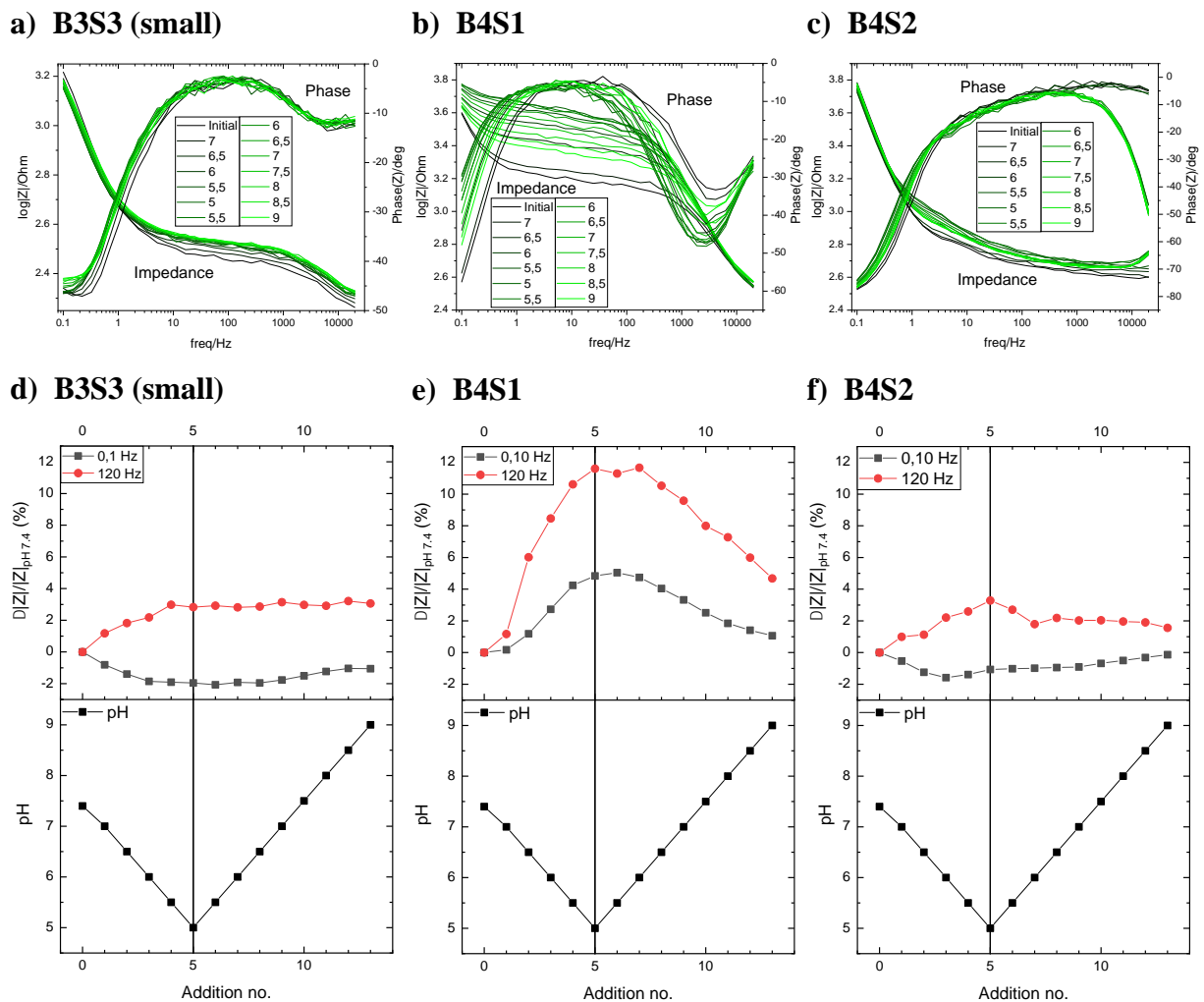

Figure 38: Impedance pH measurements with three different samples. Higher row shows the actual measurements and the lower row the relative change to the initial impedance value subtracted by the relative change seen in a corresponding blank measurement. **a)** and **d)** are for sample B3S3 (small), **b)** and **e)** for B4S1 and **c)** and **f)** for B4S2. These electrodes have areas of 2.5 mm^2, 1.8 mm^2 and 0.91 mm^2 respectively.

The first thing that can be seen from all the impedance curves of Figure 38a)-c) is that they all are of very different shapes. This type of variation can also be seen in the data of the different samples in Figure 35a)-c). Initially it was thought that maybe the oxidation level of these samples had been different to have such a different response. Therefore, Raman spectroscopy was used to determine the ratio $A(D)/A(G)$ and $w(D)$, $w(G)$ and $w(2D)$ for B4S1 and B4S2. These parameters are presented in Table 5. When compared to the characterization results presented in Table 4, $A(D)/A(G)$ seems to be closer to that of untreated EGNITE for both samples and both of the $w(D)$ values are closer to that of autoclaved EGNITE. However, $w(G)$ and $w(2D)$ for B4S1 are closer to that of untreated EGNITE and for B4S2 closer to autoclaved EGNITE. Hence, reproducibility can be believed to be an issue. Especially since these two electrodes compared were from the same batch. It is interesting to note that the sample B4S1 with the mentioned parameters closer to that of untreated EGNITE exhibits a bigger response to the change of pH. This could be a result of the oxygen groups, that the sample has more than the more reduced B4S2, being pH sensitive. It evokes the question is the autoclaving really a necessary treatment to make a pH meter out of EGNITE.

When looking at the response at mid-range frequencies (1000 – 10 Hz) for B3S3 (small), one can see that the phase angle is around zero. Therefore, the behavior is resistive and can be restricted by the resistance of the electrode material or the solution's bulk. The change within the impedance at those frequencies as the pH changes would indicate that the conductivity of the solution would change. However, this should not be the case, since the ionic concentration does not change. Only if the nature of ionic species (mainly the amount of charge per one ion) were to change drastically, the approximation of ionic concentration of the solution representing the conductivity would fail. This change does not happen and therefore, it would seem more likely that the impedance of the material changes at different pH values. This type of change in impedance when the phase angle is around zero can be seen to happen with the two other

Table 5: The used parameters for B4S1 and B4S2 to confirm their oxidization level

Parameter	B4S1	B4S2
$A(D)/A(G)$	1.75 ± 0.05	1.82 ± 0.02
$w(D)$ (cm^{-1})	132 ± 1	135.7 ± 1.3
$w(G)$ (cm^{-1})	77 ± 2	76.0 ± 1.2
$w(2D)$ (cm^{-1})	245 ± 13	223 ± 10

samples presented in Figure 38b) and c) within the frequency ranges of 1 Hz to 100 Hz for B4S1 and 100 Hz to 1 000 Hz for B4S2.

Another important observation from the impedance measurements is highlighted in Figure 38d)-f). Even though that in the graphs presented here a correlation between the pH and impedance can be seen, the process is not perfectly reversible. When the solution was made more acidic, the impedance seems to change in relation. But when the direction is changed and the solution is made more basic, the change is smaller. This could be because of degeneration of the material in acidic conditions. However, as seen in the long-term stability data discussed earlier, no clear indication of this happening can be seen. Therefore, it is more probable that maybe the pH sensitive surface charge reaches a saturation level and is not able to fully recover to the linear response when the pH is increased again.

An interesting effect that can be seen is that with the samples B3S3 (small) and B4S2 at 0.1 Hz impedance decreases when pH decreases, but with B4S1 the opposite effect can be seen. Since it was shown with the Raman data that B4S1 is not as reduced as the other samples and can therefore be assumed more resistive, it could explain this change in behavior: At 120 Hz a significantly larger impedance can be seen for B4S1 than for the rest of the samples. If this is due to the increased resistivity of the material, it could be so that the response seen at 0.1 Hz is still dominated by the same property that gives the significant 12 % increase at 120 Hz. Therefore, a lower frequency would have to be used to see the same type of decrease in impedance as can be seen with the other two samples. If this contamination of the response is taken into account, all of the trends shown in Figure 38d)-f) are quite similar for all of the three samples.

In order to find out what component of the EGNITE electrodes is the one that is causing the observed pH dependence, equivalent circuit fitting was used. Initial attempts with the Randles circuit were unsuccessful, because the fit would not converge. Therefore, because it is an inherent property of the solution and the material to have a resistance and a double layer capacitance was assumed to happen due to the phase change at low frequencies seen in Figure 38a)-c), the equivalent circuit presented in Figure 39 was selected. In it the resistance of the solution and the electrode material were assumed to be in series, so they were combined to form R_1 to simplify the fit. The double layer capacitance is represented as a CPE, because it rarely works like an ideal capacitor in real measurements. For the fitting, only measurement

points at frequencies equal to or lower than 120 Hz were used. This way the fitting did not have to take into account what can be seen in the high frequencies range, where the behavior is more difficult to interpret. The fitting results are presented in Figure 40 in percentual change that has been calculated in the same way as presented above and in Figure 41 the data is presented in the actual values from the fit. Both of these two figures are shown because the former one illustrates the shape of the change and the latter one shows the actual magnitude of the change.
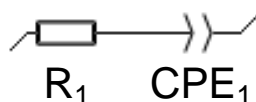

Figure 39: The equivalent circuit used for fitting. R_1 is the sum of resistances of the solution and electrode material and CPE_1 is a CPE representing the double layer formed at the electrode-electrolyte interface. The CPE_1 includes a fitting parameter a_1 that describes whether the element is behaving more like a resistor ($a_1 = 0$) or a capacitor ($a_1 = 1$).
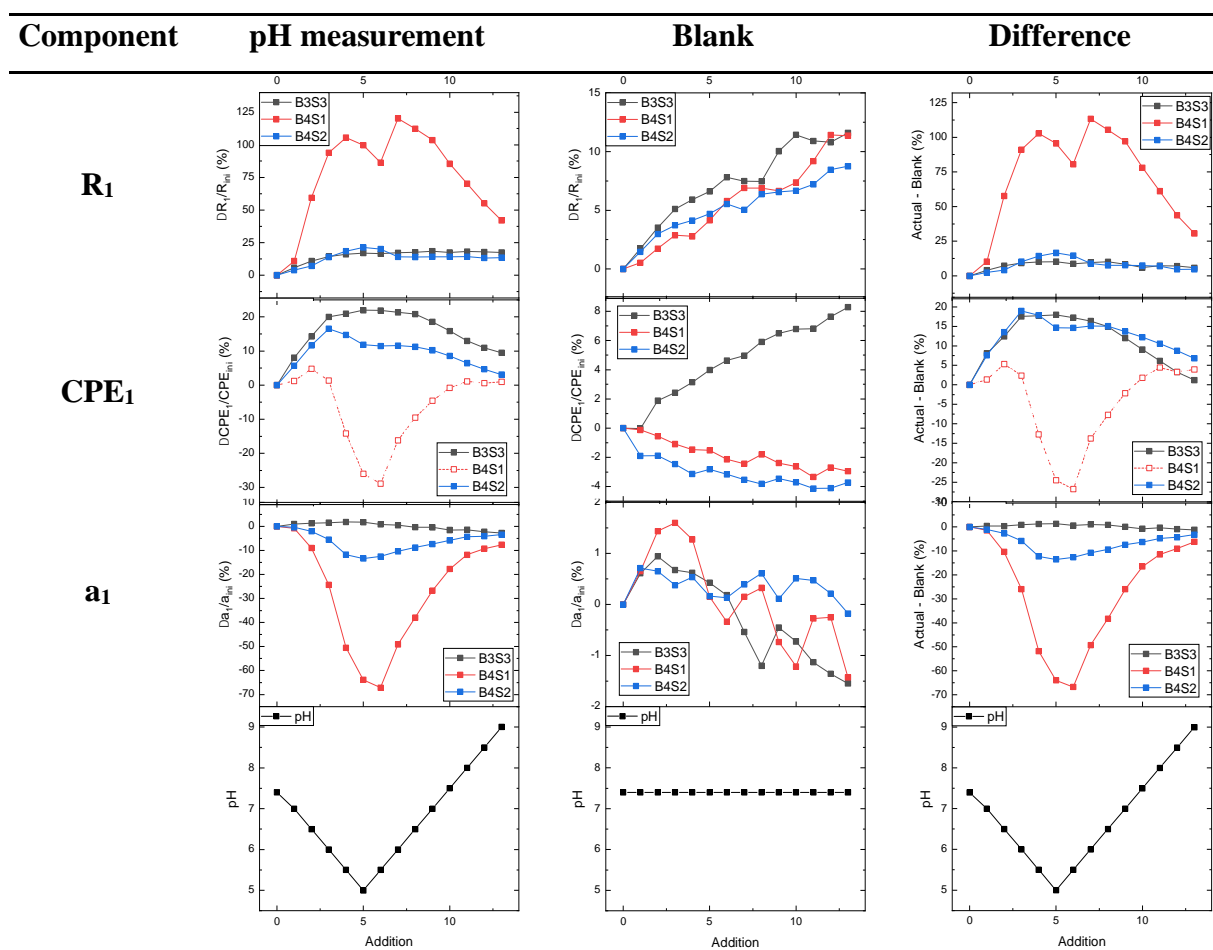

Figure 40: Equivalent circuit fitting results gained presented in percentual change to illustrate the behavior of the change as pH is altered. The samples presented here are B3S3 (small), B4S1 and B4S2 with areas of 2.5 mm^2, 1.8 mm^2 and 0.91 mm^2, respectively.

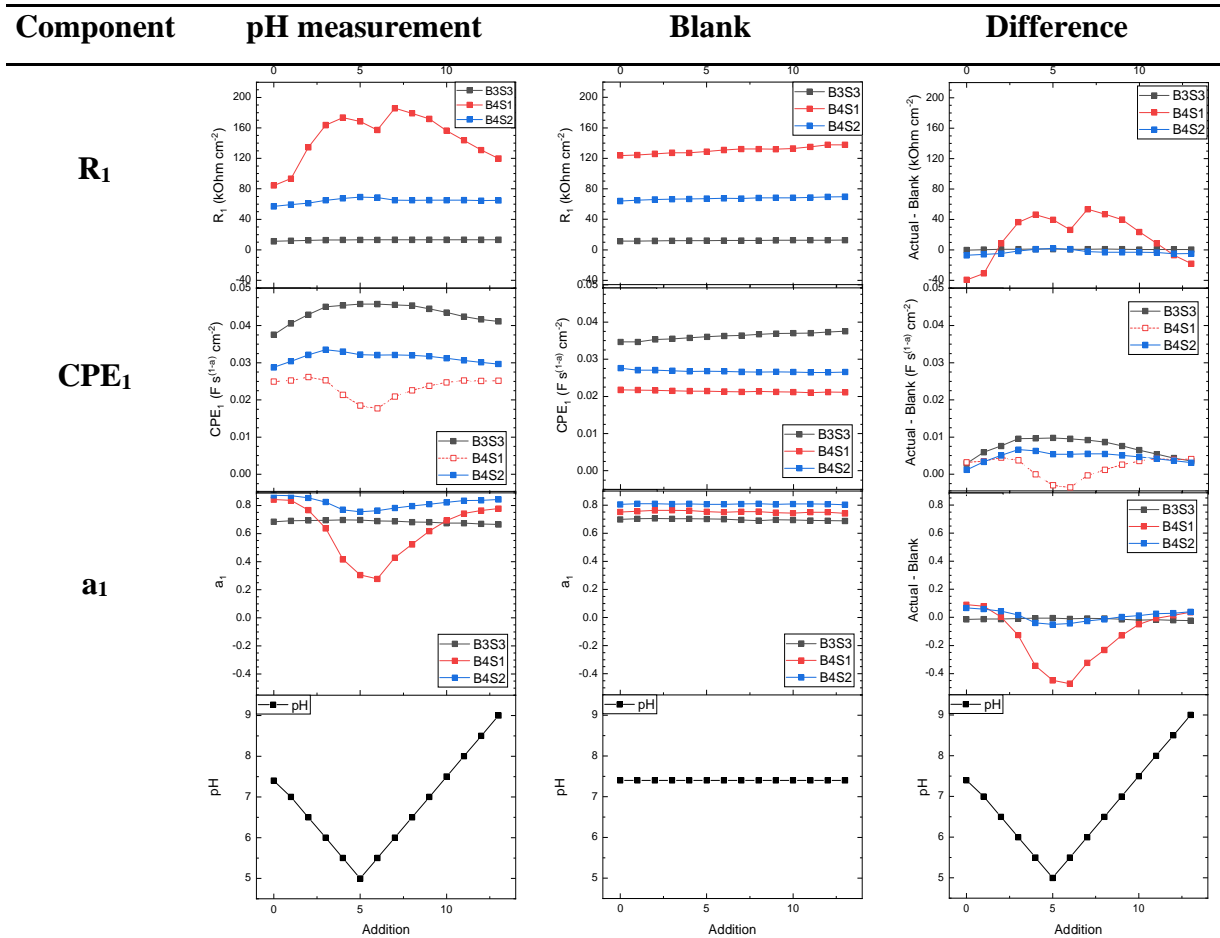| Component	pH measurement	Blank	Difference
R_1			
CPE_1			
a_1			

Figure 41: Equivalent circuit fitting results gained presented in actual values to illustrate the scale of the change as pH is altered. For each line of graphs, the scale is kept the same. The samples presented here are B3S3 (small), B4S1 and B4S2 with areas of 2.5 mm^2, 1.8 mm^2 and 0.91 mm^2, respectively.

For all fittings the quality parameter used was the Pearson's chi-squared test normalized with the square root of the total amount of samples ($\chi^2/\sqrt{N}$). Its values were between 0.02 and 0.4, which would indicate that the fittings can be trusted although some variance in the quality is apparent.

First of all, the most significant change in Figure 40 can clearly be seen in the pH measurements with the sample B4S1. A 125 % increase of the R_1 is present in the fitting results when the corresponding change with the other samples is around 20 %. However, a strange behavior is present in the lowest pH values, between 5 and 5.5. Here, the sample's R_1 seems to have a small decrease in resistance before returning to the arc-like behavior seen in the rest of the graph. However, if the parameter a_1 is taken into account, within the same additions, the CPE_1 is behaving more like a resistor (a_1 decreases). This could explain the decrease seen in R_1 as the

CPE_1 is contributing more to the total resistance. In addition, it would seem like this decrease is also seen in the Figure 38e) at the sixth addition at 120 Hz and the fitting makes this change more clearly visible. For the CPE_1, the most symmetric arc can be seen with B3S3 (small), but B4S2 also follows this shape relatively well. For these two samples here the percentual change is somewhat of the same scale to that seen with the R_1. However, B4S1 exhibits a decreasing capacitance when the pH decreases.

In the blank measurements, a drift can be seen in all of the parameters: R_1 seems to increase and a_1 decrease in a similar manner with all of the samples, but for CPE_1 the drift is downwards for B4S1 and B4S2 while it is upwards for B3S3 (small). However, as seen in Figure 41, this drift is very small when compared to the magnitude of the actual measurement. When the blank measurement is taken into account in the difference graphs it looks like the measurements have a clear pH dependence and that the process is somewhat reversible, although not perfectly. If the process were perfectly reversible, at the tenth addition the parameter's value would have returned to the initial state.

When inspecting all of the parameters fitted, it would seem like that both, the R_1 and CPE_1 exhibit pH sensitivity. However, as the sample B4S1 is more resistive due to it being less reduced, it exhibits a clear difference in behavior when compared to the rest of the samples. B4S1 has its R_1 change significantly when the pH is altered, but for the other two samples it seems more like that the response can be mainly seen in the CPE_1. If the solution resistance is assumed to be practically the same throughout all of the measurements, as discussed above, the change seen in R_1 would represent the change in the resistance of EGNITE. For B4S1 the response of R_1 seems to be so large that the corresponding CPE_1 is contaminated with it. Therefore, it is likely that the CPE_1 results for B4S1 cannot be trusted and thus they have been plotted in a distinguishable style in Figure 40 and Figure 41.

PEISW measurements over time were also measured to see if single frequency impedance measurements would show pH dependence. This was because of the pH dependence detected at low frequencies with PEIS. Frequency of 1 Hz was selected, because without any in-depth analysis of the impedance spectra of Figure 38a)-c) the pH dependence seemed to be clearer at lower frequencies. In addition, using frequencies lower than 1 Hz would give a very low time resolution, so one point every 3 seconds was chosen. The data measured is presented in Figure 42. A decrease in impedance can be seen after each addition, which at first seemed to
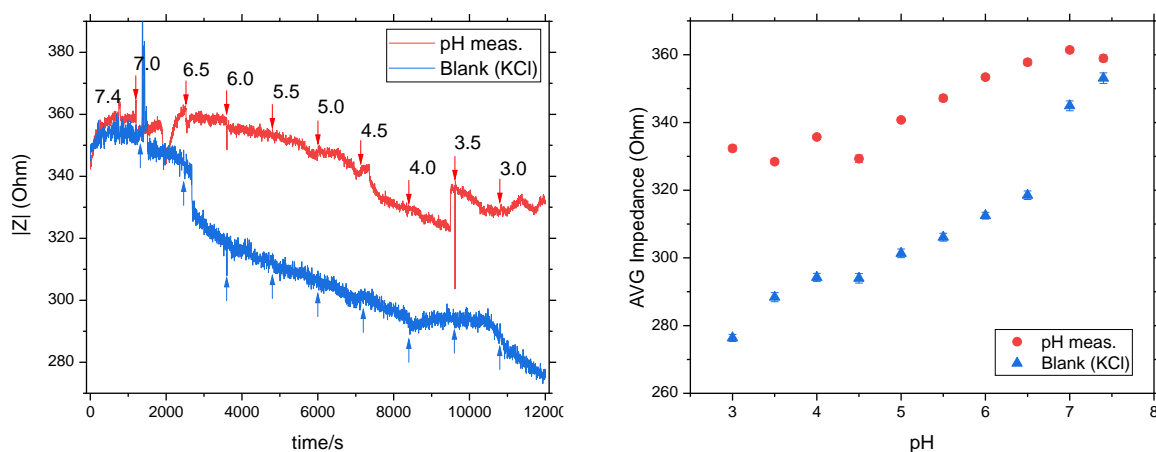
Figure 42: PEISW measurements with B3S3 (small). **a)** shows the actual measurements with arrows pointing when the pH was altered with the target pH written above it. **b)** shows the average impedance from the last 30 seconds before a new addition.

have some correlation with the pH. However, when compared with the blank measurement, which had the same pH for the whole measurement, the difference between the two of them is constant most of the time. Therefore, no pH dependence is detected, but only a change over time or due to the change of ionic species or volume of the solution.

13 Summary and Conclusions

EGNITE was found to be a highly capacitive material that exceeds many other graphene-based materials with its properties. The material seems to be durable even in long-term with several measurements conducted in highly acidic or basic environments. Optical and SEM images showed that the macroscopic structure becomes rougher with autoclaving. Furthermore, according to the XPS and Raman measurements, the treatment successfully removes oxygen from the material, increases the amount of defects and increases conductivity. The increase in defect concentration is still low, so that EGNITE stays in a low defect concentration stage. For electrochemical measurements a successful pretreatment method to stabilize EGNITE electrodes was found although due to unknown factors sample to sample reproducibility was not reliable. This can easily be seen in the PEIS graphs presented. Most likely this is due to the fact that each electrode was made by hand.

The inaccuracy in the characterization and other measurements was contributed by the fact that only two samples were used for Raman, XPS and SEM measurements. This inaccuracy can be

the reason to the dispersion between samples, especially in the PEIS spectra shown here. This can be because the initial and the final states of EGNITE can vary from batch to batch. Also, differences seen in pH response in PEIS measurements raised questions if the autoclaving is really necessary in making a pH detector out of EGNITE or would a greater amount of oxygen groups on the surface and therefore a greater surface charge of the material increase the pH sensitivity.

PEIS, CV, PEISW and CA measurement techniques were studied in attempt to find a working method to use EGNITE electrodes to measure pH of a solution. It seems that EGNITE is sensitive to pH, but the measurement techniques used here did not achieve perfectly reversible results although some reversibility can be detected. Based on the data presented here, it would seem to be possible to find a stable and more reversible measurement method by altering the measurement parameters. An example of a possible alteration for a measurement technique could be measuring PEIS against OCP instead of a forced 0 V potential across WE and RE. Another explanation for the irreversibility of the response could be degeneration of the electrode material during the measurements, but the long-term stability measurements do not indicate that this type of behavior would have happened.

In summary, EGNITE exhibits very promising properties as a material for different biocompatible or biosensor applications. However, within the work presented here, no clear and perfectly reproducible measurement methods were found. In the future, the reproducibility and optimization of the electrochemical measurement methods presented here should be studied further in order to create a working and reliable ways to use EGNITE as a detector.

Literature

1. Bard, A. J. and Faulkner, L. R., *Electrochemical Methods: Fundamentals and Applications*, 2nd edition, John Wiley & Sons, Inc., New York, 2001.

2. Sturala, J.; Luxa, J.; Pumera, M. and Sofer, Z., Chemistry of Graphene Derivatives: Synthesis, Applications, and Perspectives, *Chem. - A Eur. J.*, **2018**, *24*, 5992–6006.

3. Jia, W.; Bandodkar, A. J.; Valdés-Ramírez, G.; Windmiller, J. R.; Yang, Z.; Ramírez, J.; Chan, G. and Wang, J., Electrochemical tattoo biosensors for real-time noninvasive lactate monitoring in human perspiration, *Anal. Chem.*, **2013**, *85*, 6553–6560.

4. Bonanni, A. and Pumera, M., Graphene platform for hairpin-DNA-based impedimetric genosensing, *ACS Nano*, **2011**, *5*, 2356–2361.

5. Justino, C. I. L.; Gomes, A. R.; Freitas, A. C.; Duarte, A. C. and Rocha-Santos, T. A. P., Graphene based sensors and biosensors, *TrAC - Trends Anal. Chem.*, **2017**, *91*, 53–66.

6. Novoselov, K. S.; Geim, A. K.; Morozov, S. V.; Jiang, D.; Zhang, Y.; Dubonos, S. V.; Grigorieva, I. V. and Firsov, A. A., Electric field in atomically thin carbon films, *Science (80-.).*, **2004**, *306*, 666–669.

7. Allen, M. J.; Tung, V. C. and Kaner, R. B., Honeycomb carbon: A review of graphene, *Chem. Rev.*, **2010**, *110*, 132–145.

8. Avouris, P., Graphene: Electronic and photonic properties and devices, *Nano Lett.*, **2010**, 10, 4285–4294.

9. Shao, Y.; Wang, J.; Wu, H.; Liu, J.; Aksay, I. A. and Lin, Y., Graphene Based Electrochemical Sensors and Biosensors: A Review, *Electroanalysis*, **2010**, *22*, 1027–1036.

10. Zhou, M.; Zhai, Y. and Dong, S., Electrochemical sensing and biosensing platform based on chemically reduced graphene oxide, *Anal. Chem.*, **2009**, *81*, 5603–5613.

11. Lin, W. J.; Liao, C. S.; Jhang, J. H. and Tsai, Y. C., Graphene modified basal and edge plane pyrolytic graphite electrodes for electrocatalytic oxidation of hydrogen peroxide and β-nicotinamide adenine dinucleotide, *Electrochem. commun.*, **2009**, *11*, 2153–2156.

12. Shang, N. G.; Papakonstantinou, P.; McMullan, M.; Chu, M.; Stamboulis, A.; Potenza, A.; Dhesi, S. S. and Marchetto, H., Catalyst-Free Efficient Growth, Orientation and Biosensing Properties of Multilayer Graphene Nanoflake Films with Sharp Edge Planes, *Adv. Funct. Mater.*, **2008**, *18*, 3506–3514.

13. Tang, L.; Wang, Y.; Li, Y.; Feng, H.; Lu, J. and Li, J., Preparation, Structure, and Electrochemical Properties of Reduced Graphene Sheet Films, *Adv. Funct. Mater.*, **2009**, *19*, 2782–2789.

14. Venkateshalu, S. and Grace, A. N., Review — Heterogeneous 3D Graphene Derivatives for Supercapacitors, *J. Electrochem. Soc.*, **2020**, *167*, 050509.

15. Ke, Q. and Wang, J., Graphene-based materials for supercapacitor electrodes – A review, *J. Mater.*, **2016**, *2*, 37–54.

16. Xin, H. and Li, W., A review on high throughput roll-to-roll manufacturing of chemical vapor deposition graphene, *Appl. Phys. Rev.*, **2018**, *5*, 031105.

17. Singh, D. P.; Herrera, C. E.; Singh, B.; Singh, S.; Singh, R. K. and Kumar, R., Graphene oxide: An efficient material and recent approach for biotechnological and biomedical applications, *Mater. Sci. Eng. C*, **2018**, *86*, 173–197.

18. Ambrosi, A.; Chua, C. K.; Latiff, N. M.; Loo, A. H.; Wong, C. H. A.; Eng, A. Y. S.; Bonanni, A. and Pumera, M., Graphene and its electrochemistry-an update, *Chem. Soc. Rev.*, **2016**, *45*, 2458–2493.

19. Chen, D.; Feng, H. and Li, J., Graphene oxide: Preparation, functionalization, and electrochemical applications, *Chem. Rev.*, **2012**, *112*, 6027–6053.

20. Zuo, X.; He, S.; Li, D.; Peng, C.; Huang, Q.; Song, S. and Fan, C., Graphene oxide-facilitated electron transfer of metalloproteins at electrode surfaces, *Langmuir*, **2010**, *26*, 1936–1939.

21. Amiri, A.; Naraghi, M.; Ahmadi, G.; Soleymaniha, M. and Shanbedi, M., A review on liquid-phase exfoliation for scalable production of pure graphene, wrinkled, crumpled and functionalized graphene and challenges, *FlatChem*, **2018**, 8, 40–71.

22. Park, S.; An, J.; Jung, I.; Piner, R. D.; An, S. J.; Li, X.; Velamakanni, A. and Ruoff, R. S., Colloidal suspensions of highly reduced graphene oxide in a wide variety of organic solvents, *Nano Lett.*, **2009**, *9*, 1593–1597.

23. Chen, L.; Tang, Y.; Wang, K.; Liu, C. and Luo, S., Direct electrodeposition of reduced graphene oxide on glassy carbon electrode and its electrochemical application, *Electrochem. commun.*, **2011**, *13*, 133–137.

24. Yang, H.; Cao, Y.; He, J.; Zhang, Y.; Jin, B.; Sun, J. L.; Wang, Y. and Zhao, Z., Highly conductive free-standing reduced graphene oxide thin films for fast photoelectric devices, *Carbon N. Y.*, **2017**, *115*, 561–570.

25. Yang, X.; Chen, H.; Li, J. and Xu, M., Chemical Methods for Graphene Synthesis. In: Xu, Z. (ed.), *Graphene: Properties, Synthesis and Applications*, Nova Science Publishers, Incorporated, New York, 2012, pp. 112–124.

26. Hiew, B. Y. Z.; Lee, L. Y.; Lee, X. J.; Thangalazhy-Gopakumar, S.; Gan, S.; Lim, S. S.; Pan, G. T.; Yang, T. C. K.; Chiu, W. S. and Khiew, P. S., Review on synthesis of 3D

graphene-based configurations and their adsorption performance for hazardous water pollutants, *Process Saf. Environ. Prot.*, **2018**, *116*, 262–286.

27. Wang, X.; Zhang, Y.; Zhi, C.; Wang, X.; Tang, D.; Xu, Y.; Weng, Q.; Jiang, X.; Mitome, M.; Golberg, D. and Bando, Y., Three-dimensional strutted graphene grown by substrate-free sugar blowing for high-power-density supercapacitors, *Nat. Commun.*, **2013**, *4*, 1–8.

28. Zhang, X.; Sui, Z.; Xu, B.; Yue, S.; Luo, Y.; Zhan, W. and Liu, B., Mechanically strong and highly conductive graphene aerogel and its use as electrodes for electrochemical power sources, *J. Mater. Chem.*, **2011**, *21*, 6494–6497.

29. He, Y.; Li, J.; Luo, K.; Li, L.; Chen, J. and Li, J., Engineering Reduced Graphene Oxide Aerogel Produced by Effective γ-ray Radiation-Induced Self-Assembly and Its Application for Continuous Oil-Water Separation, *Ind. Eng. Chem. Res.*, **2016**, *55*, 3775–3781.

30. Kostarelos, K.; Vincent, M.; Hebert, C. and Garrido, J. A., Graphene in the Design and Engineering of Next-Generation Neural Interfaces, *Adv. Mater.*, **2017**, *29*, 1700909.

31. Mohan, V. B.; Lau, K. tak; Hui, D. and Bhattacharyya, D., Graphene-based materials and their composites: A review on production, applications and product limitations, *Compos. Part B Eng.*, **2018**.

32. Song, P.; Cao, Z.; Cai, Y.; Zhao, L.; Fang, Z. and Fu, S., Fabrication of exfoliated graphene-based polypropylene nanocomposites with enhanced mechanical and thermal properties, *Polymer (Guildf).*, **2011**, *52*, 4001–4010.

33. Quan, W.; Tang, Z. L.; Wang, S. T.; Hong, Y. and Zhang, Z. T., Facile preparation of free-standing rGO paper-based Ni-Mn LDH/graphene superlattice composites as a pseudocapacitive electrode, *Chem. Commun.*, **2016**, *52*, 3694–3696.

34. Huang, X.; Qi, X.; Boey, F. and Zhang, H., Graphene-based composites, *Chem. Soc. Rev.*, **2012**, 41, 666–686.

35. Ohno, H.; Yoshizawa, M. and Ogihara, W., Development of new class of ion conductive polymers based on ionic liquids, *Electrochim. Acta*, **2004**, *50*, 255–261.

36. Subbarao, E. C., *Solid Electrolytes and Their Applications*, Springer US, 1980.

37. Lefrou, C.; Fabry, P. and Poignet, J. C., *Electrochemistry: The Basics, with Examples*, Springer Berlin Heidelberg, 2012.

38. Harris, D. C., *Quantitative Chemical Analysis*, 8th edition, W. H. Freeman, New York, 2010.

39. Knight, R. D., *Physics for Scientists and Engineers: A Strategic Approach with Modern*

Physics, Global Edition., 4th edition, Pearson, San Francisco, 2016.

40. Stern, O., The theory of the electrolytic double-layer, *Z. Elektrochem*, **1924**, *30*, 1014–1020.

41. Tadros, T. F., Origin of charge at interfaces: Structure of the electrical double layer. In: *Interfacial Phenomena and Colloid Stability: Basic Principles*, De Gruyter, 2015, pp. 19–37.

42. Elgrishi, N.; Rountree, K. J.; McCarthy, B. D.; Rountree, E. S.; Eisenhart, T. T. and Dempsey, J. L., A Practical Beginner's Guide to Cyclic Voltammetry, *J. Chem. Educ.*, **2018**, *95*, 197–206.

43. Zhou, Y.; Yin, H.; Meng, X.; Xu, Z.; Fu, Y. and Ai, S., Direct electrochemistry of sarcosine oxidase on graphene, chitosan and silver nanoparticles modified glassy carbon electrode and its biosensing for hydrogen peroxide, *Electrochim. Acta*, **2012**, *71*, 294–301.

44. Nicholson, R. S., Theory and Application of Cyclic Voltammetry for Measurement of Electrode Reaction Kinetics, *Anal. Chem.*, **1965**.

45. Compton, R. G.; Laborda, E. and Ward, K. R., *Understanding Voltammetry: Simulation of Electrode Processes*, Imperial College Press, London, 2013.

46. Mirceski, V.; Komorsky-Lovric, S. and Lovric, M., *Square Wave Voltammetry: Theory and Application*, Springer Berlin Heidelberg, 2007.

47. Pumera, M., Graphene in biosensing, *Mater. Today*, **2011**, *14*, 308–315.

48. Clark, L. C. and Lyons, C., Electrode Systems for Continuous Monitoring in Cardiovascular Surgery, *Ann. N. Y. Acad. Sci.*, **1962**, *102*, 29–45.

49. Kim, J.; Campbell, A. S.; de Ávila, B. E. F. and Wang, J., Wearable biosensors for healthcare monitoring, *Nat. Biotechnol.*, **2019**, 37, 389–406.

50. Turner, A. P. F., Biosensors: sense and sensibility, *Chem. Soc. Rev.*, **2013**, *42*, 3184.

51. Kong, F. Y.; Gu, S. X.; Li, W. W.; Chen, T. T.; Xu, Q. and Wang, W., A paper disk equipped with graphene/polyaniline/Au nanoparticles/glucose oxidase biocomposite modified screen-printed electrode: Toward whole blood glucose determination, *Biosens. Bioelectron.*, **2014**, *56*, 77–82.

52. Xu, Q.; Gu, S. X.; Jin, L.; Zhou, Y. E.; Yang, Z.; Wang, W. and Hu, X., Graphene/polyaniline/gold nanoparticles nanocomposite for the direct electron transfer of glucose oxidase and glucose biosensing, *Sensors Actuators, B Chem.*, **2014**, *190*, 562–569.

53. Du, D.; Wang, J.; Wang, L.; Lu, D. and Lin, Y., Integrated lateral flow test strip with

electrochemical sensor for quantification of phosphorylated cholinesterase: Biomarker of exposure to organophosphorus agents, *Anal. Chem.*, **2012**, *84*, 1380–1385.

54. Schneider, L. A.; Korber, A.; Grabbe, S. and Dissemond, J., Influence of pH on wound-healing: a new perspective for wound-therapy?, *Arch. Dermatol. Res.*, **2007**, *298*, 413–420.

55. Schröter, A.; Walther, A.; Fritzsche, K.; Kothe, J.; Rösen-Wolff, A. and Gerlach, G., Infection Monitoring in Wounds, *Procedia Chem.*, **2012**, *6*, 175–183.

56. Melai, B.; Salvo, P.; Calisi, N.; Moni, L.; Bonini, A.; Paoletti, C.; Lomonaco, T.; Mollica, V.; Fuoco, R. and Di Francesco, F., A graphene oxide pH sensor for wound monitoring, *2016 38th Annu. Int. Conf. IEEE Eng. Med. Biol. Soc.*, IEEE, 2016, pp. 1898–1901.

57. Wu, J. Bin; Lin, M. L.; Cong, X.; Liu, H. N. and Tan, P. H., Raman spectroscopy of graphene-based materials and its applications in related devices, *Chem. Soc. Rev.*, **2018**, *47*, 1822–1873.

58. Atkins, P. W. and de Paula, J., *Atkins' Physical chemistry*, 10th edition, 2014.

59. Tan, P. H.; Hu, C. Y.; Dong, J.; Shen, W. C. and Zhang, B. F., Polarization properties, high-order Raman spectra, and frequency asymmetry between Stokes and anti-Stokes scattering of Raman modes in a graphite whisker, *Phys. Rev. B - Condens. Matter Mater. Phys.*, **2001**, *64*.

60. Johansson, A.; Myllyperkiö, P.; Koskinen, P.; Aumanen, J.; Koivistoinen, J.; Tsai, H.-C.; Chen, C.-H.; Chang, L.-Y.; Hiltunen, V.-M.; Manninen, J. J.; Woon, W. Y. and Pettersson, M., Optical Forging of Graphene into Three-Dimensional Shapes, *Nano Lett.*, **2017**, *17*, 6469–6474.

61. Eckmann, A.; Felten, A.; Mishchenko, A.; Britnell, L.; Krupke, R.; Novoselov, K. S. and Casiraghi, C., Probing the Nature of Defects in Graphene by Raman Spectroscopy, *Nano Lett.*, **2012**, *12*, 3925–3930.

62. Ma, B.; Rodriguez, R. D.; Ruban, A.; Pavlov, S. and Sheremet, E., The correlation between electrical conductivity and second-order Raman modes of laser-reduced graphene oxide, *Phys. Chem. Chem. Phys.*, **2019**, *21*, 10125–10134.

63. Díez-Betriu, X.; Álvarez-García, S.; Botas, C.; Álvarez, P.; Sánchez-Marcos, J.; Prieto, C.; Menéndez, R. and De Andrés, A., Raman spectroscopy for the study of reduction mechanisms and optimization of conductivity in graphene oxide thin films, *J. Mater. Chem. C*, **2013**, *1*, 6905–6912.

64. Ott, C.; Kaldun, A.; Raith, P.; Meyer, K.; Laux, M.; Evers, J.; Keitel, C. H.; Greene, C.

H. and Pfeifer, T., Lorentz meets Fano in spectral line shapes: A universal phase and its laser control, *Science (80-.).*, **2013**, *340*, 716–720.

65. Atkins, P. and de Paula, J., *Atkins' Physical chemistry*, 8th edition, Oxford University Press, New York, 2006.

66. Goldstein, J. I.; Newbury, D. E.; Michael, J. R.; Ritchie, N. W. M.; Scott, J. H. J. and Joy, D. C., *Scanning electron microscopy and x-ray microanalysis*, 4th edition, Springer New York, 2017.

67. Vickerman, J. C. and Gilmore, I. S., *Surface Analysis - The Principal Techniques: Second Edition*, John Wiley & Sons, Ltd., 2009.

68. Fairely, N. and Casa Software Ltd., *CasaXPS Manual 2.3.15 Introduction to XPS and AES*, Casa Software Ltd, 2009.

69. Thermo Scientific XPS: Knowledge Base, https://xpssimplified.com/periodictable.php (15.1.2020).

70. Beamson, G. and Briggs, D., *High Resolution XPS of Organic Polymers*, John Wiley & Sons, Ltd, Chichester, UK, 1992.

71. Shirley, D. A., High-resolution x-ray photoemission spectrum of the valence bands of gold, *Phys. Rev. B*, **1972**, *5*, 4709–4714.

72. Gross, S. and Armelao, L., XPS as a powerful tool to investigate the surface properties of simple, doped and mixed metal oxides. In: Wagner, J. M. (ed.), *X-Ray Photoelectron Spectroscopy*, Nova Science Publishers, Incorporated, New York, 2011, pp. 134–135.

73. Shao, Y.; Wang, H.; Zhang, Q. and Li, Y., Fabrication of large-area and high-crystallinity photoreduced graphene oxide films via reconstructed two-dimensional multilayer structures, *NPG Asia Mater.*, **2014**, *6*.

74. Conway, B. E.; Birss, V. and Wojtowicz, J., The role and utilization of pseudocapacitance for energy storage by supercapacitors, *J. Power Sources*, **1997**, *66*, 1–14.

75. Macdonald, J. R.; Johnson, W. B.; Raistrick, I. D.; Franceschetti, D. R.; McKubre, M. C. H.; Macdonald, D. D.; Bonanos, N.; Steele, B. C. H. and Butler, E. P., *Impedance Spectroscopy: Theory, Experiment, and Applications.*, Second, Wiley-Interscience, 2005.

76. Murer, N. and Diard, J.-P., Introduction to EIS (Electrochemical Impedance Spectroscopy) with EC-Lab / EC-Lab Express, **2019**, 1–23.

77. Drieschner, S.; Guimerà, A.; Cortadella, R. G.; Viana, D.; Makrygiannis, E.; Blaschke, B. M.; Vieten, J. and Garrido, J. A., Frequency response of electrolyte-gated graphene
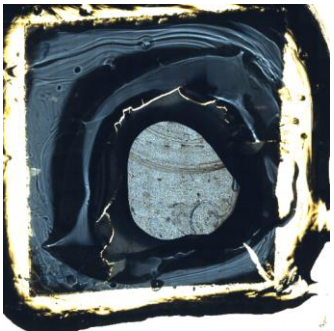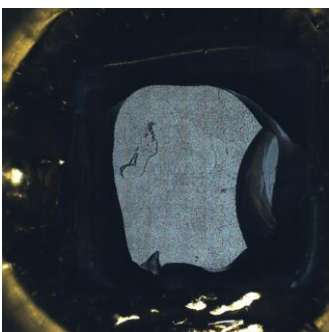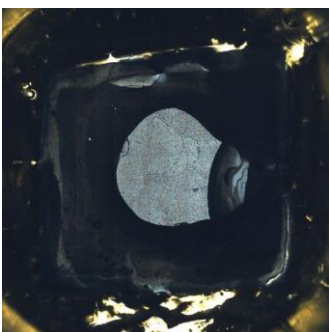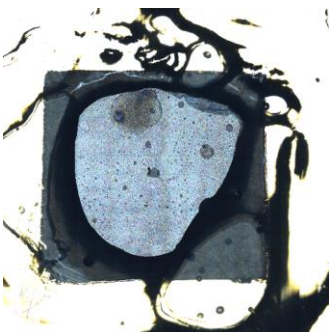
electrodes and transistors, *J. Phys. D. Appl. Phys.*, **2017**, *50*, 095304.

78. Walson, S. T., Presentation on Synthesis of Materials Graphene Oxide Electrodes, *4th Meet. Biomed. Technol. Graphene Flagsh.*, Barcelona, 2019.

79. Walson, S. T., Presentation on Technology of Neural Devices and Electronics, *4th Meet. Biomed. Technol. Graphene Flagsh.*, Barcelona, 2019.

80. OriginPro 2017, *SR1 b9.4.1.354*, OriginLab Corporation, Northampton, MA, USA.

81. Open source and Natterer, M., GIMP - GNU image manipulation program.

82. Schindelin, J.; Arganda-Carreras, I.; Frise, E.; Kaynig, V.; Longair, M.; Pietzsch, T.; Preibisch, S.; Rueden, C.; Saalfeld, S.; Schmid, B.; Tinevez, J.-Y.; White, D. J.; Hartenstein, V.; Eliceiri, K.; Tomancak, P. and Cardona, A., Fiji: an open-source platform for biological-image analysis, *Nat. Methods*, **2012**, *9*, 676–682.

83. Sigma-Aldrich, Phosphate buffered saline, https://www.sigmaaldrich.com/catalog/product/sigma/p4417 (17.10.2019).

84. Chiu, N.-F.; Huang, T.-Y. and Lai, H.-C., Graphene Oxide Based Surface Plasmon Resonance Biosensors. In: *Advances in Graphene Science*, InTech, 2013.

85. Mahmoud, A.; Olivier, J.; Vaxelaire, J. and Hoadley, A. F. A., Electrical field: A historical review of its application and contributions in wastewater sludge dewatering, *Water Res.*, **2010**, *44*, 2381–2407.

86. Scanning Electron Microscopy - Nanoscience Instruments, https://www.nanoscience.com/techniques/scanning-electron-microscopy/ (2.12.2019).

87. Gamry Instruments, Basics of EIS: Electrochemical Research-Impedance, https://www.gamry.com/application-notes/EIS/basics-of-electrochemical-impedance-spectroscopy/ (29.1.2020).
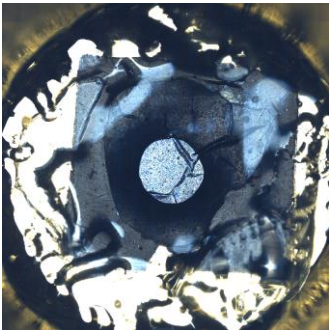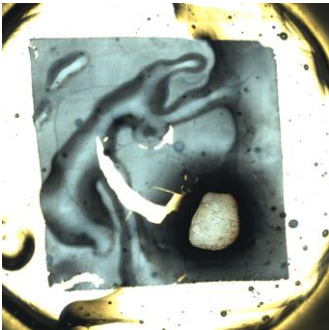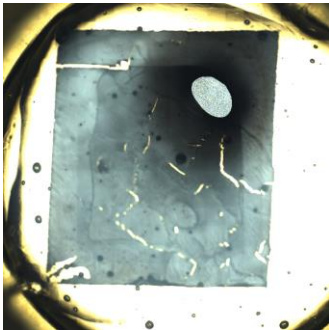
Appendices

Samples

Appendix Table 1: Samples used in material characterization and initial measurements

B1S1	B1S2	B2S1
See Figure 25a) for image	See Figure 25b) for image	
		A = 7.6 mm^2

B3S1 (big)	B3S1 (small)	B3S3 (big)
A = 16.2 mm^2	A = 6.9 mm^2	A = 15.2 mm^2

Appendix Table 2: Samples used for pH measurements

B3S3 (small)	B4S1	B4S2
A = 2.5 mm^2	A = 1.8 mm^2	A = 0.9 mm^2

Activation Protocol

Appendix Table 3: Activation protocol parameters for first PEIS

E_{we}	f_i (kHz)	f_f (Hz)	Points per decade	Amplitude (mV)
0	20.0	1	6	10

All used frequencies for PEIS (Hz)
20 000, 13 458, 9 056, 6 094, 4 101, 2 759, 1 857, 1 250, 841, 566, 381, 256, 172, 116, 78.1, 52.5, 35.3, 23.8, 16.0, 10.8, 7.25, 4.88, 3.28, 2.21, 1.49, 1.00

Appendix Table 4: Activation protocol parameters for CV

Set no	$E_{we\ ini}$ (V)	dE/dt (mV/s)	E_1 (V)	E_2 (V)	Cycles
1	0	5 000	- 0.5	0.5	750
2	0	5 000	- 0.7	0.7	750
3	0	5 000	- 0.9	0.8	750
4	0	500	- 0.9	0.8	30
5	0	200	- 0.9	0.8	30
6	0	100	- 0.9	0.8	15
7	0	50	- 0.9	0.8	20

Appendix Table 5: Activation protocol parameters for second PEIS

E_{we}	f_i (kHz)	f_f (Hz)	Points per decade	Amplitude (mV)
0	20.0	0.1	6	10

All used frequencies for PEIS (Hz)
20 000, 13 491, 9 100, 6 138, 4 140, 2 793, 1 884, 1 271, 857, 578, 390, 263, 177, 120, 80.7, 54.5, 36.7, 24.8, 16.7, 11.3, 7.60, 5.13, 3.46, 2.33, 1.57, 1.06, 0.72, 0.48, 0.33, 0.22, 0.15, 0.10

Long-term stability

Appendix Table 6: Long term stability parameters for PEIS

E_{we}	f_i (kHz)	f_f (Hz)	Points per decade	Amplitude (mV)
0	20.0	0.1	6	10

All used frequencies for PEIS (Hz)
20 000, 13 491, 9 100, 6 138, 4 140, 2 793, 1 884, 1 271, 857, 578, 390, 263, 177, 120, 80.7, 54.5, 36.7, 24.8, 16.7, 11.3, 7.60, 5.13, 3.46, 2.33, 1.57, 1.06, 0.72, 0.48, 0.33, 0.22, 0.15, 0.10

Appendix Table 7: Long term stability parameters for CV

$E_{we\ ini}$ (V)	dE/dt (mV/s)	E_1 (V)	E_2 (V)	Cycles
0	50	-0.4	0.4	10

The used program for integrating the area of a cyclic voltammogram without the other sub programs called in the program. Some extra comments have been added after a single quote symbol (') to explain the function of these calls.

```vba
Sub CapacitanceIntegral(Optional SheetIndexNro As Integer)
'define variables
Dim SRACell As Range
Dim PotWindowCell As Range
Dim Area As Double
Dim PotWindow As Double
Dim Sr As Double
Dim Strt As Range
Dim Rslt As Range
Dim Laps As Integer
Dim V1 As Double
Dim V2 As Double
Dim i1 As Double
Dim i2 As Double
Dim CurrentCycle As Integer
Set xValuesUp = CreateObject("System.Collections.ArrayList")
Set xValuesDown = CreateObject("System.Collections.ArrayList")
Set yValuesUp = CreateObject("System.Collections.ArrayList")
Set yValuesDown = CreateObject("System.Collections.ArrayList")
Dim ValuesUp() As Double
Dim ValuesDown() As Double

'Find data and cycle's number
    Area = 0.1524 ' InputBox("Area of electrode? (mm^2)", , 0.1524)
    PotWindow = 0.8 ' InputBox("Potential window? (V)", , 0.8)
    Sr = 0.05 ' InputBox("Scanrate? (V/s)", , 0.05)
    If SheetIndexNro >= 18 Then Area = 0.02467

    ' Find the number of cycles
    Range("A1").Select
    Cells.Find(What:="cycle number", After:=ActiveCell, LookIn:=xlFormulas, LookAt _
        :=xlPart, SearchOrder:=xlByRows, SearchDirection:=xlNext, MatchCase:= _
        False).Activate
    ActiveCell.Offset(-1, 0).Range("A1").Select
    ActiveCell.FormulaR1C1 = "=MAX(R[2]C:R[1048500]C)"
    Laps = ActiveCell.Value - 1
    ActiveCell.Formula = ""
    ActiveCell.Offset(1, 0).Range("A1").Activate

    ' Set up the area for results
    Set Strt = ActiveCell
    Do While ActiveCell.Value <> Empty
        Selection.End(xlToRight).Select
        ActiveCell.Offset(0, 3).Range("A1").Select
    Loop
    Set Rslt = ActiveCell
    ActiveCell.Value = "Cycle nro."
```

```
    ActiveCell.Offset(-1, 1).Range("A1").Select
    ActiveCell.Value = "Integral result"
    ActiveCell.Offset(1, 0).Range("A1").Select
    ActiveCell.Value = "Area Down"
    ActiveCell.Offset(0, 1).Range("A1").Select
    ActiveCell.Value = "Area Up"
    ActiveCell.Offset(0, 1).Range("A1").Select
    ActiveCell.Value = "Area Total"

    ActiveCell.Offset(-1, 1).Range("A1").Select
    ActiveCell.Value = "CSC = intg/sr A (mC/cm^2)"
    ActiveCell.Offset(-1, -1).Range("A1").Select
    ActiveCell.Value = "Sr * A"
    ActiveCell.Offset(0, 1).Range("A1").Select
    ActiveCell.Value = Sr * Area
    Set SRACell = ActiveCell
    ActiveCell.Offset(0, 1).Range("A1").Select
    ActiveCell.Value = "V*cm^2/s"
    ActiveCell.Offset(2, -1).Range("A1").Select
    ActiveCell.Value = "Area Down"
    ActiveCell.Offset(0, 1).Range("A1").Select
    ActiveCell.Value = "Area Up"
    ActiveCell.Offset(0, 1).Range("A1").Select
    ActiveCell.Value = "Area AVG"

    ActiveCell.Offset(-1, 1).Range("A1").Select
    ActiveCell.Value = "C = CSC / 2 dV (mF/cm^2)"
    ActiveCell.Offset(-1, -1).Range("A1").Select
    ActiveCell.Value = "PotWindow"
    ActiveCell.Offset(0, 1).Range("A1").Select
    ActiveCell.Value = PotWindow
    Set PotWindowCell = ActiveCell
    ActiveCell.Offset(0, 1).Range("A1").Select
    ActiveCell.Value = "V"
    ActiveCell.Offset(2, -1).Range("A1").Select
    ActiveCell.Value = "Area Down"
    ActiveCell.Offset(0, 1).Range("A1").Select
    ActiveCell.Value = "Area Up"
    ActiveCell.Offset(0, 1).Range("A1").Select
    ActiveCell.Value = "Area AVG"

    Strt.Activate
    ActiveCell.Offset(1, 0).Range("A1").Select
    Set Strt = ActiveCell

'collect data
    Strt.Activate
    V1 = 0
    ActiveCell.Offset(0, -2).Range("A1").Select
    V1 = ActiveCell.Value
    Do While V1 >= 0
```

```
        ActiveCell.Offset(1, 0).Range("A1").Select
        V1 = ActiveCell.Value
    Loop
    V2 = ActiveCell.Value
    ActiveCell.Offset(0, 2).Range("A1").Select

For i = 1 To Laps
        'Integrate Ox1
        CurrentCycle = ActiveCell.Value
        ActiveCell.Offset(0, -1).Range("A1").Select
        Do While V2 <= V1
            i1 = ActiveCell.Value
            yValuesDown.Add (ActiveCell.Value)
            ActiveCell.Offset(0, -1).Range("A1").Select
            V1 = ActiveCell.Value
            xValuesDown.Add (ActiveCell.Value)
            ActiveCell.Offset(1, 0).Range("A1").Select
            V2 = ActiveCell.Value
            ActiveCell.Offset(0, 1).Range("A1").Select
            i2 = ActiveCell.Value
            'ActiveCell.Offset(0, 1).Range("A1").Select
        Loop

        xValuesUp.Add (V1)
        yValuesUp.Add (i1)
        Do While V2 >= V1
            i1 = ActiveCell.Value
            yValuesUp.Add (ActiveCell.Value)
            ActiveCell.Offset(0, -1).Range("A1").Select
            V1 = ActiveCell.Value
            xValuesUp.Add (ActiveCell.Value)
            ActiveCell.Offset(1, 0).Range("A1").Select
            V2 = ActiveCell.Value
            ActiveCell.Offset(0, 1).Range("A1").Select
            i2 = ActiveCell.Value
        Loop

        xValuesDown.Add (V1)
        yValuesDown.Add (i1)
        Do While V2 >= 0
            i1 = ActiveCell.Value
            yValuesDown.Add (ActiveCell.Value)
            ActiveCell.Offset(0, -1).Range("A1").Select
            V1 = ActiveCell.Value
            xValuesDown.Add (ActiveCell.Value)
            ActiveCell.Offset(1, 0).Range("A1").Select
            V2 = ActiveCell.Value
            ActiveCell.Offset(0, 1).Range("A1").Select
            i2 = ActiveCell.Value
        Loop
    Set Strt = Offset(0, 1)
```

```
'copy to array
   ValuesUp = CopyToArray(xValuesUp.ToArray, yValuesUp.ToArray)
   ValuesDown = CopyToArray(xValuesDown.ToArray, yValuesDown.ToArray)

'organize data
   ValuesDown = SortByFirst(ValuesDown, xValuesDown) ' sort by x values

'sum w/ LinInterp
'print results
Dim n As Integer
Dim x As Double
Dim dx As Double
Dim Change As Double
Dim AreaTotal As Double
Dim AreaUp As Double
Dim AreaDown As Double
Dim y1 As Double
Dim y2 As Double

n = 1000
x = xValuesDown(0)
dx = (xValuesDown(xValuesDown.Count - 1) - x) / n

   For j = 0 To n - 1
      y1 = LinInterp(x, ValuesDown)
      x = x + dx
      y2 = LinInterp(x, ValuesDown)
      Change = ((y1 + y2) / 2) * dx
      If Change > 0 Then AreaUp = AreaUp - Change
      If Change < 0 Then AreaDown = AreaDown + Change
      AreaTotal = AreaTotal - Change
   Next

x = xValuesUp(0)
dx = (xValuesUp(xValuesUp.Count - 1) - x) / n
   For j = 0 To n - 1
      y1 = LinInterp(x, ValuesUp)
      x = x + dx
      y2 = LinInterp(x, ValuesUp)
      Change = ((y1 + y2) / 2) * dx
      If Change > 0 Then AreaUp = AreaUp + Change
      If Change < 0 Then AreaDown = AreaDown - Change
      AreaTotal = AreaTotal + Change
   Next

'print results
   Rslt.Activate
   ActiveCell.Offset(i, 0).Range("A1").Select
   ActiveCell.Value = CurrentCycle
   Offset(0, 1).Select
```

```vba
      ActiveCell.Value = AreaDown
      Offset(0, 1).Select
      ActiveCell.Value = AreaUp
      Offset(0, 1).Select
      ActiveCell.Value = AreaTotal
      Offset(0, 1).Select

      ActiveCell.FormulaR1C1 = "=RC[-3]/" & SRACell.Address(, , xlR1C1)
      Offset(0, 1).Select
      ActiveCell.FormulaR1C1 = "=RC[-3]/" & SRACell.Address(, , xlR1C1)
      Offset(0, 1).Select
      ActiveCell.FormulaR1C1 = "=RC[-3]/" & SRACell.Address(, , xlR1C1)
      Offset(0, 1).Select

      ActiveCell.FormulaR1C1 = "=RC[-3]/" & PotWindowCell.Address(, , xlR1C1) & "/2"
      Offset(0, 1).Select
      ActiveCell.FormulaR1C1 = "=RC[-3]/" & PotWindowCell.Address(, , xlR1C1) & "/2"
      Offset(0, 1).Select
      ActiveCell.FormulaR1C1 = "=RC[-3]/" & PotWindowCell.Address(, , xlR1C1) & "/2"

'Reset for next loop
      AreaTotal = 0
      AreaDown = 0
      AreaUp = 0
      xValuesUp.Clear
      xValuesDown.Clear
      yValuesUp.Clear
      yValuesDown.Clear
      Strt.Activate
Next

Rslt.Activate

'Move to Collected peaks sheet
Dim CurrentSheet As String
Dim CperA As Double

      CurrentSheet = ActiveSheet.Name
      Selection.End(xlDown).Select
      Selection.End(xlToRight).Select
      CperA = ActiveCell.Value
      Sheets("Collected peaks").Select
      ActiveCell.Value = CperA * Area
      ActiveCell.Offset(1, 0).Range("A1").Select
      ActiveCell.Value = CperA
      ActiveCell.Offset(-1, 2).Range("A1").Select
      Sheets(CurrentSheet).Activate

Rslt.Activate

End Sub
```